

Supercontinuum generation via *in-situ*
femtosecond-laser-induced filamentation
for ultrabroadband femtosecond/picosecond
coherent Raman spectroscopy
MSc Thesis

A.J. Stutvoet

Delft University of Technology

Supercontinuum generation via *in-situ* femtosecond-laser-induced filamentation for ultrabroadband femtosecond/picosecond coherent Raman spectroscopy

MSc Thesis

by

A.J. Stutvoet

in partial fulfilment of the requirements for the degree of

Master of Science
in Aerospace Engineering

at the Delft University of Technology,
to be defended publicly on Friday November 19, 2021 at 11:30 AM.

Thesis committee:	Prof.dr.ir. P. Colonna di Paliano	TU Delft, chair
	Dr. R.M. Groves	TU Delft, external examiner
	Dr.ir. A. Bohlin	TU Luleå, principal supervisor
	Ir. F. Mazza	TU Delft, daily supervisor

This thesis is confidential and cannot be made public until November 20, 2021.

An electronic version of this thesis is available at <http://repository.tudelft.nl/>.

Summary

Two-beam femtosecond/picosecond (fs/ps) coherent Raman spectroscopy (CRS) is the benchmark for laser diagnostic measurements in the gas phase. The fs-duration pump/Stokes pulse is used to excite the ro-vibrational modes of the Raman active molecules. The ps-duration probe is scattered coherently from the excited molecules. The pump and Stokes photon originate from the same pulse, therefore they overlap automatically spatially and temporally. The difference in frequency between the pump and the Stokes photon needs to match with the energy gap of molecule specific transitions. The finite bandwidth of the fs pump/Stokes pulse determines the probability to excite different transitions. To measure in the vibrational fingerprint region ($\Omega = 800\text{-}1400\text{cm}^{-1}$) a supercontinuum is required. Measurements in the vibrational fingerprint region can ease the fitting procedure due to the far spaced spectral lines and give additional information on major combustion species like for example carbon dioxide, oxygen and molecular hydrogen. In this work *in-situ* femtosecond-laser-induced filamentation is proposed as supercontinuum source for ultrabroadband two-beam fs/ps CRS. Fs-laser-induced filamentation is a non-linear optical process where the pulse self-focusses, a supercontinuum is created *in-situ* through self-phase modulation and non-linear dispersion in the plasma medium. *In-situ* generation of the supercontinuum allows for a great simplification of the experimental setup compared to *ex-situ* generation of the supercontinuum, as no additional chirped mirrors are required to deliver a near-transform-limited ultrabroadband pulse to the probe volume. An experimental campaign is presented split into three phases.

In the first phase of the experimental campaign the filamentation process is characterised. This includes measurements of the power required to initiate the filamentation process and measurements to find the spatial dimensions of the filament. Furthermore, the work demonstrates the effects of different boundary conditions on the excitation efficiency. The effects of input pulse power and temperature are major, the effects of gas composition are smaller. It is found that pulse compression by the filamentation process is stable from shot-to-shot. A novel experiment where the input and output pulse duration for different amounts of pre-chirping is presented. A chirped input pulse ($\tau \approx 60\text{fs}$) results in the shortest output pulse duration out of the filament. This is surprising, as most optical processes are strongest for transform-limited input pulses ($\tau \approx 35\text{fs}$). Most likely, the increase in pulse duration enhances the delayed nuclear response.

To avoid ionization in the probe volume the filament is placed in front of the probe volume. This increases the interaction length compared to the conventional crossing method. In the second phase of the experimental campaign the probe volume dimensions are characterised with a novel procedure to relay-image the cross-section of the pump/Stokes pulse output by the filament, to estimate the beam waist at the probe volume with its divergence. The estimated beam waist gives reasonable results, although it is sensitive to the calibration. The estimated interaction length is most likely too long due to simplifications in the post-processing.

In the third phase of the experimental campaign thermometry is performed with different boundary conditions. The work shows that thermometry is affected when the filament is placed inside the probe volume, both spectral heating and cooling are observed. Furthermore, for some pump/Stokes pulse energies spectral heating is observed. The change in excitation efficiency due to the different boundary conditions results most likely in a normalisation error. New experiments are proposed to validate these speculations. The stable excitation efficiency results in sufficient bandwidth to excite all the ro-vibrational Raman transitions up to $\Omega = 1600\text{cm}^{-1}$ behind optical windows. This is demonstrated by the first simultaneous single-shot measurement of ro-vibrational CO_2 and O_2 CRS spectra behind an optical window in a laminar hydrocarbon flame.

Contents

List of Figures	vii
List of Tables	ix
1 Introduction	1
2 Theory on Coherent Raman Spectroscopy	3
2.1 Energy Levels	3
2.2 Population Distribution	6
2.3 Scattering of Light	7
2.4 Intensity of Signal	10
3 Overview of Experimental Implementations	15
3.1 Nanosecond CRS	15
3.2 Time-Resolved CRS	15
3.3 Two-Beam CRS	16
3.4 Experimental Setup	17
3.5 Ultrabroadband CRS	19
4 Theory on Femtosecond-Laser-Induced Filamentation	21
4.1 Light Propagation	21
4.2 Kerr-Effect: Self-Focusing	22
4.3 Kerr-Effect: Self-Phase Modulation	23
4.4 Plasma Generation	25
4.5 Femtosecond-Laser-Induced Filamentation	25
4.6 Experimental Implementation	26
5 Characterisation of Femtosecond-Laser-Induced Filamentation	27
5.1 Efficiency of Filamentation Process	28
5.2 Dimensions of Filament	28
5.3 Measurement of Critical Power in Air	32
5.4 Estimate of Pulse Duration From Non-Resonant Signal	35
5.5 Effect of Boundary Conditions on Non-Resonant Signal	38
6 Characterisation of Probe Volume Dimensions	47
6.1 Probe Volume Dimensions Without Filamentation	48
6.2 Probe Volume Dimensions With Filamentation	49
6.3 Concluding Remarks	53
7 Characterisation of Ultrabroadband CRS Thermometry	55
7.1 Relation of Pump/Stokes Energy and CARS Signal	55
7.2 Effect of Filament Location on Thermometry	57
7.3 Effect of Input Energy on Thermometry	60
7.4 Effect of Combustion on Thermometry	61
7.5 Ultrabroadband Coherent Raman Spectroscopy Behind Optical Window	63
8 Conclusion and Outlook	65
Bibliography	67
Acknowledgements	73

List of Figures

2.1	The harmonic oscillator and the rigid rotator.	3
2.2	Schematic of vibrational and rotational states within ground electronic configuration.	4
2.3	Vibrational and rotational population distributions of N_2	6
2.4	Different possibilities for light to scatter during the interaction with a molecule.	7
2.5	Principle of photon and energy levels coupling for CSRS and CARS.	8
2.6	Illustration of energy coupling for non-resonant signal.	12
2.7	Herman-Wallis factors for N_2	13
2.8	Placzek-Teller coefficients for N_2	14
3.1	Phase matching condition for several alignment schemes.	17
3.2	Schematic of the experimental setup with ultrafast amplifier system, combined with SHBC and an external compressor for ultrabroadband coherent Raman spectroscopy.	17
4.1	Illustration of slice-by-slice self-focusing.	23
4.2	Conical emissions of filament.	24
4.3	Schematic of laser pulse undergoing self-focusing.	25
4.4	Schematic of experimental implementation of <i>in-situ</i> femtosecond-laser-induced filamentation for ultrabroadband femtosecond/picosecond coherent Raman spectroscopy.	26
5.1	Conversion efficiency of the filamentation process in different gasses.	28
5.2	Schematic of experimental setup for imaging of N_2+ fluorescence with consumer camera.	29
5.3	Post-processing procedure to remove the flame from the pictures and find the N_2+ fluorescence intensity profile.	30
5.4	Picture of N_2+ fluorescence in different environments.	31
5.5	Schematic of experimental setup for imaging of N_2+ fluorescence with scientific camera.	33
5.6	Averaged N_2+ fluorescence signal for three different pump/Stokes pulse energy levels.	33
5.7	Direct measurement of critical power.	34
5.8	Li et al. (2016) presents direct measurement of critical power performed in ethanol/air flame.	35
5.9	Averaged non-resonant single-shot CSRS spectrum measured in argon at $E_{p/S} = 60\mu J$ to validate model.	37
5.10	Averaged non-resonant single-shot CSRS spectrum measured in argon at $E_{p/S} = 1000\mu J$ to validate model.	37
5.11	Effects of pre-chirping on pulse compression by the filamentation process in air at room temperature.	39
5.12	Averaged non-resonant single-shot CSRS spectrum measured in argon for different pump/Stokes pulse energies.	40
5.13	Estimate of effective pulse duration for different input powers.	41
5.14	Averaged non-resonant single-shot CSRS spectrum measured for a range of pump/Stokes pulse energies in several gasses at room temperature.	42
5.15	Estimate of effective pulse duration for several gas compositions.	43
5.16	Schematic of steel non-resonator to change gas temperature.	44
5.17	Averaged non-resonant single-shot CSRS spectrum measured at different pump/Stokes pulse energies for $T = 295$ and $660K$	45
5.18	Estimate of effective pulse duration for several gas temperatures.	45
5.19	Averaged non-resonant single-shot CSRS spectrum measured for a range of pump/Stokes pulse energies inside laminar hydrogen/air diffusion flame.	46
6.1	Schematic of geometrical crossing of pump/Stokes pulse with probe pulse.	48

6.2	Schematic of experimental setup to find beam waist of pump/Stokes pulse and probe Pulse.	48
6.3	Schematic of coherent imaging spectrometer employed to estimate pump/Stokes pulse divergence.	49
6.4	Dispersed colours of pump/Stokes pulse cone.	50
6.5	Typical cross section of pump/Stokes beam waist intensity.	51
6.6	Divergence of pump/stokes pulse measured after filament.	51
6.7	Interaction length for different crossing angles in filamentation regime.	52
7.1	Scaling of resonant and non-resonant CARS signal with pump/Stokes pulse energy. . .	56
7.2	Typical fit of single-shot ultrabroadband CARS spectrum via <i>in-situ</i> femtosecond-laser-induced filamentation in molecular nitrogen at room temperature.	58
7.3	Effect of different positions of the filament with respect to the probe volume on CARS thermometry.	59
7.4	Typical fit of single-shot ultrabroadband CARS spectrum via <i>in-situ</i> femtosecond-laser-induced filamentation in molecular nitrogen at room temperature.	60
7.5	Effect of pump/Stokes pulse power on CARS thermometry.	61
7.6	Typical fit of single-shot ultrabroadband CARS spectrum via <i>in-situ</i> femtosecond-laser-induced filamentation in laminar premixed methane/air flame.	62
7.7	Effect of pump/Stokes pulse energy on flame thermometry in premixed methane/air flame.	62
7.8	Schematic of implementation of optical window in experimental setup.	63
7.9	Typical fit of single-shot ultrabroadband CSRS spectrum via <i>in-situ</i> femtosecond-laser-induced filamentation measured in fuel-lean laminar premixed methane/air flame behind an optical window.	64

List of Tables

5.1	Dimensions of filament in different environments.	32
7.1	Measured single-shot precision of ultrabroadband CSRS via <i>in-situ</i> femtosecond-laser-induced filamentation in fuel-lean laminar premixed methane/air flame behind an optical window.	64

1

Introduction

The global surface temperature of the Earth has been rising every decade since 1850. Most likely, the period from 1983 to 2012 was the warmest period in 1400 years in the Northern Hemisphere. The atmospheric concentrations of carbon dioxide, methane and nitrous oxide are higher than they have been in the last 800,000 years due to anthropogenic emissions. It is extremely likely that the increase in greenhouse gasses is the dominant cause for the observed warming. The anthropogenic greenhouse gas emissions are driven by economic and population growth. The rise in temperature leads to all sort of problems, among others; the rising of the sea levels, regions that become uninhabitable for both animals and humans, and more extreme weather patterns. [1]

Ambitious goals have been set to limit the global average temperature increase to well below 2°C above pre-industrial levels in the Paris agreements [2]. All pathways which lead to such reduction require substantial emission reductions over the next few decades, with near zero emissions of CO_2 by the end of the century [1]. To prevent further anthropogenic emissions science has to develop green alternatives for the production of energy. One of the most urgent issues worldwide is the pollution generated through the conversion of chemical energy to heat by combustion processes [3]. Industrial stationary ground-based engines produce more than 90% of energy production (2018 data) [4]. Furthermore, economically viable green alternatives are not always available. For example, there exists no clear alternative for engines in the aerospace industry, while aviation accounts for 3.5% of the effective radiative warming [5].

Sufficient reasons to justify further research to the fundamentals of combustion processes in order to improve the efficiency and limit emissions. Combustion is characterised by complicated turbulent chemical processes [3]. These processes involve ten-to-hundreds of chemical species and hundreds-to-thousands of chemical reactions [3]. Accurate and precise measurements in flames are required to study the fundamentals of combustion and innovative designs [6]. The diagnostic tools need to withstand harsh environment in flames. To give an idea; methane/air flames have adiabatic flame temperatures of up to 2236K [7]. Similar temperatures are possible in hydrogen/air flames. Hydrogen/air flames have adiabatic flame temperatures of 2442K [7].

Traditional measurement techniques exist, such as thermocouples to measure temperature and chromatography to measure species concentrations [6]. To acquire *in-situ* measurements of flames the traditional methods require a physical probe which disturbs the flow field. The velocity field in the flame changes as the gasses flow around the physical probe. The methods lack the ability to measure the complicated dynamics in for example turbulent flames. Therefore, they lack the ability to take the accurate measurements required for the development of advanced engines [6]. Currently, laser diagnostics is the method of choice compared to other measurement techniques. Mainly because it is non-perturbative (as mentioned before) and can measure *in-situ* with high accuracy and precision [6, 8–20].

For laser diagnostic measurements in the gas phase, coherent Raman spectroscopy (CRS) is the benchmark [8]. The method can perform measurements of molecular species concentrations, pressure and temperature [8–20]. The accuracy and precision of CRS are outstanding. Single-shot precision of $\sim 0.5\text{--}1.0\%$ [9, 10] and single-shot accuracy of $\sim 2\text{--}3\%$ [10–12] have been demonstrated. Furthermore, the temporal resolution (resolution in time) is in the range of picoseconds ($p_s = 10^{-12}s$) to femtoseconds ($f_s = 10^{-15}s$) [18, 19], a time frame in which the measurement is collision independent. Also, measurements are possible with excellent spatial resolutions in the order of micrometres [10, 14, 20], where spatial resolution refers to the size of the measurement space which is named the probe volume.

In this thesis two-beam fs/ps CRS is used. The methodology allows for time resolved measurements at high repetition rates through windowed combustors [21]. Fundamental research in stable open flames up to research in windowed combustors with highly turbulent flow fields is possible. Two-beam CRS uses two laser pulses; the pump/Stokes pulse contains the pump and the Stokes photon, and the probe pulse contains the probe photon. The bandwidth of the pump/Stokes pulse determines which spectral lines can be measured. These spectral lines are temperature and species specific. The spectrum is typically described by Raman shift (ω) in wavenumbers (cm^{-1}). In the vibrational fingerprint region (high Raman shift, $\Omega = 800\text{--}1400cm^{-1}$ [22]) the spectrum is less congested with spectral lines compared to low Raman shifts. Measurements in the vibrational fingerprint region can ease the fitting procedure and give additional information on major combustion species like for example carbon dioxide, oxygen and molecular hydrogen. In a two-beam CRS setup this requires an ultrabroadband pump/Stokes pulse, or in other words a supercontinuum.

Different methods exist to create an ultrabroadband pulse. In this work supercontinuum generation via *in-situ* fs-laser-induced filamentation is suggested. *In-situ* generation means that the pulse is created near the probe volume. For practical application like combustors this means that the pulse is created behind an optical window. Fs-laser-induced filamentation is a non-linear optical process which influences beam propagation and causes spectral broadening. Ultrabroadband CRS with *in-situ* fs-laser-induced filamentation is an undeveloped research field [23–28]. Thermometry has been performed in the time domain; dephasing of the coherence is used to estimate the temperature [24]. No research is available where single-shot ultrabroadband fs/ps CRS in the frequency domain is used to measure temperature or species concentration in flames.

The thesis aims to contribute to the development of two-beam fs/ps CRS by characterising fs-laser-induced filamentation and the effects of fs-laser-induced filamentation on thermometry. An experimental campaign is designed to find the limitations of the technology. The main research objectives include a characterisation of the supercontinuum and how this is affected by different boundary conditions, the power required to initiate the filamentation process, the dimensions of the probe volume, and the effects of different boundary conditions on thermometry. Furthermore, the thesis aims to demonstrate ultrabroadband CRS behind an optical window.

The report is structured in eight chapters. Firstly, some of the fundamental theory on CRS and different experimental implementations of CRS are discussed in Chapter 2 and 3. Why *in-situ* generation of the supercontinuum with fs-laser-induced filamentation is promising for CRS is further elaborated on. Then, theory on fs-laser-induced filamentation is presented in Chapter 4. Next, the results of the experimental campaign are presented. The campaign is split into three phases. Chapter 5 covers the first phase, it focuses on fs-laser-induced filamentation. An example of an output parameter is the energy required to initiate the filamentation process. The second phase consists of a novel approach to characterise the probe volume dimensions under filamentation conditions, this phase is presented in Chapter 6. Chapter 7 covers the third phase where the effects of the filamentation process on thermometry are discussed. This chapter concludes with a demonstration of ultrabroadband CRS thermometry behind an optical window. Finally, in Chapter 8 the conclusions are presented.

2

Theory on Coherent Raman Spectroscopy

In this chapter the theory on Coherent Raman Spectroscopy (CRS) is discussed. First, some theory on the rotational and vibrational energy levels is presented in [Section 2.1](#). Then, the energy level distribution dependence on temperature and species concentration is elaborated on in [Section 2.2](#). With this fundamental theoretical background it is possible to further explain CRS. In [Section 2.3](#) the scattering of light between the different energy levels is discussed. Finally, the chapter concludes with a description of the intensity of the CRS signal and different terms required to model the spectrum in [Section 2.4](#)

2.1. Energy Levels

In CRS light interacts with molecules. The interaction between electromagnetic waves and matter depends on the energy levels of the molecules. Energy levels are the basis of the physics in CRS and therefore are vital to understand. This section is based on the introduction of CRS in Bohlin (2012) [8].

Firstly, a molecule needs to be considered. A molecule consists of at least two atoms bound together with chemical bonds. In general an atom consists of negatively charged electrons, neutrons without charge (some molecules do not have neutrons), and positively charged protons. The neutrons and protons together form the nucleus, for a diatomic molecule two nuclei can be found near the centre of a molecule.

In a first approximation a diatomic molecule can be simplified as shown in [Figure 2.1](#), here the mass of the atom is represented by point masses. The point mass approximation can be made as the size of the nuclei is in the orders of femtometres ($10^{-15}m$) and contains most of the weight of the atom. The figure shows the vibrating and the rotating motion of the molecules as independent motions. For the rotational motion, the point masses of the nuclei are connected with a rod. Where for the vibrating motion the point masses are connected with a spring. Hereby, it is possible to derive the motion of the atoms with classical mechanics.

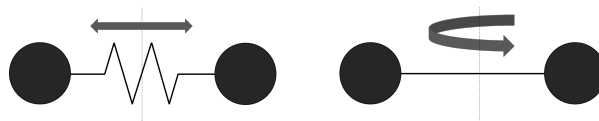


Figure 2.1: Point mass approximation for diatomic molecule. The figure presents the harmonic oscillator (left) and the rigid rotator (right).

The internal energy levels of a molecule are discrete. This comes from quantum mechanics, the energy levels are quantised. The total internal energy of a molecule can be decomposed into potential and the kinetic energy. The potential energy is associated with the bounded states from the electronic configurations. The kinetic energy is associated with the different motions of the molecule: translational, vibrational, and rotational energy. The translational energy is not regarded in this section, this energy is related to the speed of the molecules.

There is a large frequency difference between the vibrational and rotational motion; a molecule has around 1000 vibrations before 1 rotation is completed. Therefore, as a first approximation it can be assumed that the vibrational and rotational motions are independent of each other. This approximation is the Born-Oppenheimer approximation. The total energy can be determined as the sum of the energies of the different motions, excluding the electronic energies. In reality, the vibrating and rotating motions are dependent on each other. Later, a correction is presented to compensate for this effect.

A schematic of the vibrational and rotational energy levels within the ground electronic configuration is presented in [Figure 2.2](#). The vertical axis is scaled with the dissociation energy, the energy related to the strength of the chemical bond. It can be noted that the discrete steps in the vibrational states are larger compared the discrete steps in the rotational states. The energy level differences are utilised in CRS; this is further elaborated on in [Section 2.3](#).

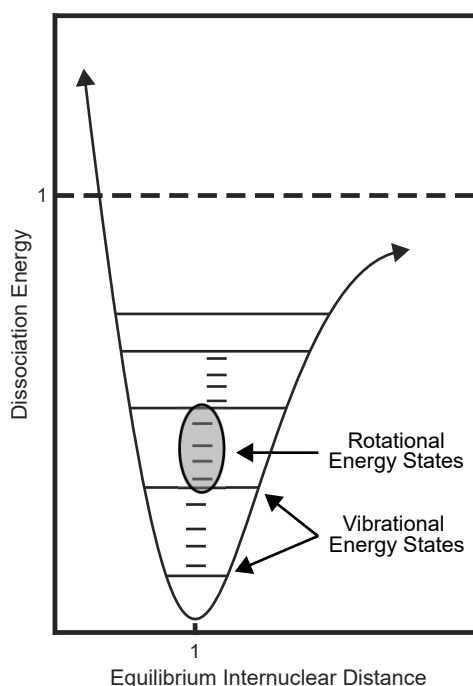


Figure 2.2: Schematic of vibrational and rotational states within ground electronic configuration. Vibrational states are subdivided by rotational states.

As mentioned, the vibrational and rotational levels are of interest. Starting with the vibrational motion, the motion can be described by a simple harmonic oscillator with sinusoidal oscillations. The motion is centred around the equilibrium internuclear distance. When the atoms are brought apart, a force proportional to the distance is present. The force represents the strength of the bond between the atoms. In the approximation, the electromagnetic force can be explained by the attraction of the positively charged atoms and negatively charged electrons when separated further than the equilibrium distance. The repulsion can be explained by the interaction when two nuclei (both positive) get closer than the equilibrium distance. This leads to a harmonic potential with vibrational energy solutions (E_v) as shown in [Equation 2.1](#).

$$E_v = \hbar\omega_{vib} \left(v + \frac{1}{2} \right), \quad (v = 0, 1, 2, \dots) \text{ [Joule]} \quad (2.1)$$

$$\omega_{vib} = \frac{1}{2\pi} \sqrt{\frac{k}{\mu}} \text{ [Hz]}, \quad \frac{1}{\mu} = \frac{1}{m_A} + \frac{1}{m_B}$$

Where k is the oscillator strength, \hbar is the reduced Planck constant, ω_{vib} is the vibrational frequency and v is the vibrational quantum number. The harmonic solution is only valid close to the equilibrium position. The model breaks down further away from the equilibrium position when the attractive force between the nuclei becomes weaker, here the bond breaks down. A more sophisticated description is the Morse potential (V), as shown in [Equation 2.2](#). Here, the effect of bond breaking is included in the potential.

$$V = D_{eq}[1 - e^{ar}]^2, \quad r = r_{eq} - r' \quad (2.2)$$

Where the constant a is species-specific and D_{eq} is the associated dissociation energy. To account for bond breaking higher-order terms are included to describe the vibrational energy levels as shown in [Equation 2.3](#). Most importantly, the difference in between the discrete vibrational energy steps are not at a fixed distance, as for the harmonic solution. At higher energy levels, the nuclei start to vibrate more strongly and the average internuclear distance of the nuclei increases. The energy steps become smaller.

$$E_v = \hbar\omega_{vib} \left(v + \frac{1}{2} \right) - \hbar\omega_{vib}x_e \left(v + \frac{1}{2} \right)^2 + \dots \text{ [Joule]} \quad (2.3)$$

Where x_e is the anharmonicity constant.

In a first-order approximation the rotational motion is described with a rigid rotator (see [Figure 2.1](#)). The energy levels can be described with [Equation 2.4](#).

$$E_J = \frac{\hbar^2}{2I} J(J + 1), \quad (J = 0, 1, 2, \dots) \text{ [Joule]} \quad (2.4)$$

Where J is the rotational quantum number and I is the moment of inertia. Some correction terms are required to model the actual physical behaviour. The derivation is outside the scope of this document. The reason for those terms are non-rigid properties of a molecule. Strong vibrations increase the average internuclear distance between the nuclei. Hereby, the moment of inertia is increased. This increase in moment of inertia decreases the rotational energy. In [Equation 2.5](#) a better model for the rotational energy levels is shown. Here correction terms are present to account for the before-named effect.

$$E_J = hc (BJ(J + 1) - DJ^2(J + 1)^2 + \dots), \quad (J = 0, 1, 2, \dots) \text{ [Joule]} \quad (2.5)$$

$$B_v = B - \alpha \left(v + \frac{1}{2} \right) + \gamma \left(v + \frac{1}{2} \right)^2 + \dots, \quad D_v = D + \beta \left(v + \frac{1}{2} \right) + \dots$$

Here B and D are equilibrium values, h is Planck's constant, and the constants α , β and γ are rotational-vibration (ro-vibrational) interaction constants.

2.2. Population Distribution

An energy state is an eigenvector of the Hamiltonian (operator corresponding to the total energy of a system) and has a single definite energy. One energy state is described by a combination of quantum numbers. The quantum numbers are the conserved quantities in the dynamics of a quantum system. Or in other words, the quantities which remain constant along each trajectory of the system. The probability density function of the energy states for a medium in thermal equilibrium can be described with the Boltzmann distribution. The probability that a molecule is in a certain energy state is given by Equation 2.6.

$$P(s) = \frac{1}{Z} \exp(-E(s)/kT), \quad Z = \sum_s \exp(-E(s)/kT) \quad (2.6)$$

Where Z is the partition function, T is the temperature, k is the Boltzmann's constant, and s is the energy state. For a system in thermal equilibrium, the distribution of the vibrational and rotational energy states is a function of temperature. For molecular nitrogen, the population distribution of the rotational and vibrational states are displayed in Figure 2.3.

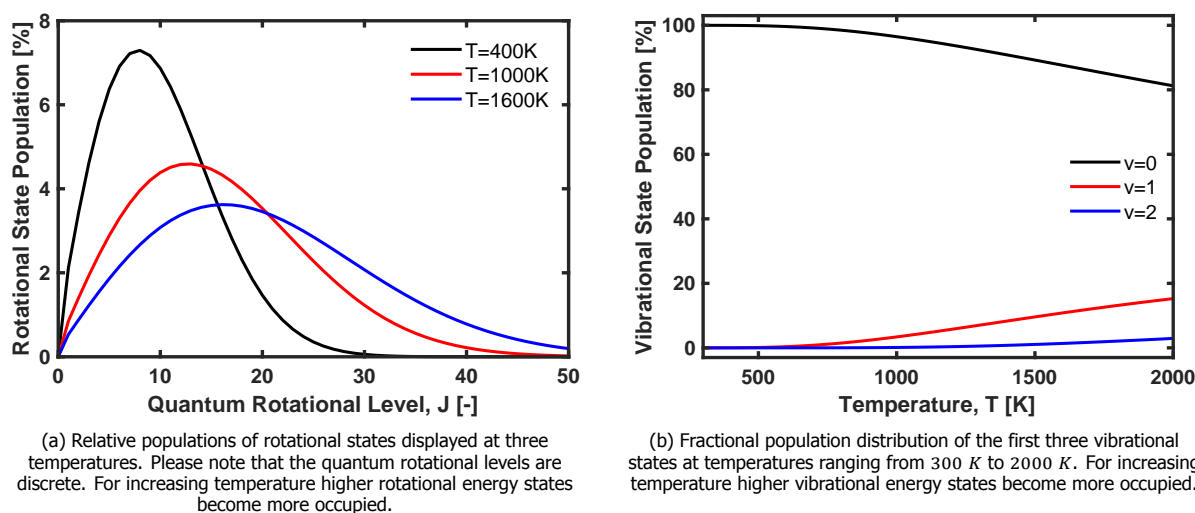


Figure 2.3: Vibrational and rotational population distributions of N_2 .

From the distribution of the rotational states it can be noted that at low temperatures there is a dense population of low quantum rotational levels. A rising temperature results in a flatter Boltzmann distribution with higher quantum rotational levels. Thus, on average the molecules rotate more rapidly at higher temperatures.

For molecular nitrogen the population distribution of the vibrational states at room temperature is monotonic, almost all molecules can be found in the first vibrational state. With increasing temperature the higher vibrational states become more occupied. Furthermore, the difference in between the vibrational states becomes more pronounced.

If a particle has multiple energy states with the same energy content, an energy level is degenerate. In calculations this needs to be included. The rotational levels have a energy state degeneracy of $g_J = 2J+1$ due to the magnetic sublevels [8]. Furthermore, a statistical weight factor (g_s) is required to account for coupling of the spin of the nucleus [8].

The population distribution is species specific. The species specific population distribution and the species specific discrete energy step locations make it possible to measure species concentrations. How the energy steps are utilised in CRS is further discussed in Section 2.3.

2.3. Scattering of Light

The internal energy of a photon, a light particle, can be described with Equation 2.7 [29].

$$E_{\text{photon}} = \frac{hc}{\lambda} = hf \quad (2.7)$$

Where h is Plack's constant, c is the speed of light, λ is the wavelength of the photon, and f is the frequency of the photon. Most important is that the internal energy of a photon is linked to its frequency.

The interaction of interest between photons and molecules is scattering. Although not scientifically correct, one could think as if the two collide. The photon and molecule combine their energies to a higher value than the original molecule, there is energy coupling. The coupling mechanisms, Rayleigh and Raman scattering, are displayed in Figure 2.4. Here, the horizontal solid lines display two energy states of a molecule. The vertical arrows represent the energy added or subtracted from a molecule. The combination of both energies is referred to as a virtual state (dashed horizontal line). This virtual state is short-lived and unobservable in quantum mechanics [30]. For the inelastic Rayleigh scattering no energy is transferred between photons and particles. For elastic Raman scattering energy is transferred. A decrease in photon energy is referred to as a Stokes shift and an increase in photon energy is referred to as an anti-Stokes shift.

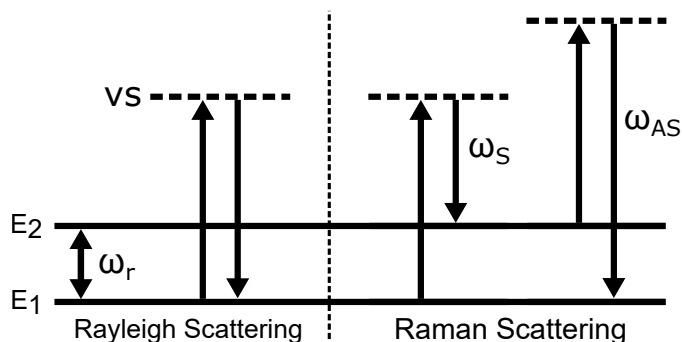


Figure 2.4: Different possibilities for light to scatter during the interaction with a molecule. From left to right, figure shows inelastic Rayleigh scattering, and elastic Raman scattering for the Stokes (ω_s) and anti-Stokes shift (ω_{AS}). Molecular states are displayed with solid horizontal lines, dashed horizontal lines are virtual states (vs).

CRS is a four wave mixing process. The pump, Stokes and probe pulse interact with the medium to produce the fourth CRS pulse, a schematic of the coupling of their energies through a molecule is shown in Figure 2.5. In classical terms, the frequency difference of the pump and Stokes pulse ($\omega_p - \omega_s$) oscillate the electrons inside the probe volume, where the probe volume is the location of interaction of the laser beams. When the frequency difference of the two optical waves is close to characteristic frequency of the harmonic oscillator (ω_r), the oscillation is driven efficiently. Then the electron clouds oscillate at the frequency difference and that changes the optical properties of the medium. The refractive index of the medium is periodically changed. The probe pulse is modulated by the medium, part of the probe pulse acquires the same periodic modulation as the medium. The probe pulse can acquire a Stokes ($\omega_{pr} + \omega_p - \omega_s$) or anti-Stokes ($\omega_{pr} - \omega_p + \omega_s$) shift. The different pathways are named coherent anti-Stokes Raman spectroscopy (CARS) and coherent Stokes Raman spectroscopy (CSRS, pronounced as "scissors"). The species specific energy states result in species specific CRS spectra. This fact makes CRS suitable for species concentration measurements.

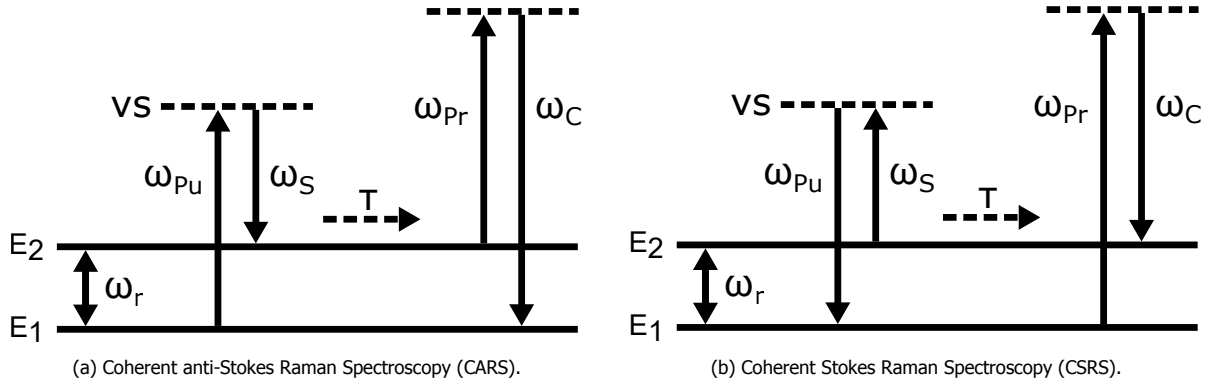


Figure 2.5: Principle of photon and energy levels coupling for CSRS and CARS. ω_{Pu} , pump pulse; ω_S , Stokes pulse; ω_{Pr} , probe pulse; ω_C , CRS signal; ω_r , resonance frequency; τ , probe pulse delay; vs , virtual state.

In a quantum mechanical model the state created in the medium by the pump and Stokes pulses is called a coherence. The CRS signal is coherent due to the coherence in the medium [31] and creates a laser-like pulse [8]. Therefore, CRS is an efficient technique as most of the output energy can be directed towards a camera.

In literature Raman shift is used commonly to display the frequency of the CRS signal. Raman shift is the spatial frequency difference between the two energy states in wavenumbers. Wavenumbers are defined as the spatial frequency $1/\lambda$, where λ is the wavelength. The SI Unit is waves per metre (m^{-1}), however the SI unit is hardly used in the literature concerning CRS, more widely used is cm^{-1} as this is more conveniently spaced.

2.3.1. Polarizability

This section describes how the polarizability of molecules is important to CRS and how it depicts the oscillatory modes of molecules. The polarizability of a molecule describes its tendency to be distorted by an electric field.

How relatively heavy positively charged nuclei are surrounded by a relatively light cloud of electrons was described in the previous sections. Electromagnetic fields push and pull on the molecules. The driving frequencies in the visible and near infrared range oscillate at frequencies too high for the nuclei to follow adiabatically [32]. The lighter electrons are able to follow the rapid oscillations, therefore the optical resonance created in the medium is mostly due to the motions of electrons [32].

The movement in the molecule induces separation between the positively and negatively charged nucleus and electrons. The separation of charges determines the formation of an electric dipole. The total dipole moment of a molecule is the sum of the inherent dipole moment and the dipole moment due to an applied electric field as shown in Equation 2.8.

$$\vec{p}(t) = \vec{\mu}(t) + \vec{p}_{induced}(t) \quad (2.8)$$

Here $\vec{p}(t)$ is the total polarization of a molecule, $\vec{\mu}(t)$ is the inherent dipole moment, and $\vec{p}_{induced}(t)$ is the induced polarization by an electric field. Some molecules have a dipole moment without an induced electric field, an example of this is a water molecule (H_2O). It consists of a triangle like arrangement of atoms where both hydrogen atoms connect to the oxygen atom in the middle. The area around the hydrogen atoms are slightly more positive than the area around the oxygen atom, therefore, there is a net dipole moment.

During CRS, the bounded electrons are displaced by the electric field of the pulses, the internal dipole moment can be described with Equation 2.9 when close to the equilibrium position [32].

$$\vec{u}(t) = -e \cdot r(t) \quad (2.9)$$

Where e is the charge of the electron and $r(t)$ is the displacement. As shown in Equation 2.9, the magnitude of the dipole moment of the molecule depends on the electron displacement. The electron displacement is dependent on how strong the electron is bonded to the nucleus. So, the stronger the bound, the smaller the displacement of electrons. The induced dipole moment in a molecule due to an external electric field is shown in Equation 2.10 [32].

$$\vec{p}_{induced}(t) = \hat{\alpha}(t)\vec{E}(t) \quad (2.10)$$

Where $\hat{\alpha}(t)$ is the polarizability tensor and $\vec{E}(t)$ is the applied electric field. The polarizability tensor links the applied electric field with the induced polarization. The polarizability tensor is a 3×3 matrix. The diagonal elements describe the anisotropic polarizability (γ) leading to vibrational motion. The off-diagonal elements describe the isotropic polarizability (α) leading to rotational motion.

To further derive an equation to describe the polarizability of the molecules during CRS, a few equations are needed. First, the incident electric field is described in Equation 2.11 [33].

$$\vec{E}(t) = \vec{E}_0 \cos(\omega_0 t) \quad (2.11)$$

Where \vec{E}_0 is the amplitude of the electromagnetic wave and ω_0 is the oscillating frequency. Then, it is required to describe the polarizability of a molecule. The polarizability can be approximated by a constant α_0 when it is assumed that there exist no nuclear modes and non-linearities. A nuclear mode is an eigenfrequency of the nuclear motion. To account for nuclear modes and non-linearities the electric polarizability needs to be expanded into a Taylor series in terms of the nuclear coordinate Q as shown in Equation 2.12 [34].

$$\hat{\alpha}(t) = \hat{\alpha}_0 + \left(\frac{\delta \hat{\alpha}}{\delta Q} \right)_0 Q(t) + \dots \quad (2.12)$$

Where $\frac{\delta \hat{\alpha}}{\delta Q}$ is the first-order correction term for the polarizability. It represents the coupling strength in between the nuclear and electronic coordinates [32]. For the derivation, the nuclear coordinate Q is approximated by an harmonic oscillator for the nuclear motion as shown in Equation 2.13 [32].

$$Q(t) = Q_0 \cos(\omega_\nu t) \quad (2.13)$$

Where Q_0 is the amplitude of the nuclear motion and ω_ν is the nuclear resonance frequency. The dipole moment in the presence of nuclear modes is found with a Taylor series as shown in Equation 2.14 [32].

$$\vec{\mu}(t) = \vec{\mu}_0 + \left(\frac{\delta \vec{\mu}}{\delta Q} \right)_0 Q(t) + \dots \quad (2.14)$$

The combination of the formulas presented in this section gives Equation 2.15.

$$\vec{p}(t) = \vec{\mu}_0 + \left(\frac{\delta \vec{\mu}}{\delta Q} \right)_0 Q_0 \cos(\omega_\nu t) + \left(\hat{\alpha}_0 + \left(\frac{\delta \hat{\alpha}}{\delta Q} \right)_0 Q_0 \cos(\omega_\nu t) \right) \vec{E}_0 \cos(\omega_0 t) + c.c. \quad (2.15)$$

Equation 2.15 can be rewritten to Equation 2.16 which describes the microscopic dipole moments whose oscillations determine the absorption/emission of electromagnetic radiation. The equation has four terms: infrared absorption, Rayleigh scattering, anti-Stokes, and Stokes. The first term, infrared absorption, describes the vibrational absorption activity. For absorption it is required that $(\delta\vec{\mu}/\delta Q) \neq 0$. The second term, Rayleigh, describes the elastic scattering at the incident frequency of the electromagnetic wave; the frequency of light is unchanged. Lastly, the anti-Stokes and Stokes shift shows the Raman shifted frequencies for the blue- and red-shift of the light, respectively. For a molecule to be Raman active it is required that $\frac{\delta\hat{\alpha}}{\delta Q} \neq 0$, the polarization must change with nuclear motion. As shown in the equation, there exist no difference in polarizability of the anti-Stokes and Stokes term, the strength of the two is equal. In reality, it is not, but the classical method as described here lacks the complexity to describe the difference [32].

$$\vec{p}(t) = \overbrace{\left(\frac{\delta\vec{\mu}}{\delta Q}\right) Q_0 \cos(\omega_v t)}^{\text{Infrared absorption}} + \overbrace{\hat{\alpha}_0 \vec{E}_0 \cos(\omega_0 t)}^{\text{Rayleigh}} + \frac{Q_0 \vec{E}_0}{2} \left(\frac{\delta\hat{\alpha}}{\delta Q}\right) \left(\overbrace{\cos[(\omega_0 + \omega_v) t]}^{\text{Anti-Stokes}} + \overbrace{\cos[(\omega_0 - \omega_v) t]}^{\text{Stokes}} \right) + \text{c.c.} \quad (2.16)$$

For most applications of light the propagation of light and the interactions with a medium can be described with linear optics. The sum of all the dipole moments cause polarization on a macroscopic level, this is described with Equation 2.17 [33]. The left side of the equation shows the summation of all electric dipoles per unit volume and the right side shows the macroscopic polarization as a function of the susceptibility. Where susceptibility indicates the degree of polarization on a macroscopic scale in response to an electric field.

$$\vec{P}(t) = N\vec{p}(t) = \epsilon_0 \chi^{(1)} \vec{E}(t) \quad (2.17)$$

Where $P(t)$ is the polarization, N are the number of dipole moments, $\vec{p}(t)$ is the local dipole moment created in a molecule, ϵ_0 is the permittivity of free space, and $\chi^{(1)}$ is the linear susceptibility. Here, the polarization depends linearly on the electric field of the light, all linear optical phenomena are based on this dependence [32]. In linear optics the properties of a medium are unaffected by the intensity of light; the superposition principle holds true in this regime [35]. If the electric field of light becomes strong enough, the polarization can not be described by a linear equation. The enhanced displacement of the electrons makes the assumption for an harmonic oscillator invalid as the anharmonic effects become more significant. The light waves and the material interact, exchanging momentum and energy, whereby the superposition principle is no longer valid [35]. In non-linear optics the response of the polarization is often described as a power series in terms of the electric field. The instantaneous function of the electric field strength is presented in Equation 2.18 [33].

$$\vec{P}(t) = \epsilon_0 [\chi^{(1)} \vec{E}(t) + \chi^{(2)} \vec{E}^2(t) + \chi^{(3)} \vec{E}^3(t) + \dots] \quad (2.18)$$

Where $\chi^{(n)}$ ($n = 2, 3, 4, \dots$) are the non-linear susceptibilities. The susceptibility $\chi^{(n)}$ indicates the degree of polarization in response to an electric field. The linear susceptibility ($\chi^{(1)}$) is dimensionless, while the non-linear susceptibilities have units of $(m/V)^{n-1}$.

2.4. Intensity of Signal

The CRS spectrum is dependent on the molecular species and the temperature. A model is used for the experimental campaign to analyse the data. Some important factors included in the model are elaborated on in this section. The highly non-linear and coherent characteristics of CRS lead to

complex optical and statistical behaviour of the four-wave mixing process [36]. For accurate determination of temperature, species concentrations and other properties with CRS it is therefore crucial to correctly implement the factors [37]. First, the model is discussed in this section. Then, the excitation efficiency is discussed in Section 2.4.1. Next, the Herman-Wallis factor and Placzek-Teller coefficients are discussed in Section 2.4.2 and 2.4.3.

In Boyd (2008) [33] the strength of the CRS signal is found by combining the Maxwell equation and part of the previously presented power series to describe the polarization as function of the susceptibilities (see Equation 2.18). The result is shown in Equation 2.19 [33].

$$I_{\text{CRS}}(z) = \frac{16\pi^4 \omega_{\text{CRS}}^2}{n^4 c^4} I_{\text{pump}} I_{\text{Stokes}} I_{\text{probe}} |\chi^{(3)}|^2 z^2 \text{sinc}^2\left(\frac{\Delta k z}{2}\right) \quad (2.19)$$

Where ω_{CRS} is the frequency of the CRS signal, I_{pump} , I_{Stokes} and I_{probe} are the intensities of the incident laser beams, z is the interaction length, and the sinc^2 -term is referred to as the phase matching condition. It can be noted that the intensity of the CRS signal is linearly dependent on all incident lasers. Furthermore, the intensity is dependent on the phase matching condition and the third-order susceptibility. Starting with the phase matching condition, the condition is given in Equation 2.20 [8].

$$\Delta k = (k_{\text{pump}} - k_{\text{Stokes}} + k_{\text{probe}}) - k_{\text{CRS}} \quad (2.20)$$

Here, k is the length of the wavevector of the four electromagnetic waves. Where each wave is described by $|k| = 2\pi n(\omega)\lambda$ [33], where λ is the wavelength and $n(\omega)$ is the index of refraction. From a mathematical point it can be observed in Equation 2.19 that the phase mismatch (Δk) should be minimised for an optimal energy conversion, for perfect phase matching $\Delta k = 0$. Then, the radiation propagates most efficiently into the desired direction due to conservation of momentum, meaning it is coherent scattering.

The third-order susceptibility is described with Equation 2.21.

$$\chi^{(3)} = \chi_{\text{NR}} + \sum_n \sum_J \frac{a_{J,J+2}}{\omega_{J,J+2} - \omega_{\text{pump}} + \omega_{\text{Stokes}} - i p \Gamma_{J,J+2}/2} \quad (2.21)$$

Where χ_{NR} is non-resonant part of the susceptibility. The term comes from the instantaneous electronic responses due to the incident electric fields. The other terms account for the delayed nuclear response; $\Gamma_{J,J+2}$ is the Raman linewidth and $a_{J,J+2}$ is the amplitude factor. The Raman linewidth ($\Gamma_{J,J+2}$) accounts for the linewidth of spectral lines. Spectral line broadening comes from several effects; among them are the Doppler effect, collisions broadening and the Stark effect [7, 36–40]. The Raman linewidth is found experimentally.

The amplitude factor for pure-rotational CRS is described by Equation 2.22 [8].

$$a_{J,J+2} = \frac{4}{45} \frac{N}{\hbar} b_{J,J+2} F^S(J) \gamma^2 \Delta \rho_{J,J+2} \quad (2.22)$$

Where N is the number density, $F^S(J)$ the Herman-Wallis factor (see Section 2.4.2), $b_{J,J+2}$ the Placzek Teller coefficient (see Section 2.4.3), γ is the polarizability anisotropy, and $\Delta \rho_{J,J+2}$ the normalised population difference involved in transitions.

As the intensity of the CRS signal scales to the third-order susceptibility squared ($I_{\text{CRS}} \propto |\chi^{(3)}|^2$) which is linearly dependent on the number density ($\chi^{(3)} \propto a_{J,J+2} \propto N$), the CRS signal scales with the number density squared ($I_{\text{CRS}} \propto N^2$). Therefore, the CRS signal in condensed matter is much stronger than

in a gas-phase medium due to the higher number density. This characteristic is used in [Chapter 6](#) to estimate the interaction length. Furthermore, consider the ideal gas law $PV = nRT$, which can be rewritten as a function of the number density: $N = n/V = P/RT$. Where P is the pressure of gas, V is the volume, n is the amount of substance of gas, R is the universal gas constant, and T is the temperature. From this it can be concluded that the intensity of the CRS signal is inversely proportional to the temperature of the probe volume. All in all, it shows that the generation of a high signal to noise ratio inside flame is most difficult as these measurement are at high temperature in the gas-phase.

To conclude the description on the CRS signal intensity, the population difference factor between two energy levels is presented in [Equation 2.23](#) [33]. The equation illustrates that CRS spectra are extremely suitable for thermometry. The population difference factor is dependent on the Boltzmann distribution which is linked to the temperature. Therefore, the CRS spectrum is directly related to the temperature.

$$\Delta\rho_{J,J+2} = \frac{g_J(2J+1)}{Q_J} [e^{-E_J/k_B T} - e^{-E_{J+2}/k_B T}] \quad (2.23)$$

Where g_J is the statistical weight factor, Q_J is the internal partition function, T is the temperature, and k_B is the Boltzmann constant. The term $(2J+1)$ is included to model the nuclear spin degeneracy, multiple energy states occupy the same energy level.

2.4.1. Excitation Efficiency

The finite bandwidth of the femtosecond ($f_s = 10^{-15}s$) pump/Stokes pulse determines the probability to excite different transitions. In post-processing, this needs to be compensated for by dividing the resonant CRS spectrum by a reference profile [8]. The reference profile includes only the non-resonant CRS spectrum created by the instantaneous response of the electronic configuration due to the electric fields. The mixing process is displayed in [Figure 2.6](#). The non-resonant CRS spectrum is generated when the pump, Stokes and probe photon interact with particles at the same instance in time. To record the resonant spectrum, the probe pulse is normally delayed, such that only the resonant nuclear response is probed. Here, the input photons are not available at the same instance in time for instantaneous coupling. Non-resonant and resonant CRS spectra are presented in [Section 5.5](#) and [Chapter 7](#), respectively. The average reference profile is typically recorded in a separate measurement with a gas without Raman resonances, like for example argon [8]. This procedure is referred to as *ex-situ* referencing of the excitation efficiency.

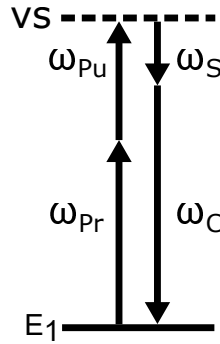


Figure 2.6: Convolution of pump, Stokes and probe photon when the three photons are present at the same time. A continuous signal is created, this is referred to as the non-resonant signal. ω_{Pu} , pump pulse; ω_S , Stokes pulse; ω_{Pr} , probe pulse; ω_C , CRS signal; vs , virtual state.

Ex-situ referencing of the excitation efficiency does account for variations in excitation efficiencies from shot-to-shot. Furthermore, it does not account for a different finite bandwidth of the fs pump/Stokes pulse due to different boundary conditions. In [Section 5.5](#) the effects of different boundary conditions on the excitation efficiency are studied, among the studied effects are gas

composition and temperature. Recently, a technique was developed where *in-situ* referencing of the excitation efficiency was used for spatially and temporally overlapped probe pulse and Pump/Stokes pulse [11]. Here the resonant and non-resonant susceptibility of the CRS signal are both measured simultaneously. The polarization dependency is used to generate the resonant and the non-resonant CRS signal with orthogonal polarization with respect to each other [41]. After which the cross-polarized signals are split based on their polarization. In this way, it is possible to measure shot-to-shot differences in the excitation efficiency [11]. For harsh environments, like turbulent flames, the *in-situ* referencing procedure is promising. [11]

It was found that at higher temperatures, *ex-situ* referencing over-predicts the temperature due to group-velocity dispersion (GVD) effects. GVD gives rise to temporal broadening of the pump/Stokes pulse, resulting in a decreased excitation bandwidth (GVD is further elaborated on in Section 4.1). For the tested gas, GVD scales linearly with density. As the density of a gas decreases with increasing temperature, the GVD-effect becomes less strong at higher temperatures. At higher temperature the excitation efficiency is therefore higher than expected with *ex-situ* referencing of the excitation efficiency.

2.4.2. Herman-Wallis Factor

The Herman-Wallis factor accounts for rotational-vibrational (ro-vibrational) coupling. As discussed in Section 2.1, the rigid rotor approximation becomes weaker when the moment of inertia changes due to a change in length of the molecule by the vibrational motion. The coupling is accounted for by the Herman-Wallis (HW) factor [42]. In general, light molecules have a larger coupling of the vibrational and rotational modes. Therefore, the HW-factor is more important for those molecules [43]. Different models exist, according to the James-Klemperer (JK) model and Tipping-Ogilvie (TO) model, the Herman-Wallis factor (F^S) is a function of the rotational quantum number, as shown in Equation 2.24 and 2.25 respectively [42].

$$F_{JK}^S = 1 + \frac{2\kappa^2 (J^2 + 3J + 3)}{\eta} \quad (2.24)$$

$$F_{TO}^S = \left[1 + \kappa^2 \left(\frac{p_1}{p_0} \right) (J^2 + 3J + 3) \right]^2 \quad (2.25)$$

Where $\kappa = 2B_e/\omega_e$, B_e is the equilibrium rotational constant, ω_e is the equilibrium vibrational constant, η is parameter which is dependent on the ratio between the first two terms of the anisotropic polarizability expansion, and p_1/p_0 is the ratio of the first two coefficients of the anisotropic polarizability expansion. The HW factor for the first 50 quantum rotational levels of molecular nitrogen for both the James-Klemperer model and the Tipping-Ogilvie model is shown in Figure 2.7.

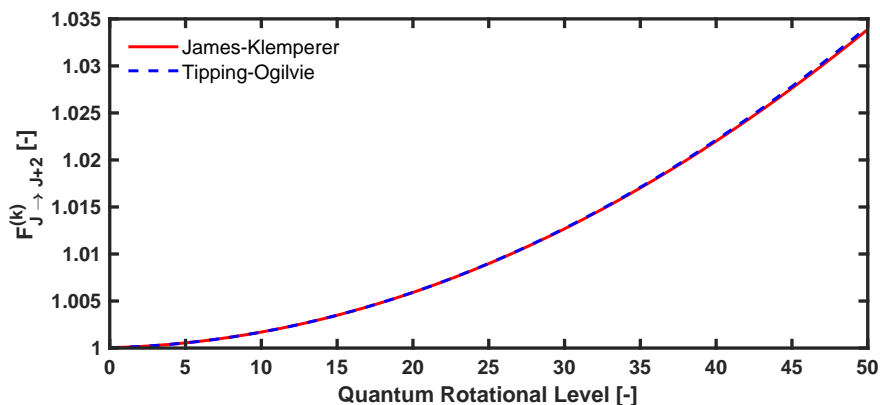


Figure 2.7: Herman-Wallis factors for N_2 . Please note that the quantum rotational levels are discrete.

An increase in rotational quantum number results in an increase in Herman-Wallis factor. Leaving out the Herman-Wallis factor would result in spectral heating, spectra which would suggest higher temperatures than the actual temperature.

2.4.3. Placzek-Teller Coefficients

The Placzek-Teller coefficients quantify the likelihood of different transitions. The transitions are characterised into three branches, the O-, Q-, and S-Branch. The Placzek-Teller coefficients for the O-, Q-, and S-Branch for molecular nitrogen are shown in Equation 2.26 [12, 44].

$$\begin{aligned} b_{(O\text{-Branch: } \Delta J=-2)} &= \frac{3J(J-1)}{2(2J-1)(2J+1)} \\ b_{(Q\text{-Branch: } \Delta J=0)} &= \frac{J(J+1)}{(2J-1)(2J+3)} \\ b_{(S\text{-Branch: } \Delta J=+2)} &= \frac{3(J+1)(J+2)}{2(2J+1)(2J+3)} \end{aligned} \quad (2.26)$$

The Placzek-Teller coefficients for the first 50 rotational levels of molecular nitrogen are presented in Figure 2.8. Some observation can be made. Firstly, at the lowest rotational level ($J = 0$), only transitions in the S-Branch are possible. As this quantum rotational level depicts the lowest energy level, it is impossible to have $\Delta J = -2$. Furthermore, as J goes to higher numbers the results of the Placzek-Teller coefficients converge. The probability for a molecule to go to a higher and lower rotational levels become almost equal. Lastly, the three chances add up to unity.

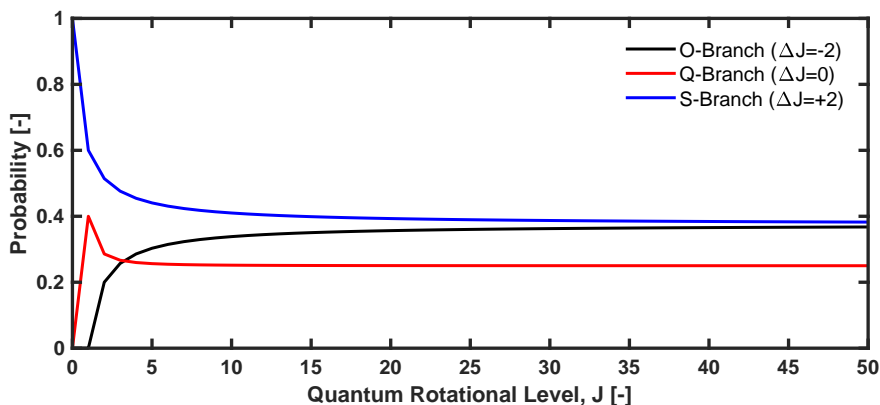


Figure 2.8: Placzek-Teller coefficients for N_2 . Please note that the quantum rotational levels are discrete.

3

Overview of Experimental Implementations

Development of experimental implementations of coherent Raman spectroscopy (CRS) over time are the basis of this chapter. As time progressed, shorter laser pulses were used. Firstly, nanosecond ($ns = 10^{-9}s$) CRS is discussed in [Section 3.1](#). Then, time-resolved CRS is elaborated on in [Section 3.2](#). Progress led to two-beam CRS as explained in [Section 3.3](#). The current experimental setup is discussed in [Section 3.4](#). Finally, the limitations of the current implementations and how ultrabroadband CRS can overcome those are elaborated on in [Section 3.5](#).

3.1. Nanosecond CRS

To enhance the signal to noise ratio of spontaneous Raman scattering, CRS was proposed for the gas phase [[45](#), [46](#)], and applied for species concentration and temperature measurements in 1974 [[47](#)] and 1975 [[48](#)] respectively. In the early days of CRS experiments, nanosecond ($ns = 10^{-6}s$) pulses were used [[48](#)]. The relatively long pulses were needed to initiate the third-order processes associated with CRS as they require high peak powers [[49](#)]. The measurements resulted in high spectral resolution. It was possible to distinguish closely spaced Raman transitions [[49](#)].

Ns CRS does have some limitations where the main limitation is the reliance on collision models. Molecules collide around 10^9 times per second [[50](#)]. A molecule collides with around 10 to a 1000 other molecules in the time of a ns pulse [[50](#)]. Therefore, the technology is prone to spectral broadening [[51](#)]. Furthermore, the long pulse lengths lead to overlap of the pump and Stokes pulse with the probe pulse, the direct interaction of those photons lead to high non-resonant contributions to the CRS signal, a non-ideal result.

3.2. Time-Resolved CRS

The temporal resolution increases at the cost of a decrease in spectral resolution when the length of the pulses decreases. Picosecond ($ps = 10^{-12}s$) CRS offers a unique compromise [[49](#)]. The decrease in pulse length allows for time-resolved measurements, meaning that probe pulse length becomes shorter than the average decay time of the molecular response. The measurements are extracted from the impulsive response of the excited system instead of the frequency dispersion of non-linear susceptibilities in the frequency domain [[52](#)]. With ps CRS it becomes possible to delay the probe pulse such that it does not temporally overlap with the Pump and Stokes pulse, hereby the non-resonant background signal is suppressed [[53](#)]. Interestingly, the technology can be used to characterise the

rotational specific line broadening coefficients [42], as it is possible to change the delay time compared to the excitation.

Further decrease of the pulse lengths leads to femtosecond ($f_s = 10^{-15}s$) CRS. The models for fs CRS require time-domain analysis, for ns and ps CRS the models rely solely on the frequency domain [49]. For an analysis in the frequency domain, it is possible to take the Fourier transformation of the different contributions separately and combine the effect. For fs CRS, this assumption does not hold.

Similar to ps CRS, the non-resonant signal of fs CRS can be suppressed by avoiding any overlap between the pump and Stokes pulses, and the probe pulse. As the pulses are shorter, the overlap can be avoided entirely. The main advantage of fs CRS is the improved efficiency of the excitation. The excitation for pure rotational CRS can result in non-adiabtic interactions between the laser pulse and the molecules if the laser pulse is around one tenth of the rotational period [54]. In literature this is sometimes referred to as impulsive excitation. For N_2 with a rotational period of $\sim 500f_s$ to undergo impulsive excitation a $\sim 50f_s$ pulse is required. The high efficiency of impulsive excitation makes single-shot measurements possible as it generates appreciable signal levels. [11]

The possibilities for fs or ps single-shot CRS are limited. The probe pulse of fs CRS is prone to distortion through windowed combustors and ps CRS is limited to 10 or 20Hz measurement rates [49]. A solution for this was proposed in 2006: Hybrid fs/ps CRS, the proposal consisted a 100-fs pump and Stokes pulse used to induce coherence in the probe volume, where the coherence is then probed with a frequency-narrowed ps probe pulse [22, 55]. The combination of a short Pump/Stokes pulse and longer probe pulse combines the advantages of fs and ps CRS. The technique, named fs/ps CRS, has enough temporal resolution to suppress the non-resonant contributions while the spectral resolution is sufficient for detecting the frequency domain [49].

Recently, dual-probe one dimensional fs/ps hybrid rotational CRS was used to measure simultaneously the temperature, pressure and species concentrations in O_2/N_2 measurements [13]. Information in the time domain is found by probing twice. As it is known that the CRS signal strength decreases as a function of time and the rate of decay changes with thermodynamic properties [49], such as the temperature, pressure and molecular composition it is possible to retrieve the three properties.

3.3. Two-Beam CRS

The four-wave mixing process has been described with 3 incident laser which form a fourth coherent pulse, the CRS signal. In the experimental setup a two-beam CRS setup with a fs Pump/Stokes pulse and ps probe pulse is used. The experimental setup is elaborated on in Section 3.4. The pump and Stokes photons originate from the same pulse. This improvement leads to some simplifications. Namely that the pump and Stokes pulse temporally and spatially overlap automatically. Therefore, the robustness of the setup is greatly increased. Furthermore, it becomes easier to account for unwanted effects as beam-steering as compared to the three beam alternative. And lastly, the phase matching stipulates that the CRS signal will propagate with the probe pulse, which in turn makes it easier to align the CRS signal with the detector.

Besides the discussion above, it is good to note that more methods exist to cross the pump, Stokes and probe photons. Three phase matching conditions are displayed in Figure 3.1, for perfect phase matching $\Delta k = (k_{pump} - k_{Stokes} + k_{probe}) - k_{CRS} = 0$, where each wave-vector is represented by $|k| = 2\pi n(\omega)\lambda$ [33]. Firstly, it is possible to cross them using a BOXCARs setup as displayed in Figure 3.1a, here all input pulses need to be precisely pointed at specific angles into the probe volume. The resulting CRS signal is stand-alone pulse. Secondly, it is possible to use a collinear setup as displayed in Figure 3.1b, where all pulses move together on the same path. In general it is true that the smaller the angles in between the pulses, the larger the overlap between the pulses. For a collinear setup the interaction length is large, therefore, the signal to noise ratio is high. However, some spatial information is lost as a measurement takes place over a large area. And thirdly, the alignment for a two-beam CRS setup is shown in Figure 3.1c. Here, the CRS signal is directed into the probe pulse direction.

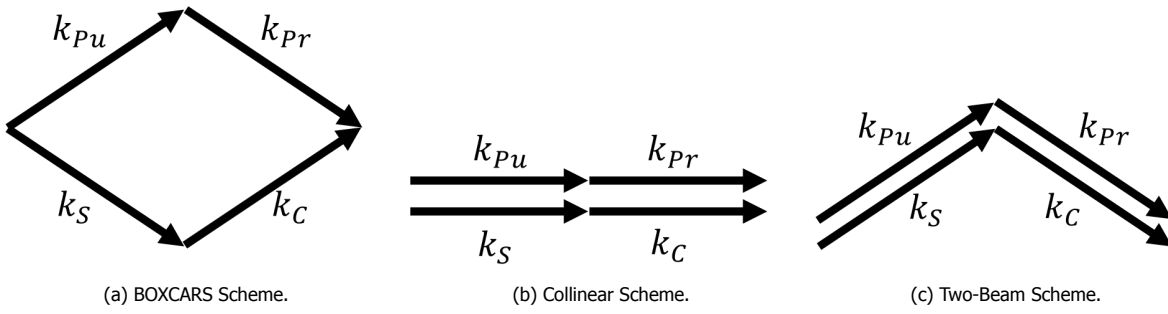


Figure 3.1: Phase matching condition for several alignment schemes. k_{pu} , pump wave-vector; k_{pr} , probe wave-vector; k_S , Stokes wave-vector; k_C , CRS signal wave-vector.

3.4. Experimental Setup

The "Ultrafast Laser Diagnostics Laboratory" of the Delft University of Technology is used for the experimental campaign. The experimental setup combines recent advancements in CRS spectroscopy. The description is based on *Castellanos et al. (2020)* [10].

The optical layout of the two-beam fs/ps CRS experimental setup is shown in [Figure 3.2](#). The setup is based on a single ultrafast regenerative amplifier system ($E = 7.5\text{mJ}$, 1kHz , Astrella Coherent) which outputs two repetition-wise synchronised beams.

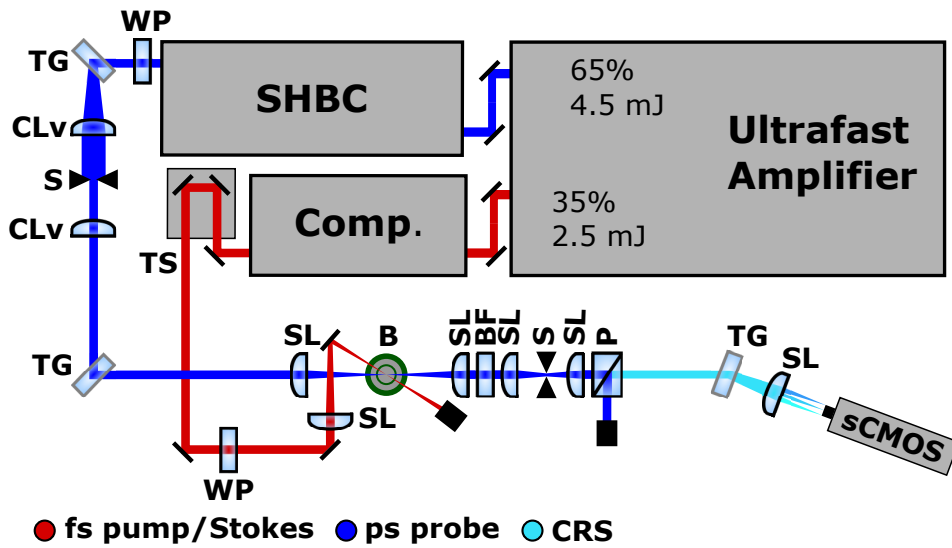


Figure 3.2: Schematic of the experimental setup with ultrafast amplifier system, combined with SHBC and an external compressor for ultrabroadband coherent Raman spectroscopy. B, burner; BF, bandpass filter; CLv, cylindrical lens with vertical alignment symmetry axes; P, polarizer beamsplitter; S, slit; SL, spherical lens; TG, transmission grating; TS, translation stage; WP, half-wave plate.

The first beam is the main compressed output ($\sim 65\%$, $E_{pr} = 4.5\text{mJ}/\text{pulse}$) which is directed to a second harmonic bandwidth compressor (SHBC) to be used as the probe pulse. In a SHBC the frequency is doubled by second harmonic generation. Here, the fs pulse is chirped and directed to a χ_2 non-linear crystal. The light is converted to a narrowband $\tau_{pr} = 4\text{ps}$ duration probe pulse with 30% conversion efficiency, leaving $E_{pr} = 1.2\text{mJ}/\text{pulse}$. The output is not entirely clean, meaning that there are undesired frequencies in the newly created pulse. Although the imperfections are several orders of magnitude smaller than the centre frequency of the probe pulse, the imperfections overlap with the expected frequency of the CRS signal. To clean the output of the probe pulse the linewidth is tuned, the light is directed through a spatial 4 f-filter. The filter consists of two transmission gratings

($\sim 3040\text{l/mm}$, Ibsen Photonics), two cylindrical lenses ($f = 300\text{mm}$), and a mechanical slit. First, one cylindrical grating horizontally diffracts the light based on its frequency, then a cylindrical lens with vertical alignment symmetry axes focuses the pulse. The Fourier plane is in the focus of the cylinder lens. A mechanical slit is able to cut away undesired wavelengths. The pulse is re-collimated and another grating is used to recreate the pulse. The resulting probe pulse is at a central wavelength of $\lambda_{pr} = 400\text{nm}$. The probe pulse is focussed by a spherical lens ($f = 300\text{mm}$) before it is crossed with the pump/Stokes pulse.

As a side-note: there exists a time-bandwidth product between the spectral bandwidth and the duration of the pulse which depends on the shape of the pulse. A pulse with the minimum product is referred to as a transform-limited pulse. For a Gaussian shaped pulse the minimum duration-bandwidth product is ~ 0.44 . As the pulses in the experiment are close to the minimum product, the length of the pulse can be slightly varied by the slit. If the slit is further closed, some frequencies are removed from the pulse and the total length of the pulse increases.

The combination of the SHBC and 4 f-filter is implemented to create efficiently a ps pulse with relatively cheap, passive equipment. The SHBC can convert the broadband fs pulse to a narrow-bandwidth ps pulse with appreciable efficiency. Another advantage for the SHBC is that the frequency of the CRS signal is doubled, which increases the CRS intensity with a factor four as the intensity of CRS is an function its frequency ($I_{CRS} \propto \omega_{CRS}^2$, see Section 2.4). One could reason that a further increase in the probe pulse frequency would be beneficial to optimise the experimental setup for high output energy. However, in practice, it would increase the cost of the setup dramatically. Lenses and especially cameras are optimised to work in the visible spectrum ($\lambda = 400\text{-}750\text{nm}$). Consumer photography has driven innovations and lowered cost for optical elements in the visible spectrum.

The second beam is the uncompressed output ($\sim 35\%$, $E_{p/S} = 2.5\text{mJ/pulse}$). This pulse is split off before the internal compressor of the amplifier system to be used as pump/Stokes pulse. An external compressor is used to generate a near-transform-limited $\tau_{p/S} = 35\text{fs}$ duration pulse. The external compressor allows for flexible compensation (pre-chirping) of dispersion terms along the optical path. Hereby, the realisation of impulsive excitation is ensured. Where chirp describes the order of different frequencies in the time-domain. The arrival time is controlled by an automated translation stage (Thorlabs, sub- 10fs resolution) to account for the path length difference between the pump/Stokes pulse and the probe pulse. The resulting pump/Stokes pulse has a bandwidth of $\lambda_{p/S} = 785\text{-}815\text{nm}$. The pump/Stokes pulse is focussed by a spherical lens ($f = 500\text{mm}$) before it is crossed with the probe pulse.

The laser beams are crossed at an angle of $\sim 3^\circ$. Half-wave plates (Eksma Optics) are inserted; half-wave plates are optical devices which alter the polarization of light. It serves three goals. Firstly, to satisfy the transmission axis of the gratings ($> 90\%$ diffraction efficiency at $\lambda = 400\text{nm}$, s-pol) for the probe pulse ($\lambda = 400\text{nm}$), secondly, to control the relative polarization of the pump/Stokes pulse ($\lambda = 800\text{nm}$) with respect to the probe pulse, and thirdly to turn the polarization of the CRS beam ($\lambda = 400\text{nm}$) to satisfy the transmission axis of the polarization beamsplitter and the grating of the spectrometer. The probe pulse needs to be removed before the detector plane to prevent damage to the detector.

The CRS signal is collimated with a spherical lens ($f = 400\text{mm}$). In combination with a transmission grating ($\sim 3040\text{l/mm}$, Ibsen Photonics) the two act as a wide-field coherent imaging spectrometer. With a sCMOS camera (Zyla 4.2, Andor) isolated spectral lines can be detected at 1000Hz . The sensor is optimised for light in the visible spectrum ($\lambda = 400\text{-}750\text{nm}$).

The experimental setup described here was designed to demonstrate two-beam fs/ps pure rotational CRS imaging at kilohertz refresh rate. It allows for temperature and relative species concentrations of oxygen and nitrogen in dynamic scenes [10].

3.5. Ultrabroadband CRS

For two-beam CRS the finite bandwidth of the fs pump/Stokes pulse determines the probability to excite different transitions. The difference in frequency between the pump and the Stokes photon need to match with the energy gap of specific transitions. The energy gap is described by Raman shift in wavenumbers. At high Raman shifts (the vibrational fingerprint region, $\Omega = 800\text{-}1400\text{cm}^{-1}$ [22]) the spectrum is less congested with spectral lines compared to low Raman shifts. Measurements in this high spectral region can ease the fitting procedure and give additional information on different molecules like for example carbon dioxide and molecular hydrogen. Commercially available ultrafast regenerative amplifiers cannot provide the bandwidths required to excite Raman transitions further than $\Omega \approx 400\text{cm}^{-1}$. In a two-beam CRS setup measurements in this spectral region require an ultrabroadband transform-limited pump/Stokes pulse, or in other words a supercontinuum.

Different options exist to create an ultrabroadband pulse. For example with laser-induced filamentation, a hollow-core fibre or with solid state materials. To explain which technique is more promising, consider the validation of a novel engine design. To validate simulations, one could build a combustor with an optical window to transmit laser pulses to the location of a measurement. If the ultrabroadband pulse is generated *ex-situ*, the pulses would be heavily chirped through the optical window. This would greatly decrease the excitation bandwidth. An *ex-situ* ultrabroadband generated pulse would require an additional external compressor to pre-chirp the pulse and compensate for the additional dispersion terms. The experimental setup would require the original external compressor to optimise the supercontinuum generation. The additional external compressor would be placed behind the location where the supercontinuum is created and before it is passed through the optical window. This could create a transform-limited supercontinuum behind an optical window. However, a change in the properties of the optical window or pulse energy would require recalibration of the system, therefore complicating the operation during experiments. Furthermore, the experimental setup would become more expensive as additional optical elements are required.

With *in-situ* supercontinuum generation the new frequencies are created behind an optical window. Here, the dispersion terms due to the optical window can be compensated for by the original external compressor. Therefore, the cost for the experimental setup is much lower. Not all techniques allow for *in-situ* generation. The generation of an ultrabroadband pulse with a hollow-core fibre or solid state materials require optical elements, they need to be placed outside the combustor. Fs-laser-induced filamentation can potentially create a near transform-limited pulse behind an optical window without additional optical elements. Fs-laser-induced filamentation is a non-linear optical process where light self-focuses induced by a change in refractive index due to intense electromagnetic radiation [56]. The technique does not require any additional optical elements. Therefore, supercontinuum generation via *in-situ* fs-laser-induced filamentation is proposed to extend the capabilities of two-beam fs/ps CRS. The experimental implementation is presented in [Section 4.5](#).

4

Theory on Femtosecond-Laser-Induced Filamentation

In this chapter theory on the generation of ultrabroadband laser pulses with femtosecond ($f_s = 10^{-15}s$) laser-induced filamentation is presented. Fs-laser-induced filamentation is a non-linear optical process which influences beam propagation and causes spectral broadening. Interestingly, in literature no consistent name exists for the creation of a supercontinuum, among the names are supercontinuum generation, superbroadening, ultrabroadband generation and transformation in white light. As with the wide range of names, no definition exists on the spectrum width and pulse quality of the generated pulse.

First, a description on the propagation of light is presented in [Section 4.1](#). In the section the phase and group velocity, and the refractive index are discussed. [Section 4.2](#) covers self-focusing by the Kerr-effect and [Section 4.3](#) covers how the Kerr-effect modulates the phase and creates new frequencies. Plasma generation is elaborated on in [Section 4.4](#). Then, an overview of the fs-laser-induced filamentation process is presented in [Section 4.5](#). Lastly, [Section 4.6](#) covers the experimental implementation of fs-laser-induced filamentation into the CRS setup.

4.1. Light Propagation

Phase and group velocity are two concepts of velocity which are associated with electromagnetic waves (light). Phase velocity describes the speed of the phase of one frequency component, where group velocity refers to the rate at which the envelope of the wave amplitude moves in space [\[35\]](#).

The phase velocity is described with [Equation 4.1](#) [\[35\]](#). Important to note is the fact that the phase velocity is dependent on the refractive index, later important for the effect of self-phase modulation.

$$v_p = \frac{c}{n} \quad (4.1)$$

Where v_p is the phase velocity, c is the speed of light, n is the refractive index. The group velocity can be described by [Equation 4.2](#) [\[35\]](#).

$$v_g = \frac{d\omega}{dk} = \frac{c}{n} \left(1 - \frac{k}{n} \frac{dn}{dk} \right) = v_p \left(1 - \frac{k}{n} \frac{dn}{dk} \right) \quad (4.2)$$

Where v_g is the group velocity, k is the wave-vector and ω is the angular frequency ($\omega = 2\pi f$). This shows that for a dispersionless medium ($dn/dk = 0$) the phase and group velocity are equal. For a medium with normal dispersion ($dn/dk > 0$) the group velocity is equal or smaller than the phase velocity. Where on the contrary, a medium with anomalous dispersion ($dn/dk < 0$) the group velocity is higher than the phase velocity. From Equation 4.2 it could be reasoned that the group velocity can be higher than the speed of light in vacuum. In such case, the group velocity does not represent the speed at which energy or information propagates [35].

The refractive index and the phase velocity are linked, the phase velocity in turn is linked to the group velocity. Therefore, the group velocity is not constant in a medium with dispersion. The group velocity varies along the length of the pulse. This type of dispersion is referred to as group velocity dispersion (GVD), it can be quantified with the GVD-parameter given in Equation 4.3 [33].

$$GVD = \left(\frac{d^2k}{d\omega^2} \right)_{\omega=\omega_0} = \left(-\frac{1}{v_g^2} \frac{dv_g}{d\omega} \right)_{\omega=\omega_0} \quad (4.3)$$

A transform-limited pulse will lengthen over time when placed in a dispersive medium. In a medium with positive group velocity dispersion the shorter wavelengths will travel slower than the longer wavelengths. This results in a positively chirped pulse. For a negative GVD parameter the opposite is true. Most importantly, both positive and negative GVD result in lengthening of a transform-limited pulse.

4.2. Kerr-Effect: Self-Focusing

To further explain fs-laser-induced filamentation, the refractive index needs to be considered. The refractive index is a dimensionless number that describes the speed of light through a material and can be quantified by rewriting Equation 4.1 to Equation 4.4.

$$n = \frac{c}{v_p} \quad (4.4)$$

Where v_p is the phase velocity. A wavefront (a set of all locations where the wave is in the same phase) where the central part of the beam has higher refractive index than the outer edge results in focusing of the beam. The wavefront curves towards the axis of propagation. For a convex lens, the distance the central part of a pulse travels inside the lens is longer compared to the distance the outer edge of the pulse travels inside the lens, due to the difference in thickness of the lens. In a lens the phase velocity is slower compared to air and thus has a higher refractive index causing the pulse to focus. In fs-laser-induced filamentation changes in the refractive index self-focus the beam. [56]

For electromagnetic waves with large amplitude of the electric field, the refractive index becomes a function of the Kerr-effect (Δn_{kr}) and the free-electron-effect (Δn_p) as shown in Equation 4.5 [56]. The Kerr-effect is a non-linear process which contributes to focusing of light. The free-electron-effect causes diffraction due to the interaction of light with a plasma. A plasma is an ionised medium, which is further elaborated on in Section 4.4.

$$n = n_0 + \Delta n_{kr} - \Delta n_p \quad (4.5)$$

Where n_0 is the refractive index of neutral air, $\Delta n_{kr} = n_2 I$ is the Kerr-term, and $\Delta n_p = \frac{4\pi e^2 N_e(t)}{2m_e \omega_0^2}$ is the free-electron-term. Rewriting the refractive index results in Equation 4.6 [56].

$$n = n_0 + n_2 I - \frac{4\pi e^2 N_e(t)}{2m_e \omega_0^2} \quad (4.6)$$

Where n_2 is the second-order non-linear refractive index which can also be expressed in terms of the third-order susceptibility as follows $n_2 = 3\chi^{(3)}/4n_0\epsilon_0c$ [33], I is the intensity of the pulse, $N_e(t)$ is the electron density, e is the electronic charge, m_e is the electron mass, and ω_0 is the central frequency of the pulse. From Equation 4.6 it follows that for a pulse with its maximum intensity in the centre of the wavefront, the refractive index of the centre of the pulse is higher. The higher refractive index in the centre curves the wavefront towards the axis of propagation. The pulse self-focuses.

It is important to note that Nurhuda et al. (2008) suggest that saturation of the non-linear susceptibility ($\chi^{(3)}$) is an effect which can contribute to diffraction of light during fs-laser-induced filamentation [57]. This can be accounted for by higher-order Kerr-terms [58]. Therefore, it is not by definition that the free-electron-effect has to play a role in the filamentation process [58]. However, this is deemed outside the scope of this description.

4.3. Kerr-Effect: Self-Phase Modulation

The self-focusing of the pulse results in a balance where the core size of the laser pulse stays almost constant. In the process, initially, the Kerr-effect will be leading. In time, a competing effect to the Kerr-effect which can be either the free-electron-effect or higher-order Kerr-terms will oscillate in strength resulting in a periodic balance. Normally, fs-laser-induced filamentation is explained with a balance between the Kerr- and free-electron-term ($\Delta n_{kr} \approx \Delta n_p$). The temporary balance which repeats in space is referred to as intensity clamping. The intensity is stabilised and becomes almost unaffected by the intensity of the input pulse. [59] Furthermore, the clamped intensity becomes independent of pressure [56, 60]. It is possible for a filament to re-focus multiple times, although eventually it breaks up and diffracts due to perturbations in the medium and the pulse [59]. The diffractionless propagation is called filament propagation, the location is named the filament.

Non-linear interactions between the laser pulse and the medium result in self-phase modulation (SPM). SPM refers to the variation in refractive index which produces a phase shift and eventually spectral broadening. The light is red- ($f \downarrow$) and a blue-shifted ($f \uparrow$). To further explain the concept of fs-laser-induced filamentation, the pulse is approximated by a plane wave. The intensity of the laser pulse is not equal for all plane waves inside the pulse. Consider three slices of the pulse, one at the back, one in the middle and one at the front of the pulse as shown in Figure 4.1. The intensity of the centre slice is highest compared to the other slices, the intensity gradually decreases towards the front and back of the pulse as outside the pulse the intensity is zero. The high intensity in the centre of the pulse leads to the strongest Kerr-effect as the effect is linearly dependent on the intensity. Hereby, the centre slice will reach the intensity clamping condition first.

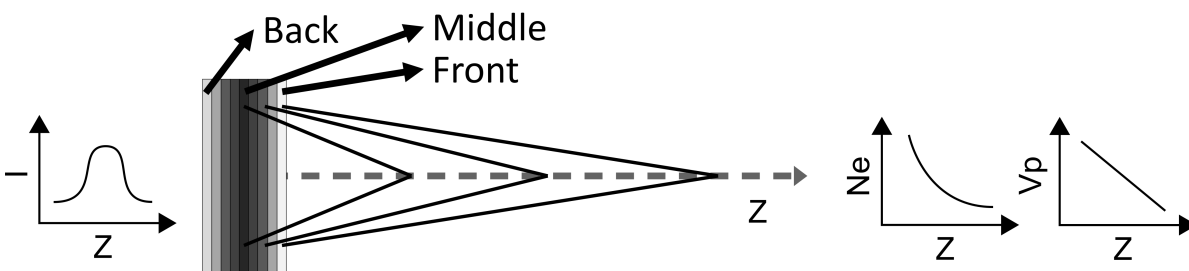


Figure 4.1: Illustration of slice-by-slice self-focusing. Figure is inspired by schematic of Chin et al. (2008) [61]. Three figures are presented with an indication of the trends of intensity, number density and phase velocity versus position.

The front part of the pulse did not reach the intensity clamping condition yet, here the Kerr-effect is leading. The refractive index of the front slice is higher compared to the later slices as no plasma has been created by the pulse in the medium. The refractive index is linked to the phase velocity by $n = c/v_p$, the phase velocity of the front slice hereby is lower than the centre slice. Oppositely, the back part of the pulse moves through a medium where some plasma has been created. Here, the free-electron-term is larger than the Kerr-term. Therefore, the back slice diverges and catches up

with the centre slice. All in all, decreasing the total length of the pulse. Therefore, the intensity of the centre slice is reached in a smaller period of time, the intensity gradient increases. The intensity gradient gives rise to spectral broadening. A white light chirped laser pulse is generated. The back part of the laser pulse will initially decrease its intensity. After some time, the back part will re-focus as the intensity will increase when it gets closer to the centre slice. [56]

As the intensity does not further increase with more input power, an increase in energy will in an ideal situation result in a larger filament core, its intensity will remain clamped [62]. In practice, this can be difficult to get as small local perturbation in the laser intensity will lead to local self-focusing. An increase in the size of the filament core can only be achieved when the quality of the input laser is high and few perturbations in the experimental setup exist.

The mathematics behind SPM are not discussed here, but are covered in other work, for example Boyd (2008) [33] and Chin (2010) [56]. In Chin (2010) [56] a plane wave approximation is made, Equation 4.7 follows from this approach. Here, it can be noted that the slope of the intensity determines the direction of frequency change. The front slice has a positive intensity slope, here lower frequencies (red shift) are created. The back slice has a negative intensity slope, here higher frequencies (blue shift) are created

$$\Delta\omega = -\frac{\omega_0 z}{c} n_2 \frac{\partial I}{\partial t} \quad (4.7)$$

Where z is the length of the filament and $\frac{\partial I}{\partial t}$ is the derivative of intensity with respect to time.

The description above describes SPM with the plane wave approximation, here only the properties of the pulse in the direction of propagation (z -axis) are considered. However, the properties of the pulse and the medium vary in both the direction of propagation (z -axis) and the radial (r -axis) direction. The two-dimensional physics result in conical emissions as shown in Figure 4.2. Sometimes, black rings can be observed in between conical emissions. Those arise from destructive interference of different filaments on the same axis. [56]

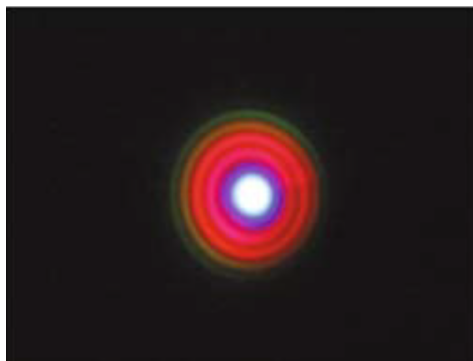


Figure 4.2: Conical emissions of filament captured with consumer digital camera, picture is 20 cm in width [56].

In the experimental setup, the filamentation process is used *in-situ*. Meaning that the filament is positioned near the probe volume, inside the flame. The flame is provided on a Bunsen burner with a smaller radius than the filament. The filament starts well outside the flame where the temperature is still low and moves inside the flame where the temperature is close to adiabatic flame temperature. The filament travels over a large gradient in temperature. The large gradient in temperature goes accompanied with a large gradient in number density. The number density decreases rapidly. Furthermore, the gas composition changes. Fs-laser-induced filamentation is a function of these gas characteristics. No research exists where such large gradient in boundary conditions are applied. In the experimental campaign, the effects of the large gradient on the spatial dimensions of the filament are studied.

4.4. Plasma Generation

A plasma is a medium made of ions and free electrons. This is the fourth fundamental state of matter, next to the solid, liquid and gaseous state. A plasma can be created by ionization, this process converts electrically neutral atoms or molecules to electrically charged atoms or molecules. Electrons are emitted from the atoms or molecules. In the experimental setup a photon does not have enough energy to directly ionise a molecule or particle. Two processes exist which can cause ionization; multiphoton ionization (MPI) and tunnel ionization.

MPI is the process where multiple photons below the ionization threshold combine their energies to ionise. As the process requires multiple photons the probability is strongly correlated to the intensity of the light. The other possibility is tunnel ionization, here the potential barrier is distorted such that electrons can pass through the ionization barrier. The potential barrier can be distorted by a strong electric field.

To distinguish which effect is leading the Keldysh (adiabatic) parameter γ can be used, the Keldysh parameter is described by Equation 4.8 [63]. From experimental findings, it has been found that when $\gamma < 0.5$, it is said to be in the tunnel ionization regime, and when $\gamma > 0.5$, it is said to be in the MPI regime [64]. The experimental setup is in the MPI regime.

$$\gamma = \frac{\omega}{F} \sqrt{2E_0} \text{ (in atomic units)} \quad (4.8)$$

Where ω is the frequency of the laser, F is the laser electric field strength, and E_0 is the ionization potential of the atom. Energy from the laser pulse is lost, because of the ionization process. In Section 5.1 the efficiency of the filamentation process is quantified.

The plasma channel is visible by naked eye due to N_2+ fluorescence. Fluorescence is the emissions of electromagnetic radiation from particles. In the plasma channel N_2+ emits light at $\lambda \approx 391$ and $428nm$ [65–67]. In the experimental campaign, the N_2+ fluorescence is used to characterise the position of the filamentation process. Furthermore, it is used to find the focal point.

4.5. Femtosecond-Laser-Induced Filamentation

A schematic of fs-laser-induced filamentation is presented in Figure 4.3. A laser pulse is represented by the black-coloured circle on the left, the pulse moves towards the right. The cone shows a decreasing size of the laser beam, the laser self-focuses. Further downstream, a filament is created. In the experimental setup a plasma is present in the filament, this is sometimes referred to as the plasma channel. Energy from the pulse surrounds the filament, this region is called the background reservoir. The filament interacts with the energy contained in the background reservoir [56]. The end product is white light surrounded by conical emissions. The light in the centre is white, because it contains many different frequencies.

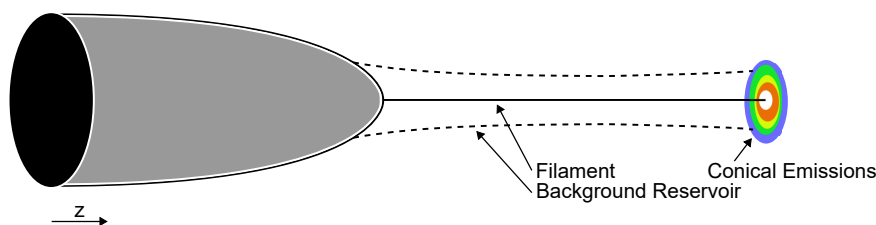


Figure 4.3: Schematic of laser pulse undergoing self-focusing. Figure is inspired by schematic of Chin et al. (2005) [68].

4.6. Experimental Implementation

As mentioned earlier, supercontinuum generation via *in-situ* femtosecond-laser-induced filamentation for ultrabroadband femtosecond/picosecond coherent Raman spectroscopy (CRS) is used in this thesis. The filament is placed near the probe volume where the pump/Stokes pulse is crossed with the probe pulse. A schematic of the experimental implementation is shown in Figure 4.4. The remaining part of the experimental setup is unchanged and has been presented in Section 3.4. The pump/Stokes pulse and probe pulse are focused by spherical lenses ($f_{p/S} = 500mm$, $f_{Pr} = 300mm$). The pulses are crossed as follow. The probe pulse is in the focus, such that the intensity is highest. The pump/Stokes pulse is diverging out of the filament, such that all newly generated frequency can be used and ionization in the probe volume is avoided. The effects of placing the probe volume in the filament on CRS thermometry are studied in Section 7.2.

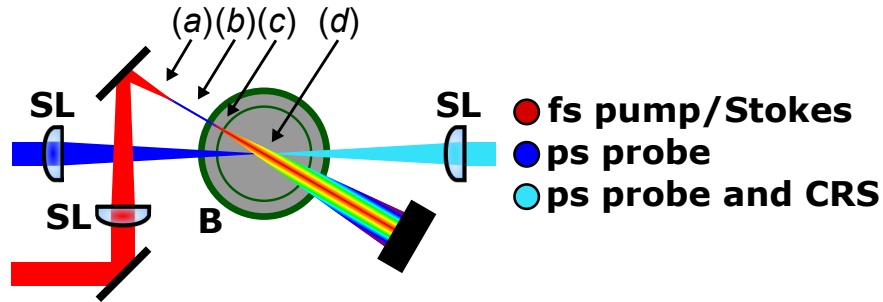


Figure 4.4: Schematic of experimental implementation of *in-situ* femtosecond-laser-induced filamentation for ultrabroadband femtosecond/picosecond coherent Raman spectroscopy (CRS). The pump/Stokes pulse ($f = 500mm$) and the probe pulse ($f = 300mm$) are focused by spherical lenses (SL), the pump/Stokes pulse is aligned with the probe pulse by two mirrors. (a) After the last mirror the pump/Stokes pulse self-focuses. (b) A filament forms, the plasma channel is visible by naked eye due to N_2^+ fluorescence. (c) Here, new frequencies have been created by self-phase modulation and the pump/Stokes pulse diverges out of the filament. (d) the pump/Stokes pulse and probe pulse are crossed, an ultrabroadband femtosecond/picosecond CRS signal is created. B, burner; SL, spherical lens.

5

Characterisation of Femtosecond-Laser-Induced Filamentation

In the previous chapters theory from the literature has been presented on coherent Raman spectroscopy (CRS) and supercontinuum generation via femtosecond ($f_s = 10^{-15}$) laser-induced filamentation. In the next three chapters the experimental work is presented. The work consists of an experimental campaign which is split into three phases. The goal of the campaign is to characterise fs-laser-induced filamentation and the effects of fs-laser-induced filamentation on two-beam femtosecond/picosecond ($ps = 10^{-12}s$) CRS.

In this chapter the first experimental phase is presented, here fs-laser-induced filamentation is characterised. This includes the measurements of the spatial properties of the plasma channel, the power required to initiate the fs-laser-induced filamentation process and the effects of different boundary conditions on the excitation efficiency. The second experimental phase is presented in [Chapter 6](#) and covers the characterisation of the probe volume dimensions. Here a novel procedure is demonstrated to find the pump/Stokes pulse diameter in the probe volume under filamentation conditions. The third experimental phase is presented in [Chapter 7](#) and contains measurements to characterise the effects of fs-laser-induced filamentation on CRS thermometry. This phase includes a demonstration of ultrabroadband fs/ps CRS behind an optical window. The report is structured per experiment, meaning that the methodology, results and conclusions of one experiment are presented all at once. For some experiments additional theory is provided.

This chapter is structured as follows. Firstly, the efficiency of the supercontinuum generation via fs-laser-induced filamentation is discussed in [Section 5.1](#). Here the average power before and after the filament is measured in different gas mixtures. Secondly, the spatial properties of the filament are studied in [Section 5.2](#). Thirdly, the power required to initiate the fs-laser-induced filamentation process is measured in [Section 5.3](#). Then, a model for the non-resonant CRS signal is presented to characterise the pulse duration in [Section 5.4](#). In [Section 5.5](#) the excitation efficiency is characterised with the pulse duration for different boundary conditions. The tested boundary conditions are the amount of chirp produced by the external compressor, the input power, the gas composition, the gas temperature, and finally the effect of a flame.

5.1. Efficiency of Filamentation Process

The efficiency of supercontinuum generation via fs-laser induced filamentation can be characterised by comparing the average power before and after the filament. The difference shows the losses of the filamentation process due to multi-photon ionization. The average power is measured with a power meter.

5.1.1. Results

The input pump/Stokes pulse energy is varied between 300 and 1500 μJ . The efficiency curve for different input energies is shown in Figure 5.1. The slopes of the respective lines are used to describe the efficiency of the filamentation process. The dashed line has a slope of 45 deg, which represents the ideal case where no energy is lost. The energy conversion efficiency for the laminar premixed methane/air flame, air and molecular nitrogen is $\eta = 86.5, 82.2,$ and 82.2% respectively.

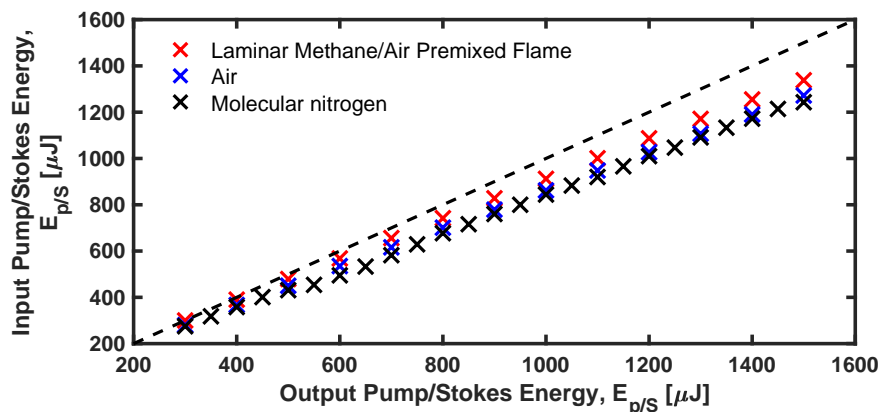


Figure 5.1: Conversion efficiency of the filamentation process in different gasses with pump/Stokes pulse energy in the range of 300 – 1500 μJ . Output of filament is generated in molecular nitrogen and air are at room temperature, and in the products of a laminar premixed methane/air flame.

The experiment shows only small differences in efficiency between different gas compositions and overall a small loss. In the flame a higher conversion efficiency is observed, this can be explained by the lower ionization rate due the lower density in the hot gas mixture compared to the denser gas mixtures at room temperatures. It can be concluded that most energy is preserved for CRS measurements.

5.2. Dimensions of Filament

The spatial dimensions of the filament vary from pulse to pulse. In the literature it is not described whether the end position of the filament changes with temperature. The initial crossing of the beams is normally optimised in air at room temperature. Changes of the gas composition and temperature could result in a shift of the filament position with respect to the probe volume position. All of the named changes lead to an uncertainty of the filament position with respect to the probe volume position.

In this experiment the spatial dimensions of the filament and its variation in time under three boundary conditions are evaluated. The variation in time is named the spatial jitter. Firstly, the filament is placed in air at room temperature. Secondly, part of the filament is placed inside a laminar methane/air premixed flame provided on a Bunsen burner. This flame setup is typically used for experiments. Special focus is on this setup, because the filament propagates over a region with a large gradient in temperature and thus number density. Lastly, the full filament is placed inside the same flame.

5.2.1. Methodology

The dimensions of the filament are captured by placing a consumer complementary metal oxide semiconductor (CMOS) camera (Nikon D7500) perpendicular to the filament. The filament is visible by naked eye due to N_2+ fluorescence. Electromagnetic radiation from molecular nitrogen at $\lambda \approx 391$ and $428nm$ is emitted [65, 66]. The experimental setup is displayed in Figure 5.2. During the experiment, the energy per pulse of the pump/Stokes laser ($\lambda = 800nm$) is set to $E_{p/s} = 1.5mJ$. The pump/Stokes pulse is focused by a $f = 500mm$ lens.

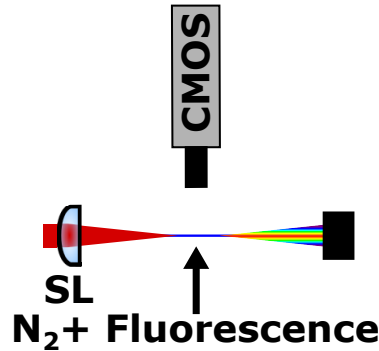


Figure 5.2: Schematic of experimental setup for imaging of N_2+ fluorescence with Nikon D7500 (CMOS). Implemented for imaging in flames and calibration of $2f$ telescope with sCMOS (see Section 5.3). SL, spherical lens.

The exposure time of the camera is set to $1/1000s$, equal to the repetition rate of the laser amplifier system. The maximum frame rate of the camera is 8 frames per second. Therefore, the figures do not give information in the time domain, especially because two consecutive filaments are uncorrelated. Two consecutive filaments are uncorrelated, because the electron-ion recombination timescale is in the order of nanosecond [69] which is much shorter than the millisecond timescale of the regenerative amplifier system ($1kHz$). The camera is calibrated by placing a ruler at the position of the filament. The ruler is placed in the focus of the camera. This results in a resolution of $\sim 24\mu m/pixel$. The experiments inside the combustion environment are performed with a laminar methane/air premixed M-flame.

In post-processing, the flame is removed from the pictures to find the integrated intensity profile of the N_2+ fluorescence. The intermediate steps of the post-processing are presented in Figure 5.3. The filament is the horizontal white line. On the right the blue flame is visible. The procedure to remove the flame is as follows. Firstly, from every colour column (line perpendicular to filament) the mean value of the first and last few pixels are subtracted. Secondly, the image is converted to grey scale (see Figure 5.3c). There is still some noise where the background subtraction was unsuccessful. The main noise consists of small isolated regions. The background subtraction is most difficult at the boundaries of the flame. There, the background intensity along one column is not constant. This is because, at the boundaries of the flame the fluorescence is sloped.

The next step is to remove pixels which are isolated. Or in other words, small objects are removed (see Figure 5.3d). This leaves the filament with some extra tails in the vertical direction at the boundaries of the flame. To remove these, the outer edge of the filament is found by calculating the vertical derivative of the intensity. The edge is fitted with a quadratic function. Everything outside of this range is removed (see Figure 5.3e). Lastly, the image is vertically binned and the horizontal length (length, $1/e^2$) is determined. Where (length, $1/e^2$) describes the intensity at the pulse boundaries, the horizontal length is defined as the length between two points with $1/e^2 \approx 0.14$ of the maximum intensity value. The procedure is applied to every individual frame, hereby the spatial jitter can be quantified.

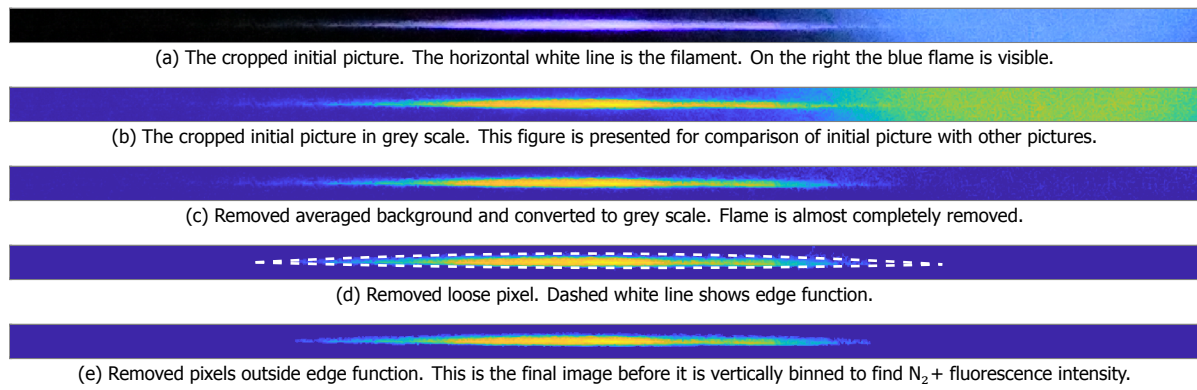


Figure 5.3: Post-processing procedure to remove the flame from the pictures and find the N_2+ fluorescence intensity profile. Example shows picture where part of filament is placed in laminar premixed methane/air m-flame.

5.2.2. Results

Typical pictures for the three environments without post-processing are shown in Figure 5.4. The focusing lens is positioned on the left side, the pulse moves from left to right. The straight horizontal line is the N_2+ fluorescence from the filament. The laminar premixed methane/air M-flame is shown as a light blue area present in Figure 5.4b and 5.4c. A graph of the normalised post-processed fluorescence is projected on the figure. The vertical dashed lines represents the mean horizontal length (length, $1/e^2$) of the filament for 275 pictures. Its standard deviation is displayed with the greyed filled area.

Some observations. Firstly, the filament which is partly placed inside the flame (Figure 5.4b) shows no major difference with the other figures. It is quite interesting that the filament is unaffected, while the filament passes a large gradient in temperature. The filamentation process starts well outside the flame and moves inside the flame. The large gradient in gas temperature is accompanied by a large gradient in number density. As the temperature increases, the number density of the gas-phase medium reduces. It should be noted that the N_2+ fluorescence decreases more rapidly where the flame starts.

Secondly, it can be observed that the data inside the flames is more noisy. The N_2+ fluorescence intensity profile is less smooth. In these cases, the flame adds extra uncertainty in post-processing. Therefore, the background subtraction is less successful.

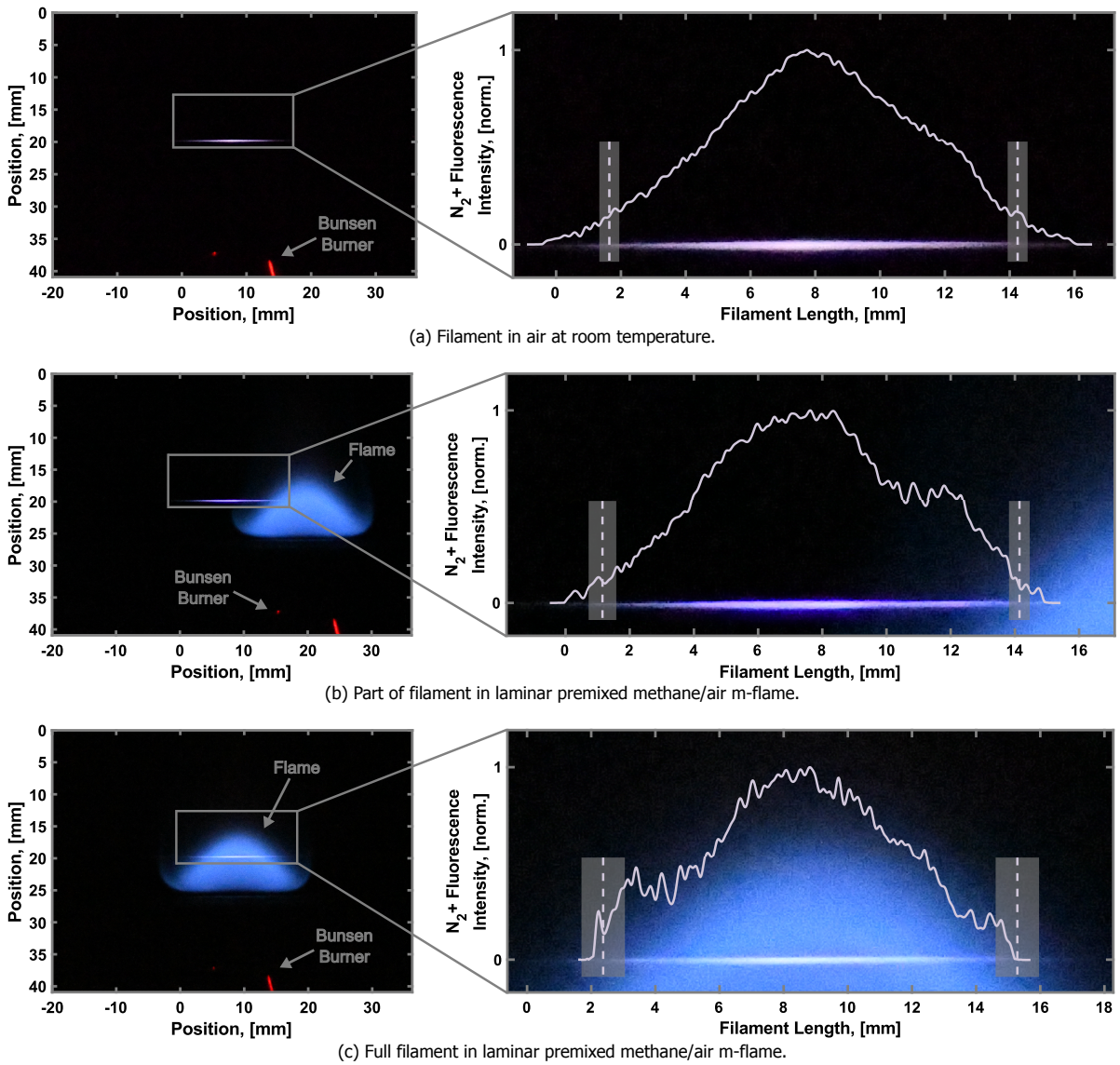


Figure 5.4: Picture of N₂+ fluorescence in different environments acquired with CMOS camera. Power of pump/Stokes pulse set to $E_{p/S} = 1.5mJ$ per pulse. The origin of the horizontal axis is arbitrary. Vertical dashed lines shows mean edge, with grey area representing its standard deviation. The horizontal line is the filament, with the fluorescence intensity profile placed on top. The blue colour is the laminar premixed methane/air m-flame.

The spatial dimensions of the filament are presented in Table 5.1. Surprisingly, the spatial dimensions are hardly affected by the presence of the flame. The spatial dimensions are stable with temperature. Furthermore, the filamentation process continues over the large gradient in temperature and number density, the filament is not stopped at the large gradient. Therefore, it seems that the intensity clamping condition ($\Delta n_{kr} \approx \Delta n_p$) is not dependent on temperature. Both the Kerr-effect (Δn_{kr}) and the free-electron-term (Δn_p) are affected equally such that the balance is unchanged.

Table 5.1: Dimensions (length, $1/e^2$) of filament in different environments. Populations size is $n = 275$. the origin of the length axis is arbitrary.

	Start	σ_{Start}	End	σ_{End}	Length	σ_{Length}
Room Temperature Air [mm]	1.67	0.33	14.24	0.30	12.56	0.28
Part of Filament in Methane Flame [mm]	1.21	0.44	14.13	0.39	13.10	0.45
Full Filament in Methane Flame [mm]	2.40	0.70	15.29	0.67	12.99	0.67

The standard deviation increases due to the influence of the flame. The end position of the filament varies in between $\sigma_{\text{End}} = 0.3$ and 0.7mm . The increase in precision is most likely due to additional uncertainties in the flame background and not due to the increase in temperature. The flame itself is not stable in time. Therefore, the background moves in time, this affects the successfulness of the post-processing procedure. All in all, this means that the real impact on the CRS process is small, as the spatial jitter of the filament hardly changes due to the presence of the flame.

5.3. Measurement of Critical Power in Air

The onset of the filamentation process changes the characteristics of the pump/Stokes pulse. For a pulse to undergo self-focusing the optical power needs to exceed the critical power, for a Gaussian continuous-wave laser the critical power can be described with Equation 5.1 [33].

$$P_{\text{cr}} = \frac{(0.61)^2 \pi \lambda^2}{8 n_0 n_2} \quad (5.1)$$

Where λ is the central wavelength of the pulse, n_0 is the refractive index of neutral air, and n_2 is the second order refractive index of air. In literature, the second order refractive index is reported on with different measurement techniques. A wide range of second order refractive indices have been presented ($n_2 = (1.2-5.57) \cdot 10^{-23} \text{m}^2/\text{W}$) [70, 71]. This range in refractive indices results in a range of critical powers according to Equation 5.1. For a central wavelength of 800nm the critical power ranges from $P_{\text{cr}} = 1.7$ to 7.8GW , or $E_{p/S} = 101$ to $468\mu\text{J}$ for a pulse duration of $\tau = 60\text{fs}$.

The focal point of the laser pulse can be used to determine the onset of the Kerr-effect. The focal point shifts towards the focusing lens at powers higher than the critical power. The focal point is reached at a shorter distance and shifts towards the focusing lens. This shift can be described with the transformation formula presented in Equation 5.2 [72, 73]. f' is the position of the focal point when the contribution from the geometrical focusing (the lens) and the filamentation process are combined.

$$f' = \frac{f \cdot z_{sf}}{f + z_{sf}} \quad (5.2)$$

Where f is the focal length of the focusing lens. z_{sf} is the self-focusing distance of the parallel Gaussian, z_{sf} is described with Equation 5.3 [74].

$$z_{sf} = \frac{0.367 k_0 a^2}{\left\{ \left[\left(\frac{P}{P_{\text{cr}}} \right)^{1/2} - 0.852 \right]^2 - 0.0219 \right\}^{1/2}} \quad (5.3)$$

Where k_0 is the wavenumber, a is the radius of the beam profile ($1/e$). The term $k_0 a$ indicates the diffraction length. Most important is that if the power is lower than the critical power, the focal point is constant with power.

5.3.1. Methodology

The focal point is measured with the experimental setup displayed in Figure 5.5. The fluorescence is imaged with a $2f$ telescope, a spherical lens ($f = 100\text{mm}$) is used. The experimental setup is changed as compared to Section 5.2. A scientific CMOS (sCMOS) camera is used instead of a CMOS camera. The benefits are twofold. Firstly, the repetition rate of the CMOS camera is a 1000 frames per second, equal to the repetition rate of the laser. This reduces the required time for a measurement. Secondly, the sensitivity of the sCMOS camera is higher.

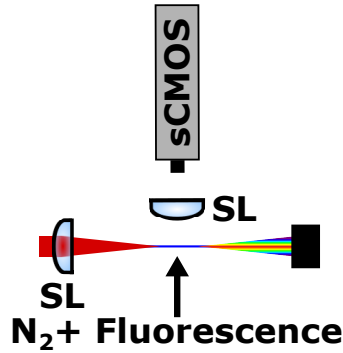
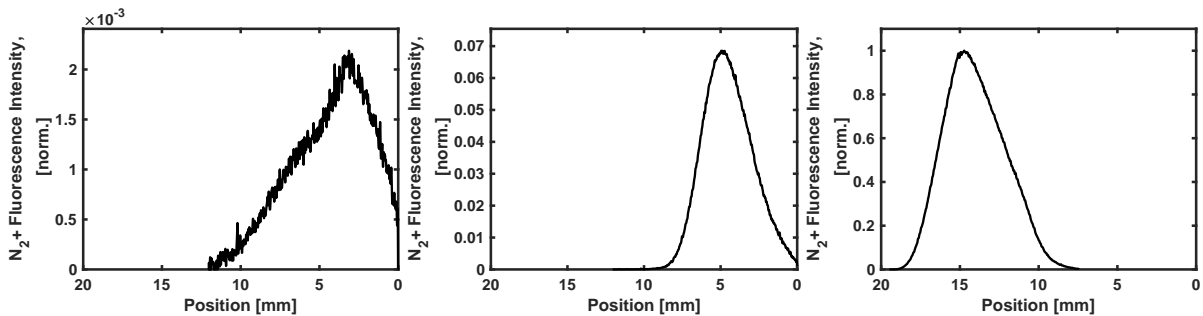


Figure 5.5: Schematic of experimental setup for imaging of N_2+ fluorescence. Imaging with Andor Zyla 4.2 (sCMOS) in $2f$ telescope. SL, spherical lens.

The system is calibrated with the experimental setup presented in Section 5.2. A filament is imaged with both the commercial CMOS camera and the sCMOS camera. The length of the filament for both measurements is equal. The pixel size of the commercial CMOS camera can be calibrated with a ruler as explained earlier. This results in a resolution of $\sim 6\mu\text{m}/\text{pixel}$ for the new experimental setup.

5.3.2. Results

The fluorescence observed perpendicular to the filament in air at room temperature is displayed in Figure 5.6. The figures show the summed intensity. In post-processing, Mie scattering from dust particles inside the optical path is removed from the data (see [35] for definition of Mie Scattering).



(a) $E_{p/S} = 40\mu\text{J}$; 150,000 pulses averaged. (b) $E_{p/S} = 150\mu\text{J}$; 150,000 pulses averaged. (c) $E_{p/S} = 1000\mu\text{J}$; 30,000 pulses averaged.

Figure 5.6: Averaged N_2+ fluorescence signal for three different energy levels. Positive position is towards the focusing lens with arbitrary origin. Please note that the positive direction of the x-axis is flipped. The intensity is normalised to the maximum intensity of $1000\mu\text{J}$.

N_2+ fluorescence is observed from pump/Stokes pulse powers of $E_{p/s} = 40\mu J$ and higher. The fluorescence is not symmetric. For powers above $E_{p/s} = 50\mu J$ the left hand side where the filament forms, has a steep curve. Where on the right hand side, where the filaments ends, a shallow curve is present. This could be due to the pulse deformation during the non-linear propagation [73, 75].

The peak of the fluorescence shifts towards the focusing lens. In Figure 5.6 this corresponds to a shift towards the left, or to a higher value on the horizontal axis. The focus shifts towards the focusing lens, because the Kerr-effect increases the speed of focusing. In post processing, a filter is applied to smoothen the fluorescence and find the peak position. The peak positions for different powers are displayed in Figure 5.7. The peak positions start to shift towards the focusing lens at $E_{p/s} = 74\mu J$. The pulse duration is $\tau_{p/s} \approx 60fs$ (see Section 5.4 and 5.5 for details), which gives a critical power of $P_{cr} \approx 74\mu J/60fs \approx 1.2GW$. Compared the critical powers calculated with different refractive indices at the start of this section ($P_{cr} = 1.7$ to $7.8GW$) this measurement of the critical power is low.

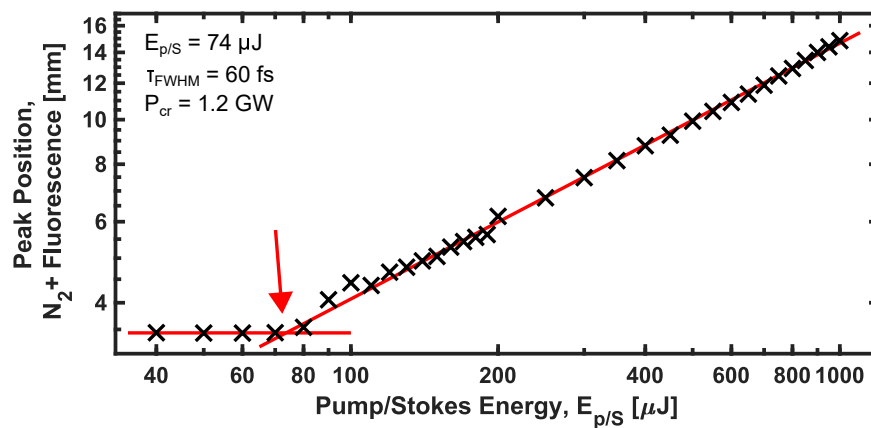


Figure 5.7: Direct measurement of critical power. Peak position of N_2+ fluorescence signal as function of pulse energy is presented. The crosses are experimental results, the straight red lines are fits used to determine the critical power. The origin of the vertical axis is arbitrary, positive peak position is towards the focusing lens. Please note that both axis are logarithmic scales.

An interesting observation can be made. Liu et al. (2005) report a critical power of $P_{cr} = 10GW$ in air ($\tau = 42fs$, $\lambda = 800nm$ and $f = 750mm$) [73]. Later, the same research group changed their experimental setup and report on a lower critical power inside a flame of $P_{cr} = 2.2GW$ ($\tau = 35fs$, $\lambda = 800nm$ and $f = 500mm$) [76]. Their direct measurement of the critical power inside a flame is presented in Figure 5.8. The experiment was performed with an experimental setup identical to ours; a Ti:Sapphire laser system which produces a $\tau = 35fs$, $\lambda = 800nm$ pulse focused by a $f = 500mm$ lens. Interestingly, the results in a flame (2016) look almost identical to our experimental results. The research presents a similar pulse energy for the onset of the Kerr-effect, namely $E = 74\mu J$. Li et al (2016) find their critical power low compared to their previous findings measured in air (2005), they speculate that a flame reduces the critical power. However, this experimental campaign suggest that, opposite to the authors suggestions, that the flame is not the main contributor to the change in critical power. This is further supported by results presented in Section 5.2. There, no clear difference in the dimensions of the filament are observed when the filament is placed in a methane/air premixed flame or when placed in air at room temperature ($L \approx 13mm$, $\sigma_{Length} = 0.3-0.7mm$ for $E_{p/s} = 1.5mJ$). Other changes in the experimental setup are more likely to influence the critical power. For example, the focal length was changed in between the different experiments. This seems to play a larger role.

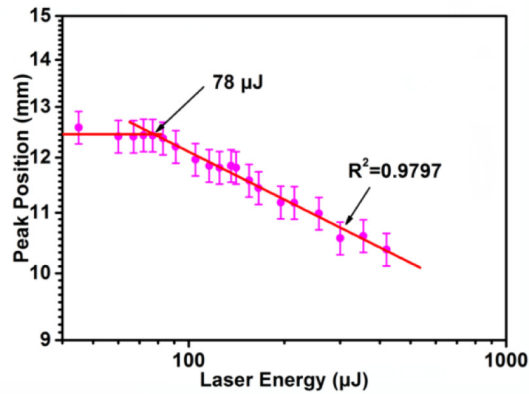


Figure 5.8: Li et al. (2016) present a direct measurement of critical power performed in ethanol/air flame [76]. Experiment is performed with a Ti:Sapphire laser system which produces $\tau = 35\text{fs}$, $\lambda = 800\text{nm}$ pulse which is focused by a $f = 500\text{mm}$ lens. In the figure a positive position is further from the focusing lens, the peak position shifts towards the focal length at higher powers.

Literature shows that ultrashort pulses have a higher critical power compared to longer pulses [73]. The critical power for ultrashort pulses becomes a function of pulse duration, because the molecular response is delayed [73]. As this experiment presents a critical power for an ultrashort pulse which is already low compared to literature, it shows that the critical power does not describe the onset of the filamentation process adequately.

Furthermore, in this experiment multiphoton ionization (MPI) is observed before the onset of the filamentation process. The experiment shows that the pure MPI regime ranges from $E_{p/s} = 40\text{-}74\mu\text{J}$. This regime has been previously described in literature [77]. However, the general description of the filamentation process found in many papers lacks to describe this regime. In literature critical power is used to describe the onset of the filamentation process. It is described how the Kerr-effect focuses the beam when the critical power is reached. The focusing effect decreases the waist of the beam. It is suggested that this decrease in beam waist increases the irradiance which initiates MPI. A plasma channel is formed. However, this research shows that the onset of ionisation is not directly linked to the onset of the Kerr-effect. There is no direct correlation. Also, in literature it is presented that the Kerr-effect is possible without ionization [58]. Here, higher-order Kerr-terms disperse the beam. For further research on the filamentation process it is advised to assume that ionisation and the Kerr-effect are independent of each other and do not start at the same pulse powers.

5.4. Estimate of Pulse Duration From Non-Resonant Signal

The time-bandwidth product of a pulse is the product of the temporal duration and the spectral width. The minimum time-bandwidth product is obtained for transform-limited pulses, for a Gaussian-shaped pulse the product has a minimum of ~ 0.44 . It is not possible to go below this limit. Such transform-limited pulses have minimum possible duration for a given spectral bandwidth. During the filamentation process the pulse is compressed and new frequencies are created. The output therefore resembles a transform-limited pulse, the pulse duration is used to quantify the increase in bandwidth. Hereby, only one characteristic value is needed. In two-beam CRS an increase in pump/Stokes pulse bandwidth can be observed by a flatter non-resonant normalised CRS spectrum. The resonances at higher Raman shifts can be measured more easily. A model for the non-resonant spectrum is created with the following set of equations and approximations.

Firstly, it is assumed that the probe pulse has no width in the frequency domain. The small width of the probe pulse compared to the larger width of the pump/Stokes pulse in the frequency domain makes this approximation possible.

The pump/Stokes pulse electric field envelop (E_0) is described in Equation 5.4. Here, the electric field envelop is a Gaussian. A transform-limited Gaussian is the theoretical output of the ultrafast amplifier system in combination with the external compressor.

$$E_0 = e^{\left(-2 \log(2) \left(\frac{t}{\tau_{p/s}}\right)^2\right)} \quad (5.4)$$

Where t is the time domain, and τ is the pump/Stokes pulse duration. The square of the electric field describes the intensity. The duration of the pulse is the full-width-at-half-maximum of the intensity profile. The pump/Stokes pulse electric field is described with Equation 5.5.

$$E = 2E_0 e^{-i\omega t} \quad (5.5)$$

Where ω is the angular frequency described with $\omega = 2\pi c/\lambda$, c is the speed of light, and λ is the central wavelength of the light.

The electric field in the time domain is transformed into the frequency domain with a Fourier transform. This gives a Gaussian in the frequency domain. To model the non-resonant CRS spectrum, the available photon pairs for different frequencies differences need to be counted. Or in other words, one needs to count which combinations of frequencies in the frequency spectrum are available to match a certain energy difference in between two energy states. Mathematically, this is represented by an autocorrelation of the frequency spectrum. An autocorrelation is a type of convolution, it is calculated by taking the integral of the product between the signal and a delayed copy of the signal which is shifted. This results in a synthetic spectrum for the non-resonant CRS signal.

A library is created from $\tau_{p/s} = 5$ to $100fs$ with $0.1fs$ step size. The signal can be scaled by multiplication of the entire field, this simulates different intensities. An optimization function is written to minimize the total residual in a specified spectral region. The function allows to fit individual frames.

5.4.1. Validation

To validate the model, the non-resonant coherent Stokes Raman spectroscopy (CSRS) spectrum is measured in argon. The spectrum is acquired at pump/Stokes pulse energy of 60 and $1000\mu J$.

The averaged experimental spectrum at $E_{p/s} = 60\mu J$ fitted with the model is presented in Figure 5.9. At this power the energy per pulse is too low to initiate the filamentation process. The residual is displayed at an offset of -0.2 . The mean pulse duration is estimated to be $\tau = 63.9fs$ long with a standard deviation of $\sigma_\tau = 0.9fs$. The pulse duration is long compared to the specifications of the laser amplifier system. The pulse should be approximately $\tau \approx 35fs$ long according to specifications. The difference can be explained by the chirp in the pulse. The non-resonant CRS spectrum is not generated with a transform-limited input pulse. The effect of pre-chirping is elaborated on in Section 5.5. At low powers, the shape of the synthetic and experimental spectra match nicely. The offset is relatively small. With model of the synthetic spectrum the effective transform-limited pulse duration can be estimated.

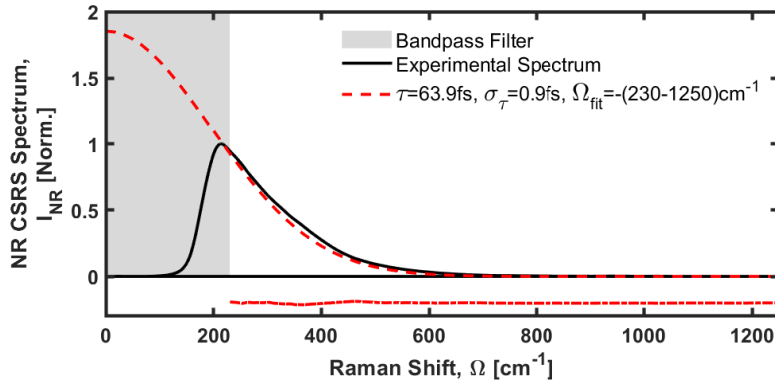


Figure 5.9: Averaged non-Resonant single-shot CSRS spectrum measured in argon with $E_{p/S} = 60\mu J$ (1000 frames). Model follows shape experimental spectrum nicely. The spectral fitting can be evaluated by the residual of the synthetic and experimental spectra, the residual is presented in the figure at an offset of -0.2 for clarity purposes. The grey filled area shows region where bandpass filter reduces strength of signal, the bandpass filter prevents damage to the camera.

The averaged experimental spectrum for $E_{p/S} = 1000\mu J$ fitted with the model is presented in Figure 5.10. The energy of the pump/Stokes pulse is large enough to initiate the filamentation process. A strong filament is created. A direct comparison of the non-resonant signal at low power (Figure 5.9) shows that the excitation efficiency at high Raman shift has increased, the increase in excitation efficiency with input power is further elaborated on in Section 5.5. The experimental spectrum is fitted in different ranges. It is not possible to fit the entire range at once. The shapes of the experimental and synthetic spectrum do not compare over the entire range. There are three ranges in the spectral window where the residual can be minimised. The effective pulse duration is affected strongly by the spectral region chosen. The estimated pulse duration for the three spectral regions is $\tau_{p/S} = 56.7fs$ ($\Omega_{fit} = 230-490cm^{-1}$), $\tau_{p/S} = 35.6fs$ ($\Omega_{fit} = 490-630cm^{-1}$), and $\tau_{p/S} = 29.2fs$ ($\Omega_{fit} = 630-1250cm^{-1}$). Clearly, there is a large difference between the model and the observed spectrum.

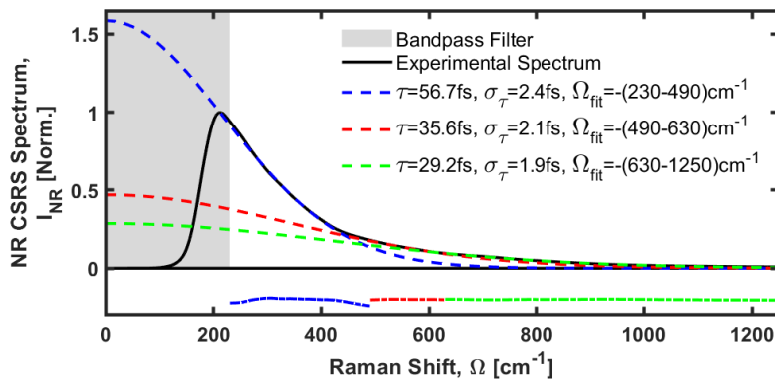


Figure 5.10: Averaged non-Resonant single-shot CSRS spectrum measured in argon with $E_{p/S} = 1000\mu J$ (1000 frames). The spectral fitting can be evaluated by the residual of the synthetic and experimental spectra, the residual is presented in the figure at an offset of -0.2 for clarity purposes. The grey filled area shows region where bandpass filter reduces strength of signal, the bandpass filter prevents damage to the camera.

The difference between the model and the experimental spectrum can be explained. The filamentation process increases the bandwidth of the pulse. The distributions of the frequencies flattens. Experimental results show that the increase in bandwidth is not symmetric [75, 78, 79]. However, the model assumes a Gaussian shaped pulse in the frequency domain. This assumption does not hold during measurements at powers above the critical power. A different input in the frequency domain would not solve the problem for all powers, as the spectrum in the frequency domain changes with different boundary conditions. Still, the model is used to quantify the increase

in pump/Stokes pulse bandwidth. Hereby, it is possible to show trends in specific spectral regions, it is not possible to compare the results of different spectral regions.

In [Figure 5.10](#) it is shown that a decrease in pulse duration results in a flatter non-resonant signal. The flatter signal allows for measurements at higher Raman shifts. It should be noted that the experimental spectra are less applicable for measurements across a large spectral region compared to the synthetic spectra. The slope of the experimental spectra are steeper. This means that the excitation efficiency at low Raman shift is much higher compared to the excitation efficiency at high Raman shifts. Therefore, it is difficult to prevent saturation of the camera at low Raman shifts while attaining a decent signal to noise ratio at high Raman shifts. For example, a measurement of molecular hydrogen S-branch would be difficult as the first 6 resonances range from $\Omega \approx 350$ to 1450cm^{-1} [[16](#)].

5.5. Effect of Boundary Conditions on Non-Resonant Signal

The non-resonant CRS spectrum is used to normalize the resonant CRS spectrum. The non-resonant signal changes when the filamentation process increases the bandwidth of the pump/Stokes pulse. The possibility to measure at higher Raman shifts is improved by this process. In this section the effects of different boundary conditions on the non-resonant spectrum are discussed.

The section is structured as follows. Firstly, the effect of pre-chirping is discussed in [Section 5.5.1](#). Secondly, the effect of power on the non-resonant spectrum is presented in [Section 5.5.2](#). Then the effect of gas composition and temperature are discussed in [Section 5.5.3](#) and [5.5.4](#), respectively. Lastly, the effect of combustion is elaborated on in [Section 5.5.5](#).

5.5.1. Effect of Pre-Chirping

The external compressor varies the chirp in the pump/Stokes pulse. It is implemented into the design of the experimental setup to compensate flexibly for dispersion terms along the optical path [[10](#)]. The external compressor can pre-chirp the pulse.

In [Section 5.4.1](#) it is shown that the pump/Stokes effective pulse duration without filamentation is $\tau_{p/S} \approx 60\text{fs}$. Compared to the specifications of the laser amplifier system of $\tau_{p/S} = 35\text{fs}$ this estimate seems to be too long. To further validate the model and to see the effect of different amounts of chirp inside the input pump/Stokes pulse on the filamentation process, the position of the external compressor is varied. The power is set to $E_{p/S} = 30$ and $1000\mu\text{J}$. The low energy case describes the effective input pulse duration during the filamentation process. This energy is well below the energy required to initiate the filamentation process ($E_{p/S} \approx 74\mu\text{J}$). The high energy case describes the output of the filamentation process. Hereby, it is possible to describe the effects of chirp in the input pulse on pulse compression via fs-laser-induced filamentation. In the literature, it is described how an increase in chirp reduces the critical power for ultrashort pulses [[73](#)]. No research is available where the effects of chirp in the input pulse on pulse compression are described, the experimental results are novel.

The external compressor has no discrete steps, therefore it is not possible to return to the same amount of chirp. The step size is determined by the manual input. The measurements are executed with the following procedure. First, the external compressor is moved towards negative chirp where the non-resonant signal is just visible. Further moving of the stage results in heavy modulations of the non-resonant signal. Then, for both powers, the non-resonant signal is measured. Next, the position of the external compressor is moved with a small step towards positive chirp. This procedure is repeated until heavy modulation of the non-resonant signal makes further measurements impossible.

The effective pulse duration measured in air at room temperature for different positions of the external compressor is presented in Figure 5.11. Positive position are associated with positive chirp. At position 1 and 13 it is not possible to fit the synthetic to the experimental data for $E_{p/S} = 30\mu J$ due to large modulations of the non-resonant signal. For a pump/Stokes pulse energy of $E_{p/S} = 1000\mu J$ two regions are fitted with the theoretical model. One fit ranges between $\Omega = 630$ and $900cm^{-1}$, the other fit ranges between $\Omega = 900$ and $1450cm^{-1}$. A fit for the entire measured spectrum was not possible due to a mismatch in the synthetic and experimental spectrum (see Section 5.4.1).

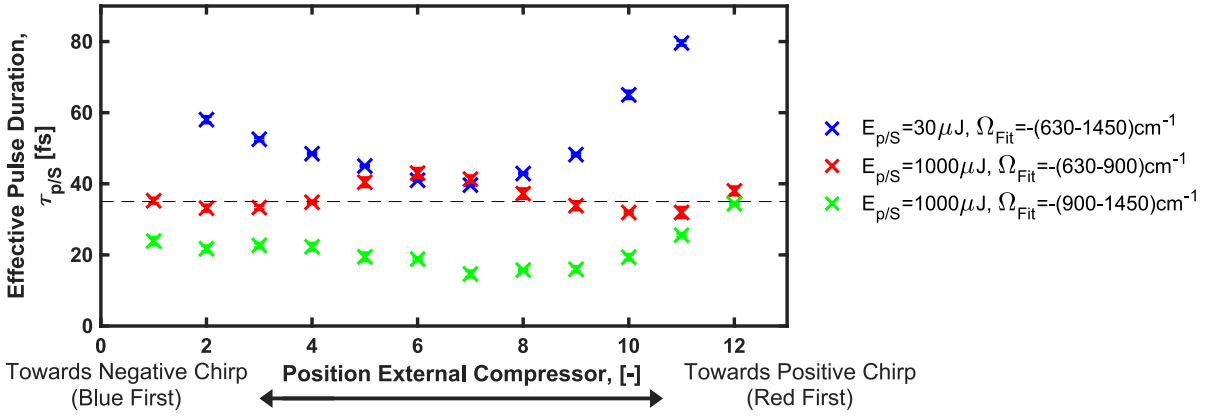


Figure 5.11: Effects of pre-chirping on pulse compression by the filamentation process in air at room temperature (1000 frames). $E_{p/S} = 30\mu J$ describes the input pulse, $E_{p/S} = 1000\mu J$ describes the output pulse of the filamentation process. On the horizontal axis positions of the external Compressor are displayed, positive position are associated with positive chirp. The origin is arbitrary. Please note that the horizontal axis is not completely linear, because the external compressor has no discrete locations.

At low energy, the effective pulse duration is minimal at position 7, here the effective pulse duration is $\tau_{p/S} = 39.6fs$ ($\sigma_\tau = 0.2fs$) which is close to the specified transform-limited pulse duration of the laser system ($\tau_{p/S} = 35fs$). At high energy, different optima can be observed. For the fit close to the probe pulse ($\Omega_{fit} = -(630-900)cm^{-1}$) there exist an optima at position 2 ($\tau_{p/S} = 33.1fs$, $\sigma_\tau = 0.9fs$) and 11 ($\tau_{p/S} = 31.9fs$, $\sigma_\tau = 1.5fs$). At those positions the input pulse duration is not transform-limited, but positively or negatively chirped to around $\tau_{p/S} \approx 60fs$ which is close to the pulse duration found in Section 5.4.1. For the fit further from the probe pulse ($\Omega_{fit} = -(900-1450)cm^{-1}$) the effective pulse duration is more flat for different positions of the external compressor. The global minimum is present close to transform-limited input pulse at position 7 ($\tau_{p/S} = 14.6fs$, $\sigma_\tau = 0.9fs$). Furthermore, a local minimum is located at position 2 ($\tau_{p/S} = 21.7fs$, $\sigma_\tau = 0.8fs$), the same location where a minimum is found for the fit close to the probe pulse.

Two methods are normally used to optimise the position of the external compressor during operation of the system. The first method is to look at the conical emissions from the filament (see Section 4.3 for theory on conical emissions). The position of the external compressor is changed such that the conical emissions have maximum intensity out of the filament. The second method is to optimise the non-resonant signal in the live feed of the sCMOS camera. The results show that optimisation of the external compressor during normal operation of the system does not result in a transform-limited input pulse. The optimisation results in either position 2 or 11 with an input pulse duration of approximately $\tau_{p/S} = 60fs$.

As mentioned before, the critical power reduces for an increase in chirp for ultrashort pulses [73]. Liu et al. (2005) show that for an increase in pulse duration from 42 to 200fs, the critical power drops from 10 to 5GW in air at room temperature. This can be explained as follows [71, 80]. The non-linearity in the medium consists of an instantaneous electronic response, and a delayed nuclear response. For longer pulses, the contribution of the delayed nuclear response is larger. It leads to a higher effective second-order refractive index (n_2). And therefore, a lower critical power.

The results presented in this section show that the input pulse duration for an optimal filamentation process is not transform-limited for a gas mixture with a nuclear response function. This is opposite to most optical phenomena where a transform-limited input pulse is most effective. Most likely, this has similar reasons why the critical power is reduced for a chirped input pulse. For longer pulses, the contribution of the delayed nuclear response is larger. The trend will most likely be different when the experiment is repeated in a gas mixture without delayed nuclear response function. An example of such gas mixture is argon, here a transform-limited input pulse is probably most optimal for pulse compression. Then the electric field intensity is highest, which results in the strongest instantaneous electronic response function.

The results shows the power of the novel methodology to estimate the pulse duration based on the non-resonant signal. It suggests that for a correctly assumed input pulse shape in the frequency domain, autocorrelation measurements are possible with a CRS system. The capabilities of a CRS system are increased without the need for any modifications to the setup. A user can note if the shape of the synthetic and experimental non-resonant signal do not match for measurements over a large spectral range ($\Omega_{fit} > 1000\text{cm}^{-1}$). If the shapes do not match, it points at an incorrect input shape in the frequency. Then, the results can not be used reliably to estimate the pulse duration. For further research it is advised to validate the experiments with an autocorrelator.

5.5.2. Effect of Input Power

In this section the effects of input power on the non-resonant CSRS signal and pulse compression are discussed. Averaged non-resonant CSRS spectra measured in argon for different pump/Stokes pulse energies are presented in Figure 5.12. The excitation efficiency increases at higher Raman shifts for increasing pump/Stokes pulse energies.

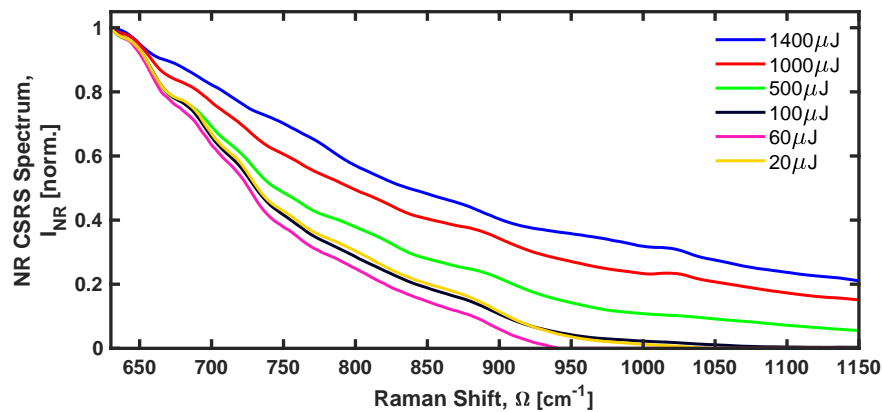


Figure 5.12: Averaged non-resonant single-shot CSRS spectrum measured in argon for different pump/Stokes pulse energy (1000 frames).

An estimate of the effective pulse duration for different powers is presented in Figure 5.13. The effective pulse duration decreases from $\tau_{p/S} = 40.1\text{fs}$ ($\sigma_{\tau} = 0.1\text{fs}$) to 24.5fs ($\sigma_{\tau} = 0.4\text{fs}$). The pump/Stokes pulse duration is compressed and the bandwidth is increased by the filamentation process. Quite surprising, the standard deviation of the pulse duration is small, the non-resonant CRSR signal is stable from shot-to-shot, although the filamentation process is highly non-linear. Apparently, small variations in the inputs do not result in large oscillations in the output. The experiment demonstrates that laser-induced filamentation can increase the bandwidth in the vibrational fingerprint region ($\Omega = 800\text{-}1400\text{cm}^{-1}$ [22]) such that thermometry in this less congested region is most likely possible.

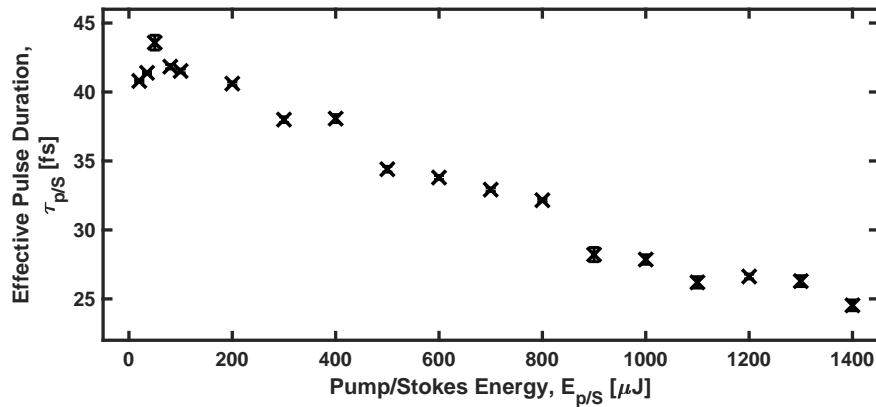


Figure 5.13: Estimate of effective pulse duration for different input powers (1000 frames). Pulse duration decreases with an increase in pump/Stokes pulse energy.

5.5.3. Effect of Gas Composition

In Figure 5.14 the effects of gas composition on the excitation efficiency for a range of pump/Stokes pulse energies is presented. The figures shows non-resonant CSRS spectra for air, argon, carbon dioxide and methane. The spectral region is chosen such that no resonant lines are present. The spectrum is calibrated with a resonant CSRS spectrum acquired in molecular hydrogen at room temperature.

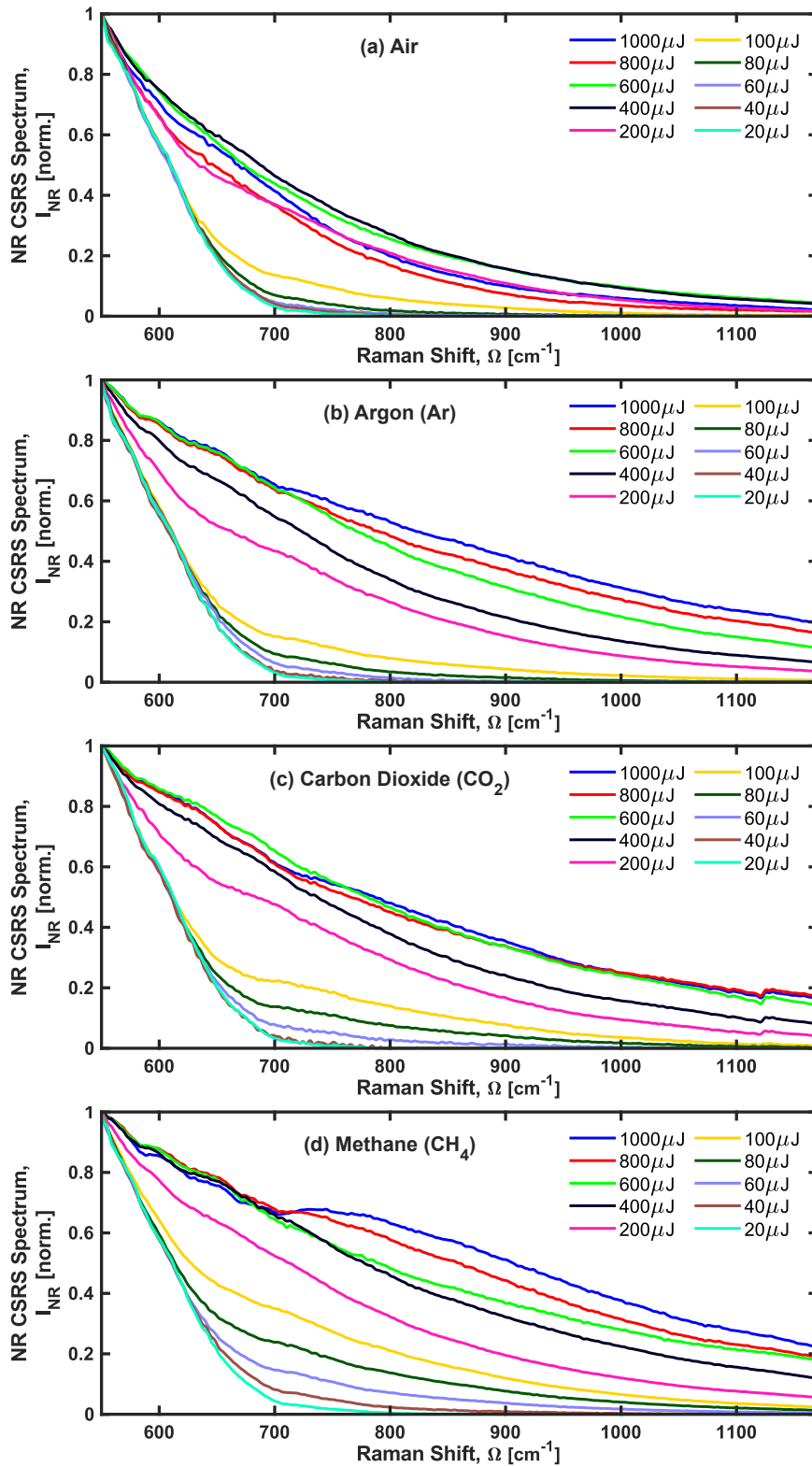


Figure 5.14: Averaged non-resonant single-shot CSRS spectrum measured for a range of pump/Stokes pulse energies in (a) air, (b) argon, (c) carbon dioxide and (d) methane at room temperature (1000 frames).

The main trend for all graphs is similar. From $E_{p/s} = 20\text{-}60\mu\text{J}$ the non-resonant signal is relatively constant for all gas compositions. No clear differences can be observed. For slightly higher powers, the pulse reaches critical power. The filamentation process starts and the excitation efficiency is increases.

For pulse energies of $E_{p/S} = 60\text{-}200\mu\text{J}$ the bandwidth increases rapidly with pulse energies. This corresponds to the critical power ($P_{cr} = 1.2\text{GW}$, $E_{p/S} = 74\mu\text{J}$) measured in Section 5.3. The onset of the broadening varies per gas composition. At higher powers, the excitation efficiency increases in more gradual steps.

Some spectral aspects are noteworthy. Firstly, the non-resonant CSRS spectrum acquired in methane shows a modulation from $\Omega = 700\text{cm}^{-1}$ onwards for $E_{p/S} = 800$ and $1000\mu\text{J}$. Secondly, the non-resonant CSRS spectrum acquired in air at high powers ($E_{p/S} > 400\mu\text{J}$) does not entirely grow with power. Or in other words, the excitation efficiency does not increase with power in this range. Thirdly, the curvature of the non-resonant signal acquired in air looks lower as compared to the other gas compositions. The excitation efficiency at powers above the critical power ($E_{p/S} = 74\mu\text{J}$) is lower. This is interesting, as the normal procedure for CRS thermometry involves normalisation in argon. A resonant air spectrum is normalised with a non-resonant signal acquired in argon. This would result in spectral cooling, as peaks at higher Raman shifts are normalised with a too large value.

An estimate for the effective Gaussian shaped pulse duration is shown in Figure 5.15. Here, the same trends can be observed. The pulse duration is around 60fs before compressions. In between $E_{p/S} = 60\text{-}200\mu\text{J}$ the pulse duration decreases rapidly with pulse energies. Here the filamentation process has started. At higher powers onwards, the effective pulse duration gradually becomes smaller with power.

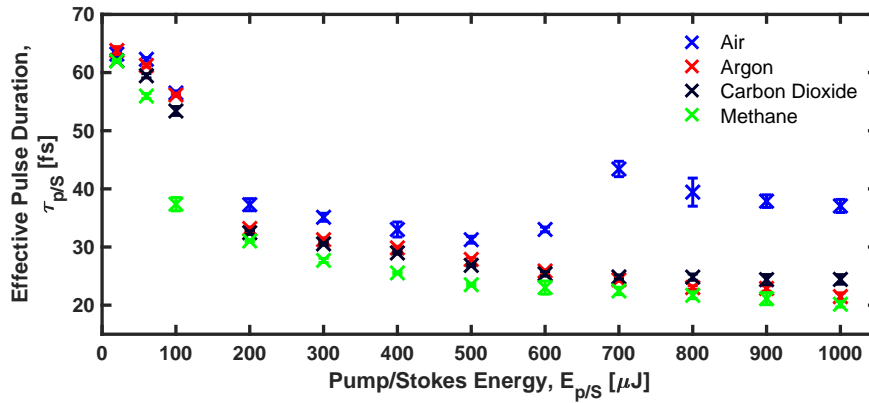


Figure 5.15: Estimate of effective pulse duration for several gas compositions at room temperature (1000 frames).

The combination of many non-linear processes determine the strength of the filamentation process. The pulse compression is dependent on many variables, among them is the third-order susceptibility and number density. To explain these effects a model is not available, but the dependency of different gas specific variables on pulse compression can be speculated.

Firstly, the non-resonant third-order susceptibility is reported on in literature for molecular nitrogen ($\chi_{NR}^{(3)} = 7.90 \cdot 10^{-18}\text{cm}^3/\text{erg amagat}$), oxygen ($\chi_{NR}^{(3)} = 7.98 \cdot 10^{-18}\text{cm}^3/\text{erg amagat}$), argon ($\chi_{NR}^{(3)} = 9.46 \cdot 10^{-18}\text{cm}^3/\text{erg amagat}$), carbon dioxide ($\chi_{NR}^{(3)} = 11.8 \cdot 10^{-18}\text{cm}^3/\text{erg amagat}$), and methane ($\chi_{NR}^{(3)} = 22.7 \cdot 10^{-18}\text{cm}^3/\text{erg amagat}$) [81]. Air can be approximated as a combination of the oxygen (21%) and nitrogen (79%). This gives an approximate non-resonant third-order susceptibility of $\chi_{NR}^{(3)} = 7.92 \cdot 10^{-18}\text{cm}^3/\text{erg amagat}$. The experiments show that the higher the non-resonant third-order susceptibility, the larger the pulse compression. However, the dependence of the non-resonant third-order susceptibility and pulse compression is not strong. The large difference in pulse compression between air and the other gas compositions is not fully explained. Furthermore, at higher powers a different trend is visible ($E_{p/S} = 700\text{-}1000\mu\text{J}$), the effective pulse duration of argon becomes smaller than the effective pulse duration of carbon dioxide. The reason for this behaviour is unknown.

Secondly, another possibility to characterise the differences in pulse compression is the number density. Number density is a count for the number of particles per unit volume. The number of particles can be described in mol ($N_A = 6.02 \cdot 10^{23}$ particles per mol). The number density at $T = 273K$ and $1atm$ of air, argon, carbon dioxide and methane are 42.46, 44.56, 44.76, and $44.88mol/m^3$ respectively. Up to $E_{p/s} = 700\mu J$ the order of pulse duration follows the same trend. Meaning that the chemical compositions with higher number densities have larger pulse compression, or a lower effective pulse duration. The larger difference between the pulse duration measured in air and the other gas compositions is better explained by the number density than the non-resonant third-order susceptibility.

Most probably, the effect is described by a combination of the third-order susceptibility and number density. Thermometry performed with normalisation in a different gas compositions will result in spectral heating and cooling. Up to $E_{p/s} = 700\mu J$ the data shows that normalisation in a gas with higher number density and non-linear susceptibility will result in spectral cooling. Normalisation in a gas with a lower number density and non-linear susceptibility will result in spectral heating. The discussion on spectral heating and cooling is further continued in [Section 7.3](#).

5.5.4. Effect of Gas Temperature

The effect of gas temperature is evaluated by heating a gas in a custom build steel non-resonator. A non-resonator is a device which allows measurements of a gas without optical windows. The main objective is to keep air out of the probe volume. A drawing is displayed in [Figure 5.16](#), the non-resonator consists of a T-junction. A gas bottle is connected to the "side road" of the T-junction, the gas leaves through the "main road". The laser pulses used for the experiment are then passed through the straight section with unobstructed access to the probe volume (the "main road").

The steel non-resonator is heated with a flame mounted on a translation stage. The flame is positioned under the "side road", the pipe connected to the gas bottle. A translation stage moves the position of the flame with respect to the junction to change the temperature. The temperature inside the probe volume is found with CRS thermometry.

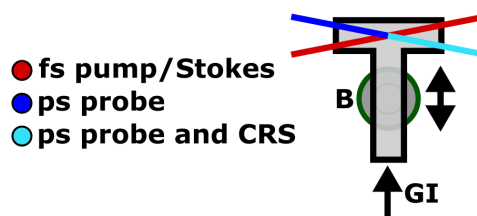


Figure 5.16: Schematic of steel non-resonator to change gas temperature. Bunsen burner is mounted on translation stage to change the gas temperature. Gas temperature inside non-resonator is measured with CRS. B, burner; GI, gas inlet.

The averaged non-resonant CSRS spectrum for room temperature and for $T \approx 660K$ are presented in [Figure 5.17](#). The figure includes a power before ($E_{p/s} = 60\mu J$) and after ($E_{p/s} = 1000\mu J$) the filamentation process has started. The effect of different pump/Stokes pulse energies is larger than the effect of temperature changes.

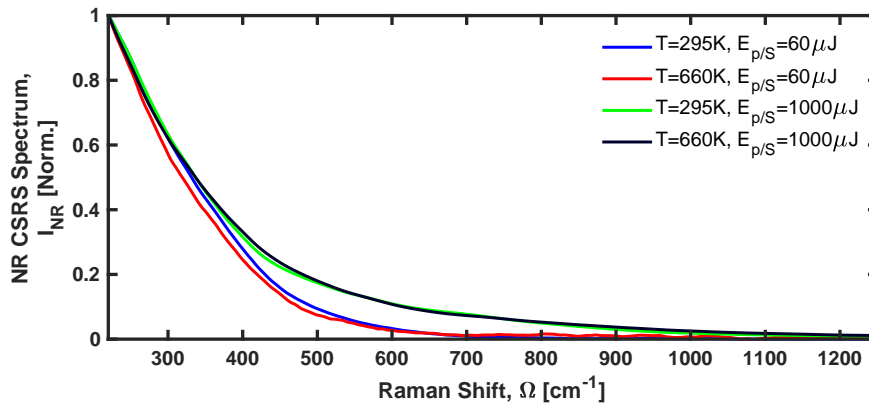


Figure 5.17: Averaged non-resonant single-shot CSRS spectrum measured at different pump/stokes pulse energy for $T = 295$ and 660K (1000 frames).

An estimate for the effective pulse duration is displayed in Figure 5.18. For $E_{p/S} = 30\mu\text{J}$, the increase in temperature results in a slightly longer pulse duration. Possibly, this is due to a smaller amount of group velocity dispersions (GVD) at higher temperatures. A decrease in GVD leads to a change in chirp. For $E_{p/S} = 1000\mu\text{J}$, the effective pulse duration decreases slightly. In the filamentation regime, it is not expected that an increase in temperature would result in a lower effective pulse duration. An increase in temperature results in a lower number density. Therefore, it is expected that the filamentation process becomes less strong. However, at low powers an increase in pulse duration is observed. In Section 5.5.1 it is presented how large the effect of pre-chirping is. The increase in input pulse duration increases the strength of the filamentation process.

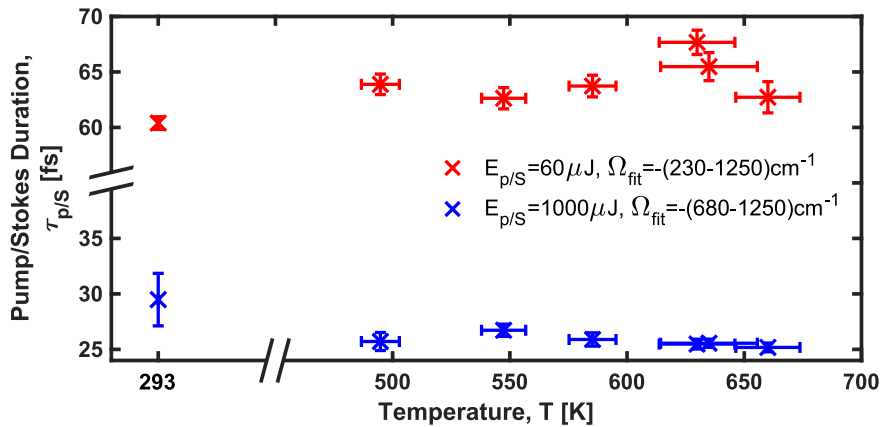


Figure 5.18: Estimate of effective pulse duration for several gas temperatures (1000 frames). Please note that the horizontal and vertical axis have a cut.

It would be interesting to redo the experiment for different positions of the external compressor. This could prove if there are other optima for pre-chirping at high temperatures and whether the external compressor was not optimised for high temperatures.

5.5.5. Effect of Combustion

An indication of the effects of combustion on the non-resonant signal are presented in Figure 5.19. The non-resonant signal is acquired with *in-situ* referencing in a laminar hydrogen/air diffusion flame. *In-situ* referencing of the excitation efficiency is a methodology where the non-resonant and resonant signals are cross-polarized so that they can be separated. The resonant and non-resonant susceptibility of the CRS signal are both measured simultaneously. The methodology is further explained in Section 2.4.1. The temperature in the probe volume is unknown. The purpose of the figure is to indicate the decrease in excitation efficiency due to combustion. The pump/Stokes pulse energy is $E_{p/S} = 1000\mu J$. The estimated effective Gaussian shaped pulse duration for argon and for the hydrogen flame are $\tau_{p/S} = 25.61fs$ ($\sigma_\tau = 0.54fs$) and $\tau_{p/S} = 33.02fs$ ($\sigma_\tau = 0.46fs$), respectively ($\Omega = -(630-1250)cm^{-1}$).

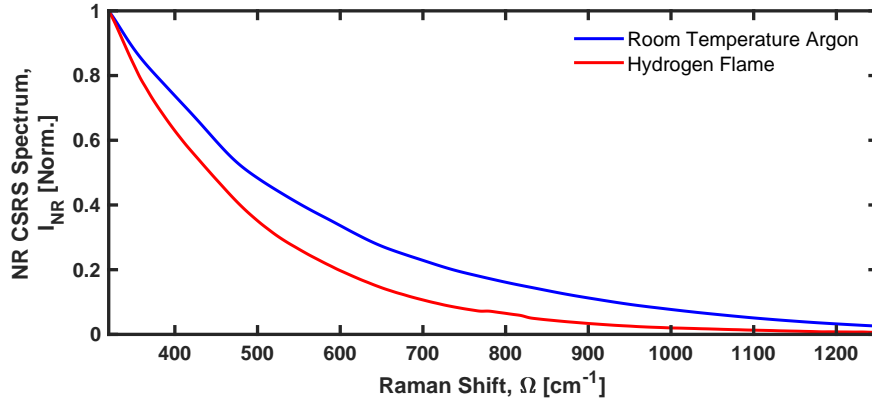


Figure 5.19: Averaged non-resonant single-shot CSRS spectrum measured for a range of pump/Stokes pulse energies inside laminar hydrogen/air diffusion flame (1000 frames).

Although the bandwidth generation is stable, the results suggest that there is a need for *in-situ* referencing of the excitation efficiency. The non-resonant profile is affected by the boundary conditions presented in this section. Therefore, *ex-situ* referencing of the excitation efficiency will most likely result in a constant offset in normalisation.

6

Characterisation of Probe Volume Dimensions

In this chapter the probe volume dimensions under filamentation conditions are determined. A small probe volume is preferred as this enables point measurements. The probe volume is mainly determined by the crossing angle and the beam waist (radius) of the pump/Stokes pulse and probe pulse. The probe volume is located $\sim 4mm$ behind the filament. The main objective of this chapter is to estimate the beam waist of the pump/Stokes pulse under filamentation conditions as no standard procedure exists. The probe volume is described by an ellipsoid with a certain beam waist and a length. In reality, the crossing is more complicated. The probe volume length is called the interaction length, this is defined as the length where both pulses interact along the probe pulse to generate the coherent Raman spectroscopy (CRS) signal.

The standard procedure to measure the probe volume dimensions requires an attenuated probe pulse and pump/Stokes pulse [82]. One part of the procedure requires that a beam profiler is placed in the beam path to measure the beam waist of the probe pulse and pump/Stokes pulse. Where a beam profiler is a diagnostic device to measure the spatial intensity profile of a laser beam. Another part of the procedure requires that a thin sheet of glass is placed in the beam path to measure the interaction length. For both measurements the irradiance at the focus should be much lower compared to the irradiance during normal experiments to prevent damage to the optical equipment placed in the optical path. Under filamentation conditions there is enough irradiance at the focus of the pump/Stokes pulse to blast metal away. Attenuating the pump/Stokes pulse would result in a pulse without filamentation and therefore different characteristics. Therefore, it is not possible to use the standard procedure to estimate the probe volume dimensions under filamentation conditions. In this chapter a novel procedure is presented to estimate this.

The chapter is structured as follows. In [Section 6.1](#) the probe volume dimensions are estimated without filamentation, the conventional method is applied. In [Section 6.2](#) the novel procedure to estimate the probe volume dimensions with filamentation is presented. Lastly, some recommendations for further research are made in [Section 6.3](#).

6.1. Probe Volume Dimensions Without Filamentation

In this section, the probe volume dimensions without filamentation are estimated. Here, the pump/Stokes pulse and probe pulse can be attenuated.

6.1.1. Methodology

The crossing of the pump/Stokes pulse and the probe pulse is illustrated in [Figure 6.1](#). It is assumed that the pump/Stokes and probe beam waist are constant along the probe volume. The beam waist is defined as half the length (radius) between two points with $1/e^2 \approx 0.14$ of the maximum intensity value, where (radius, $1/e^2$) describes the intensity at the pulse boundaries.

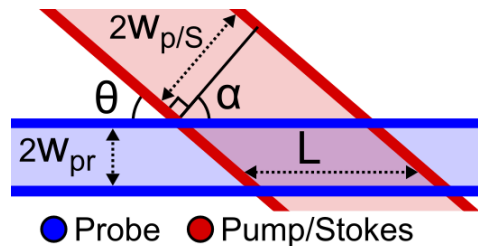


Figure 6.1: Schematic of geometrical crossing of pump/Stokes pulse with probe pulse. Figure is not to scale. For approximation it is assumed that beams do not diverge. w_{pr} , probe beam waist; $w_{p/s}$, pump/Stokes beam waist; θ , crossing angle; α , pump/Stokes pulse angle.

With this assumption the crossing angle (θ) can be determined according to [Equation 6.1](#).

$$\theta = \sin^{-1}\left(\frac{2w_{p/s}}{L}\right) \quad (6.1)$$

As shortly introduced at the beginning of this chapter, two experiments are required for the conventional method. First, the beam waist of the pump/Stokes pulse and probe pulse are measured. The experimental setup is presented in [Figure 6.2](#). The half-wave-plate in the path is rotated to minimise the power in the pulse. Rotating the half-wave plate rotates the linearly polarized light such that the beam can be attenuated by the polarizing beamsplitter which passes only linearly polarized light in a certain direction. Secondly, a wedge plate and neutral density filter are placed behind the last focusing lens. A wedge plate is an optical element with two surfaces which are not parallel. Therewith, the strongly attenuated reflections from both surfaces travel in different directions and therefore are separable. Finally, the beam waist is measured with a beam profiler which is placed in the focus of the pulse.

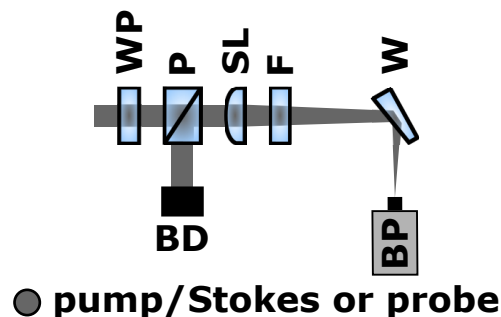


Figure 6.2: Schematic of experimental setup to find beam waist of pump/Stokes pulse and probe pulse. The objective of the experimental setup is to attenuate the pulse to be able to place a beam profiler in the focus of the beam without damaging the beam profiler. WP, half-wave-plate; P, polarizer beamsplitter; SL, spherical lens; F, neutral density filter; W, wedge plate; BD, beam dump; BP, beam profiler.

To determine the interaction length, a thin sheet of glass ($\sim 200\mu\text{m}$) is placed in the crossing of the beams. Inside the glass, the four-wave mixing process is much stronger, as the number density in a condensed medium is much higher compared to the gas phase. Given the quadratic relation between the CRS signal and the third-order susceptibility ($I_{CRS} \propto |\chi^{(3)}|^2$) and the linear relation between the third-order susceptibility and the number density ($\chi^{(3)} \propto N$), the CRS signal scales quadratically with number density ($I_{CRS} \propto N^2$). Placing a thin sheet of glass in the probe volume creates a high CRS signal. The glass is moved on a translation stage along the probe pulse. The length (full-width-at-half-maximum, FWHM) of the integrated signal along the translation stage is the interaction length.

6.1.2. Results

The beam waist of the probe pulse and pump/Stokes pulse are measured to be $w_{pr} = 22\mu\text{m}$ (radius, $1/e^2$) and $w_{p/s} = 38\mu\text{m}$ (radius, $1/e^2$) respectively. The interaction length is measured at $L = 1.4\text{mm}$ (length, FWHM). With Equation 6.1 the crossing angle can be determined. The crossing angle is estimated to be $\theta = 3.2$ deg.

6.2. Probe Volume Dimensions With Filamentation

In this section the probe volume dimensions with filamentation are estimated. The main objective is to estimate the beam waist of the pump/Stokes pulse under filamentation conditions.

6.2.1. Methodology

An experimental setup is designed to relay-image the cross-section of the beam output by the filament, to estimate its divergence. The inverted optical telescope setup is shown in Figure 6.3.

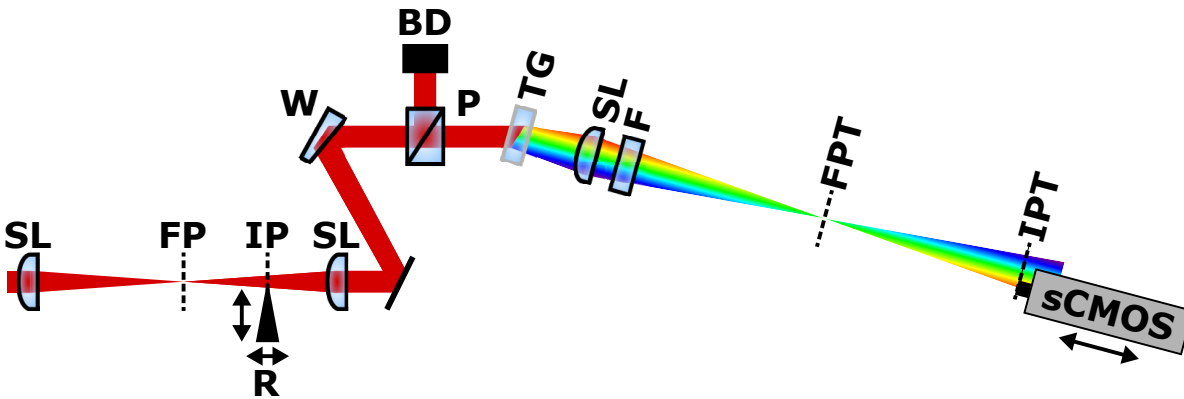


Figure 6.3: Schematic of coherent imaging spectrometer employed to estimate pump/Stokes pulse divergence. Pump/Stokes pulse is collimated by spherical lens ($f = 200\text{mm}$) after it diverges out the filament. To attenuate signal wedge plate, polarizer and neutral density filter are inserted. Then, colours are dispersed by a transmission grating and focussed by a spherical lens ($f = 500\text{mm}$). SL, spherical lens; FP, focal plane; IP, imaging plane; R, razor blade; W, wedge plate; BD, beam dump; P, polarizer; TG, transmission grating; F, neutral density filter; FPT, focal plane after telescope; IPT, imaging plane after telescope.

The pump/Stokes pulse ($E_{p/s} = 1.5\text{mJ}$) is focused by a spherical lens (SL, $f = 500\text{mm}$), in the focal plane a filament is produced. The beam diverges out of the filament and the laser beam is collimated with a spherical lens ($f = 200\text{mm}$). To attenuate the signal, a wedge plate, a polarizer and a neutral density filter are inserted. The angle of the linear polarization is changed by a half-wave plate in the initial part of the experimental setup. The filamentation process does not change the polarization of linearly polarized light. The half-wave plate is turned to minimize the output signal. The initial part of the experimental setup is identical to the experimental setup used for CRS measurement (see Section 3.4).

The collimated light is then passed through a transmission grating. The dispersed colours are focused by a spherical lens ($f = 500mm$). The neutral density filter is placed after the focusing position. Here, the light refocuses, behind the focal plane of the telescope (FPT) the imaging plane of the telescope (IPT) is positioned. The beam is then imaged with a sCMOS camera (Zyla 4.2, Andor).

In between the focal plane and the spherical lens a razor blade on a translation stages is positioned which can cover part of the pulse. The razor blade is used to find the imaging plane with the sCMOS camera. The methodology during the measurement is as follows. Firstly, the razor blade at the IP is moved transversely to cover part of the beam path at a location where the irradiance of the pump/Stokes pulse is low. This location is the furthest point from the filament which is imaged. Part of the beam is blocked. Secondly, the sCMOS camera is moved in longitudinal direction. The position of the camera is found where the edge function in intensity due to the razor blade is best imaged on the camera. The image of the razor blade is only sharp if the IPT is found, outside the IPT the change in intensity is not a sharp change. The razor blade is then removed from the beam path and an image is acquired. Thirdly, for calibration, two images are acquired with the razor blade $1mm$ apart positioned in the path. This is repeated for different imaging planes closer to the filament. The procedure is stopped when the irradiance becomes too high for metal to be placed in the beam path, close to the filament the metal razor blade is blasted.

6.2.2. Results

The dispersed colours from the pump/Stokes pulse with the neutral density filter removed are displayed in Figure 6.4. This is a photo captured with a consumer camera (CMOS, Nikon D7500) on a white surface. This figure is not used in post-processing, it is presented to show the output of the experimental setup. The figure shows donut like patterns. These patterns have been reported on in literature [65, 83, 84]. The underlying mechanism to create this shape is unexplained in literature; this could be due to the interactions of multiple filaments [83]. Furthermore, as the signal is not perfectly continuous in the horizontal direction, it shows that the spectrum is not perfectly continuous. There are discrete colours with more energy.

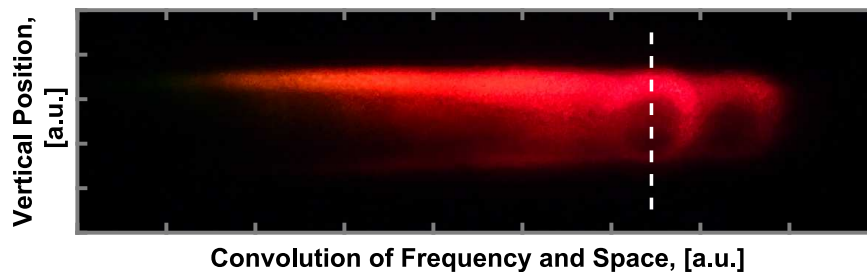


Figure 6.4: Dispersed colours of pump/Stokes pulse cone at location of sCMOS camera captured with CMOS camera. The information on position and wavelength are dispersed in the vertical and horizontal direction respectively. The dashed line shows the location of the actual measurement. Please note that the horizontal axis also contains some spatial information. A convolution of frequency and spatial information is displayed (see for example [85]). The donut like patterns are believed to be one frequency.

During the experiment the transversal position of the CMOS camera is kept constant by placing it in the middle of the displayed donut like shaped ring. This is a relatively bright, dark red colour. It was chosen to use the most dark red colour visible, because that is closest to the central wavelength of $\lambda = 800nm$. Higher wavelengths were not visible due to losses in the experimental setup. In post-processing, the brightest pixel is selected to process the same vertical line in all images.

The intensity profile of a cross section is displayed in Figure 6.5 (along the dashed line in Figure 6.4). The intensity profile shows two peaks. The width at $1/e^2$ is shown for both the main as the smaller peak with a red and blue crosses (x) respectively.

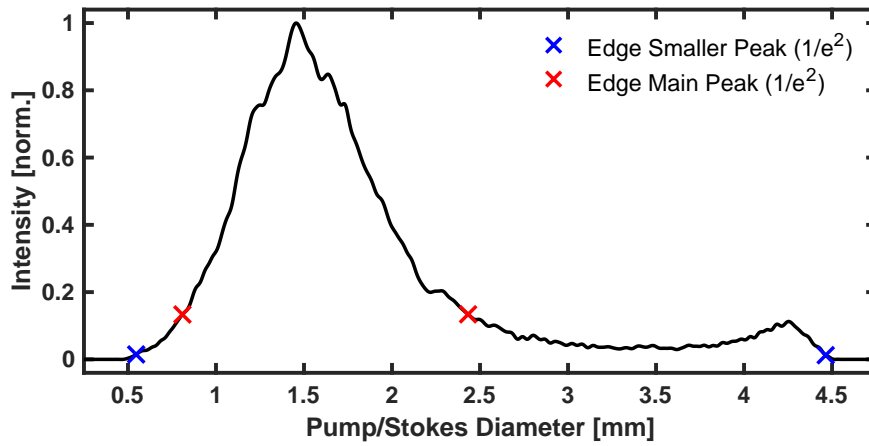


Figure 6.5: Typical cross section of pump/Stokes beam waist intensity ($x = 66.33\text{mm}$ or 7th point). The intensity profile consists of two peaks; a donut-like shape. The $1/e^2$ width is found for both peaks. The main and smaller peak are located at 1.46 and 4.25mm .

The rate of divergence is determined for both the smaller and the main peak. The beam waist along the longitudinal direction of the pump/Stokes pulse is shown in Figure 6.6. The solid black line represents the location of the probe volume, which is approximately $\sim 4\text{mm}$ after the filament. It is not possible to image closer to the probe volume, because that results in blasting of the razor blade. Without the razor blade the images can not be calibrated. In the captured regime the beam waist is a linear function of the longitudinal position. The beam diameter at the probe volume is estimated to be $2W_{p/S} = 0.53$ and 0.63mm for the line with the smaller and the main peak, respectively. It should be noted that most of the energy is in the main peak, therefore, the radius determined with the main peaks represents better the waist of the pump/Stokes pulse at the probe volume ($2W_{p/S} = 0.53\text{mm}$).

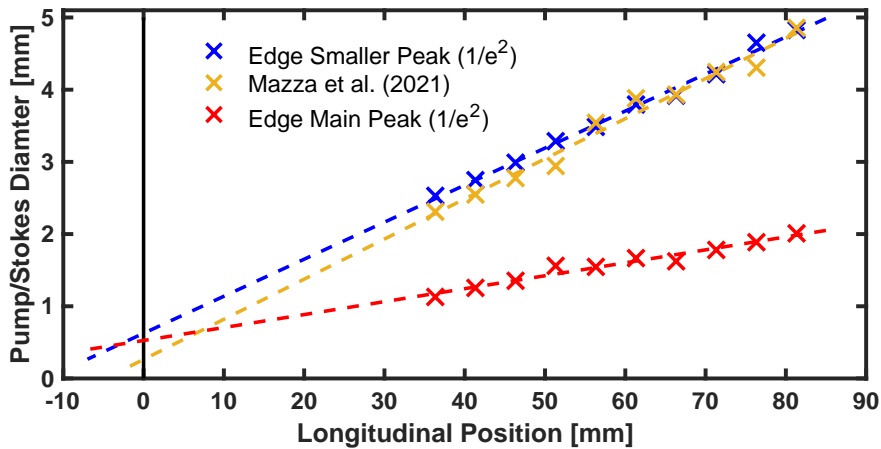


Figure 6.6: Divergence of pump/Stokes pulse measured after filament for $E_{p/S} = 1.5\text{mJ}$. The origin of the longitudinal position is the approximate location of the probe volume. The figure shows data used recently for a publication by our research group (Mazza et al. (2021)) [86].

Furthermore, the Figure 6.6 presents data points used in a recent publication by our research group (Mazza et al. (2021)) [86]. This set of points involves the same experimental data. For Mazza et al. (2021) the edge of the smaller peak is used. The data points presented in this work deviate slightly from those points. In Mazza et al. (2021) the pump/Stokes waist at the probe volume is estimated to be $2W_{p/S} = 0.26\text{mm}$ which is approximately twice as small as estimated here. The difference can be explained by an improved methodology used for the calibration of the images in this work. The images are linearly interpolated to find more precisely the edge function of the images. For Mazza et al. (2021) the images were not linearly interpolated. Hereby, the pump/Stokes diameter becomes more smooth

with longitudinal position. A slight change in calibration can result in a large change in estimated beam waist, because the data needs to be extrapolated over a large distance. It demonstrates the sensitivity of the methodology to the calibration, this is a clear limitation of the methodology.

With Equation 6.1 the interaction length is estimated for different crossing angles in Figure 6.7. In Section 6.1 the crossing angle is determined to be $\theta = 3.2$ deg. This crossing angle gives an interaction length in between $L = 9.6$ and 11.3 mm (length, $1/e^2$). Compared to the interaction length measured outside the filamentation regime ($L = 1.4$ mm, length, FWHM), the estimate for the interaction length with filamentation is long even when the difference between the $1/e^2$ and FWHM length is accounted for. The differently calibrated images used for Mazza et al (2021) results in a interaction length of $L = 4.8$ mm (length, $1/e^2$) for $\theta = 3.2$ deg. This further illustrates that the methodology is very sensitive to the calibration.

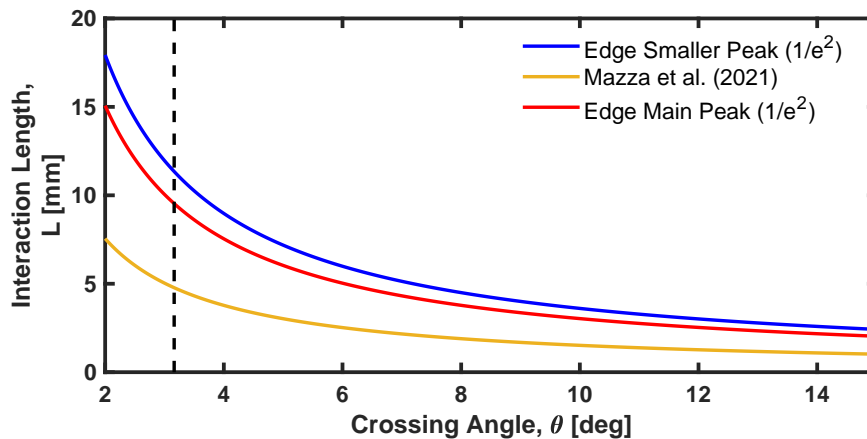


Figure 6.7: Interaction length for different crossing angles in filamentation regime. The dashed vertical line shows a crossing angle of $\theta = 3.2$ deg, as determined in Section 6.1.

The estimated interaction length with filamentation is long. Partly this can be expected, because the pump/Stokes pulse is not in the focus when crossed with the probe pulse. This results in a longer interaction length. However, the estimated interaction length with filamentation is longer than expected. This can be explained by the assumption that the crossing of the pump/Stokes pulse and probe pulse is purely geometric. Meaning that the intensity is not weighted. A more sophisticated method where the intensity is weighted would most likely result in a smaller interaction length. Most likely, this would also affect the estimated crossing angle as the same geometric scheme is used there. Furthermore, in hindsight the location of the filament was relatively far spaced from the probe volume. A large spacing was used to avoid ionization in the probe volume. Ionization of the medium can possibly impact the Boltzmann distribution of the Raman-active molecules, hereby, thermometry would be affected. The effects of the filament on the Boltzmann distribution are further studied in Section 7.2. As the pump/Stokes pulse diverges out of the filament, further spacing between the filament and the probe volumes results in a larger estimate for the pump/Stokes beam waist at the probe volume. This waist is directly linked to the estimated interaction length. A shorter distance would shift the trend displayed in Figure 6.7 downwards.

The estimated interaction length of $L = 9.6$ - 11.3 mm (length, $1/e^2$) can therefore be seen as a maximum length. Especially because, such long interaction lengths would result in problems when the probe volume is positioned near steep temperature gradients like the flame front. During CRS thermometry these problems are not observed. To avoid spatial averaging in experiments, it is advised to avoid too shallow crossing angles.

The probe volume radius is equal to the beam waist of the probe volume, because the beam waist of the probe pulse is smaller than the beam waist of the pump/Stokes pulse. The probe volume radius is $w_{prv} = w_{pr} = 22 \mu\text{m}$ (radius, $1/e^2$). Concluding, the probe volume dimension with filamentation is measured to be $\sim 44 \mu\text{m}$ (width, $1/e^2$) \times $\sim 44 \mu\text{m}$ (height, $1/e^2$) \times ~ 9.5 mm (length, $1/e^2$) for a probe volume positioned ~ 4 mm after the filament.

6.3. Concluding Remarks

All in all, the novel methodology to relay-image the cross-section of the beam output by the filament, to estimate its divergence shows reasonable results. It allows to estimate the pump/Stokes beam waist at the location of the probe volume inside the filamentation regime. It should be noted that a clear limitation of the methodology is sensitivity of the output to the calibration. Some recommendation can be made to improve other aspects presented in this chapter.

During the experiment it was observed that the transmission of long wavelengths was not optimal in the telescope. The chosen optical mirrors were not optimised for light outside the visible light spectrum. It is advised to redo the experiment with optical equipment optimised for $\lambda = 700\text{-}900\text{nm}$.

With optical elements optimised for a larger frequency range, it is advised to measure the divergence of multiple colours. This can further increase the quality of the results. Furthermore, the pump/Stokes pulse can be modelled as a cone per colour with the intensity profile as measured during the experiment. Therewith, a more reasonable interaction length can be found.

7

Characterisation of Ultrabroadband CRS Thermometry

In this chapter the effects of femtosecond ($fs = 10^{-15}s$) laser-induced filamentation on two-beam femtosecond/picosecond ($ps = 10^{-12}s$) coherent Raman Spectroscopy (CRS) thermometry are characterised. The chapter is structured as follows. Firstly, the relation of the resonant and non-resonant coherent anti-Stokes Raman spectroscopy (CARS) signals with the input pump/Stokes pulse energy is investigated in [Section 7.1](#). Secondly, the effect of different filament positions with respect to the probe volume on thermometry is discussed in [Section 7.2](#). Thirdly, for different pump/Stokes pulse energies molecular nitrogen thermometry is performed in [Section 7.3](#). Then, the effects of combustion on thermometry are discussed in [Section 7.4](#). Finally, thermometry with ultrabroadband CARS via *in-situ* fs-laser-induced filamentation is demonstrated behind an optical window in [Section 7.5](#). All experimental results in this chapter are novel, similar figures have not been presented in the literature.

7.1. Relation of Pump/Stokes Energy and CARS Signal

According to theory the CARS signal is a function of the product of the input pulses intensities ($I_{CARS} \propto I_{pump}I_{Stokes}I_{probe}$). In a two-beam CARS setup, the pump and Stokes photon originate from the same pulse. Therefore, there is a quadratic relation between the intensity of the CARS signal and the pump/Stokes pulse ($I_{CARS} \propto I_{p/S}^2$). During CARS experiments it was observed in a recent publication by our research group that the resonant and non-resonant signal did not scale quadratically with pump/Stokes pulse power in some regions [87]. Kliukin et al. (2021) argue that the start of the filamentation process could play a role in the change of scaling. It is speculated that a competing effect associated with the filamentation process could reduce the intensity of the CARS signal.

In this thesis some experimental results are of interest for the discussion. In [Section 5.3](#) the N_2+ fluorescence is imaged. The plasma channel is observed from pulse energies of $E_{p/S} = 40\mu J$ upwards. Furthermore, it is observed that the filamentation process starts around $E_{p/S} \approx 74\mu J$. The region in between the two points is referred to as the pure multi-photon ionization (MPI) regime ($E_{p/S} \approx 40-74\mu J$).

To characterise this effect, a power scaling of the pump/Stokes pulse is performed. The data consists of three power ranges of the pump/Stokes pulse ($E_{p/S} = 10-50, 50-200, \text{ and } 200-1000\mu J$), where each range has a different intensity of the probe pulse. The probe pulse was attenuated in between the different ranges to prevent saturation of the camera. The power of the probe pulse was not measured, as it was thought to be irrelevant. A measurement overlap allows for comparison of the different

ranges. The resonant signal is acquired in molecular nitrogen at room temperature, the non-resonant signal is acquired in argon at room temperature.

The scaling of CARS intensity with pump/Stokes pulse input energy is presented in Figure 7.1. The figure presents the summed intensity of a 1000 single-shot CARS spectra. There is a quadratic scaling of the resonant CARS signal up to $E_{p/S} \approx 300\mu J$, above $E_{p/S} \approx 300\mu J$ a linear trend is observed. The non-resonant CARS signal scales similarly up to $E_{p/S} \approx 200\mu J$. Above $E_{p/S} \approx 200\mu J$ it is not possible to drawn firm conclusions on the trend.

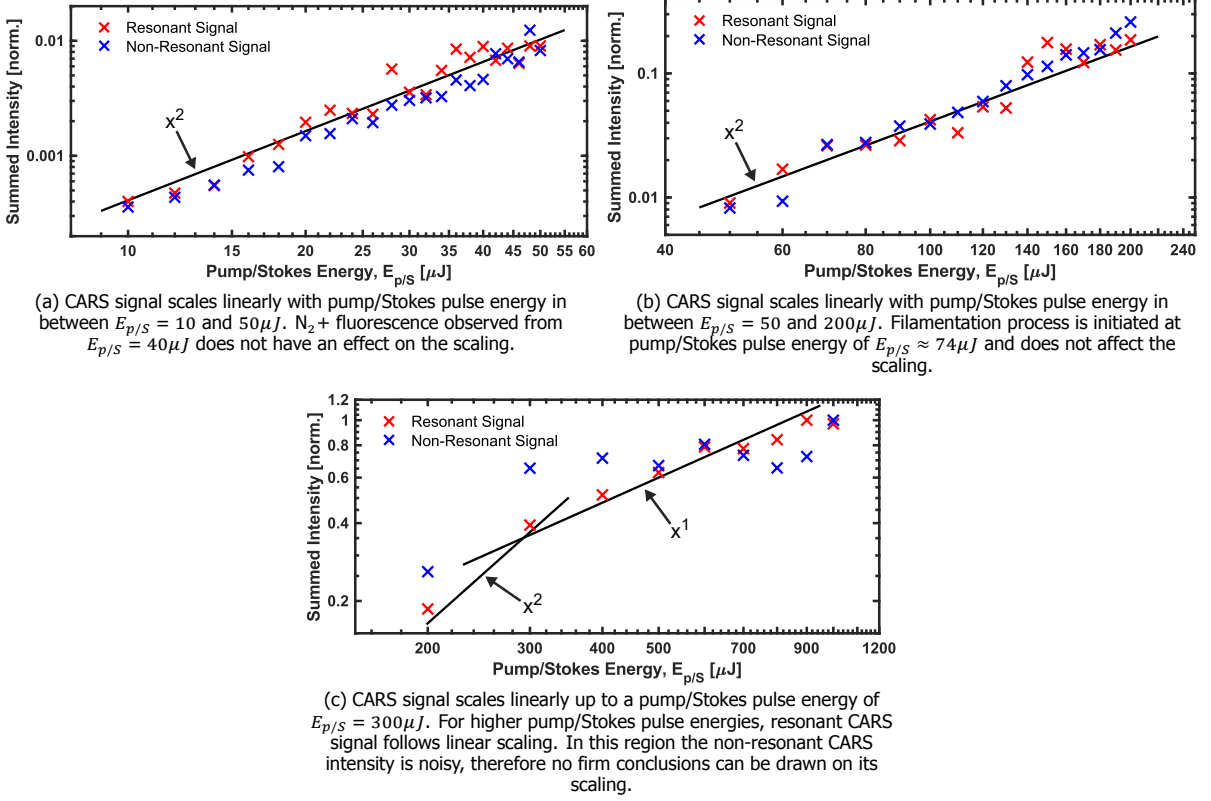


Figure 7.1: Scaling of resonant and non-resonant CARS signal with pump/Stokes pulse energy in a log-log plot. A quadratic trend between $E_{p/S} = 10$ and $300\mu J$ is shown. Above $E_{p/S} = 300\mu J$ a linear trend is shown. The resonant signal is acquired in molecular nitrogen at room temperature, the non-resonant signal is acquired in argon at room temperature.

Kliukin et al. (2021) showed that the resonant CARS signal changes from quadratic to linear scaling at pump/Stokes pulse energies of $E_{p/S} \approx 25-30\mu J$ [87]. The experimental results do not match. The experiment was performed with the same experimental setup. Therefore, it was expected that the results would match. Different boundary conditions are discussed to explain the difference between the two experimental results.

Firstly, it is possible to exclude the gas composition from the discussion. The resonant signal presented here and the experiment results presented by Kliukin et al. (2021) are both obtained in a flow of molecular nitrogen [87]. Furthermore, the experimental data shows no clear difference in scaling between the resonant and non-resonant signal while obtained in a different gas mixtures.

Another possibility would be the effect of different polarization settings. Kliukin et al. (2021) demonstrated the scaling of cascaded CARS (CCARS), the authors opted to orthogonally polarize the CARS and CCARS signal. Such that both signals can be separated with a polarization beamsplitter. The polarization angle between the pump/Stokes pulse and probe pulse polarization is $\phi = 70.5$ deg. For the measurements presented in this work, probe pulse suppression was used. The intensity of the probe pulse is minimised in the channel directed to the camera. This gives the possibility to open the bandpass filter further and measure spectral lines closer to the probe pulse ($\Omega = 0cm^{-1}$) without

damaging the camera. The relative polarization of the pump/Stokes pulse and probe pulse is set to $\phi = 45$ deg. Although both measurements are performed with different polarization settings, it is not likely that this gives rise to different scaling regimes. No theory suggests a change in scaling based on a constant difference in polarization settings.

Then, it can be argued that the scaling is not correlated to the filamentation or ionization processes as Kliukin et al. (2021) suggest. The experimental data shows that the transition point in scaling is at a pump/Stokes pulse energy of $E_{p/s} = 300\mu J$ which is much higher than the onset of the pure MPI regime and the onset of the Kerr-effect. The onset of those processes therefore does not explain the difference.

Possibly, the probe pulse energy affects the scaling, the probe pulse energy is not constant. This points at an effect where the irradiance in the probe volume plays a role. Both the probe pulse and pump/Stokes pulse energy would be effecting the scaling. To test the effect of irradiance in the probe volume, a 2D power scan is required, where both the probe pulse and the pump/Stokes pulse power are varied. As the probe pulse can not be attenuated to prevent saturation of the camera one could place neutral density (ND) filters in front of the camera. The ND filters can be calibrated by measuring the total intensity before and after placing the filters.

From the experiment, the change from quadratic to linear scaling remains unexplained. Future experiments are required to investigate the scaling. To reduce noise in future measurements, it is advised to increase the measurement time. Increasing the acquisition time will decrease the noise. This can reduce the uncertainty in finding the transition point.

7.2. Effect of Filament Location on Thermometry

In this section the effects of filament location on thermometry are studied to investigate whether the filamentation process has an impact on the Boltzmann distribution of the Raman-active molecules in the probe volume. A change in Boltzmann distribution would result in spectral cooling or heating during CRS thermometry. In the experiment the filament is moved with respect to the probe volume. The start position is referred to as the reference position or position = 0mm. It should be noted that the reference position of the filament referred to in this section is not exactly the same as reported on in [Chapter 6](#). The alignment of the beams is optimised before every experiment. Most probably, the filament and probe volume are more closely spaced in this section.

7.2.1. Methodology

The filament is moved with the focusing lens of the pump/Stokes pulse. This lens is placed on a translation stage and moved with 1mm steps. A resonant CARS spectrum is acquired in molecular nitrogen at room temperature. The spectrum is normalised with the non-resonant CARS spectrum acquired in argon at room temperature. The pump/Stokes pulse energy during the experiment is $E_{p/s} = 1000\mu J$.

To find the location of the filament with respect to reference position a similar procedure as explained in [Section 5.2](#) is applied. This procedure involves placing a consumer CMOS camera perpendicular to the filament. Multiple images are acquired of the filament in air. To calibrate the frames, a ruler is placed where the filament is positioned normally. To correlate the position of the filament to the probe volume a razor blade is positioned at the location of the probe volume. The image of the ruler with the razor blade gives the dimensions of the filament, and its position with respect to probe volume.

7.2.2. Results

The synthetic Raman spectra are computed with a time-domain CARS model, similar to models reported on in literature [[11](#), [15](#), [88](#)]. To account for spectral broadening due to the imaging system, the synthetic spectrum is convolved with a Voigt instrument response function. A Voigt profile is a

distribution given by a convolution of a Cauchy-Lorentz distribution and a Gaussian distribution. Here the Voigt lineshape consists of a 0.9cm^{-1} Lorentzian (full-width-at-half-maximum, FWHM) and a 1.2cm^{-1} Gaussian contribution (FWHM).

A typical fit with the filament placed at the reference position is shown in Figure 7.2. The molecular nitrogen at room temperature single-shot CARS spectrum is fitted with a model to retrieve the temperature. At an offset of -0.2 the residual between the model and the spectrum is displayed. In the experimental spectrum, slight increases around the minima of the synthetic spectrum can be observed between the positions of the normal peaks. Most likely, the slight deviations originate from cascaded CARS (CCARS). Two CCARS pathways are possible; in parallel CCARS the CARS photons serve as new probe photons for other molecules, in sequential CCARS the photons participate in the creation of new Raman coherences [87]. For molecular nitrogen the even and odd spectral lines are separated by $\sim 4B$ and the first S-branch spectral line is shifted with $\sim 6B$ from the probe spectral line, where B is the rotational constant of the Raman-active species ($\sim 2\text{cm}^{-1}$ for molecular nitrogen) [87]. Therefore, the spectral lines for CCARS are shifted with $\sim 2B$ [87]. In Figure 7.2 the CCARS signal is visible in between the main CARS spectral lines. The synthetic model does not include this contribution as the effect in the experimental data is deemed only small.

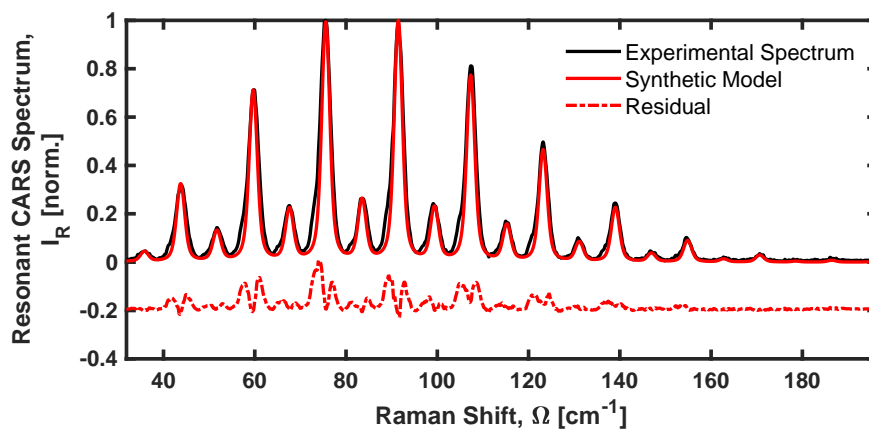


Figure 7.2: Typical fit of single-shot ultrabroadband CARS spectrum via *in-situ* fs-laser-induced filamentation in molecular nitrogen at room temperature where probe volume is at the reference position (position = 0mm) with $E_{p/S} = 1000\mu\text{J}$. Temperature of synthetic model is $T = 298\text{K}$. The spectral fitting can be evaluated by the residual of the synthetic and experimental spectra, the residual is presented in the figure at an offset of -0.2 for clarity purposes.

It should be noted, that the acquired spectrum does not show the need for ultrabroadband CRS. Here, molecular nitrogen thermometry is performed at room temperature. As the gas composition consist of only one molecular species, the spectrum is much less congested than when oxygen would have been present as for example in air.

The evaluated temperatures for different positions of the filament are presented in Figure 7.3. On the left side of the figure the probe pulse is crossed with the pump/Stokes pulse before the filament, here conventional two-beam fs/ps CARS takes place. The pump/Stokes pulse is not yet broadened by the filamentation process and no ionization is present in the probe volume. On the right side the probe pulse is crossed with the pump/Stokes pulse behind the filament, here ultrabroadband two-beam fs/ps CARS takes place. The pump/Stokes pulse is broadened by the filamentation process and no ionization is present in the probe volume. In the middle, the probe pulse is crossed with the pump/Stokes pulse in the filament. Here, the filamentation process is active, in this region the pump/Stokes pulse is broadened. Ionization is present in the probe volume. The length of the filament is estimated to be $\sim 7\text{mm}$ long in air ($E_{p/S} = 1000\mu\text{J}$). This is much shorter than the 12.6mm found in Section 5.2 ($E_{p/S} = 1.5\text{mJ}$). Most likely, the difference is due to the change in pump/Stokes pulse power.

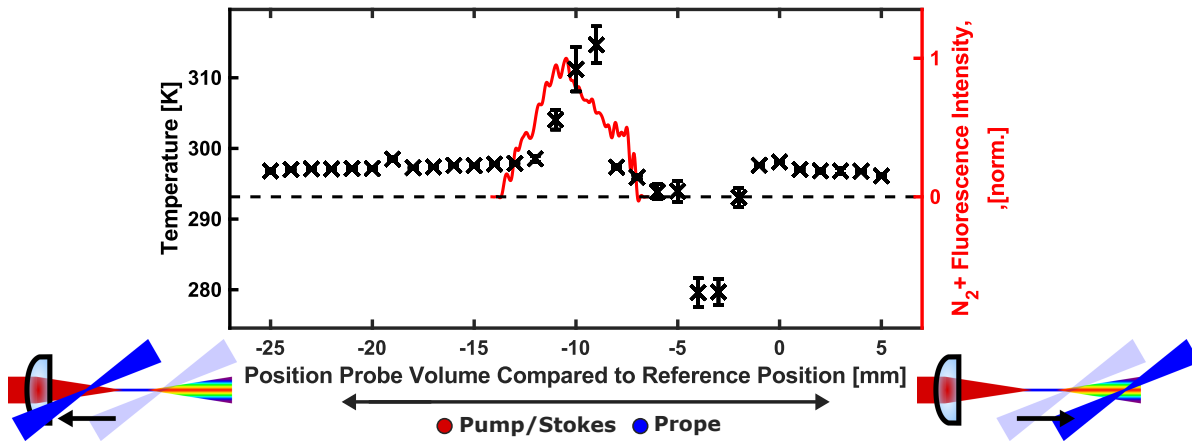


Figure 7.3: Effect of different positions of the filament with respect to the probe volume on CARS thermometry (1000 frames, $E_{p/S} = 1000\mu J$). The red line shows the N_2+ fluorescence from the filament in air at room temperature. For positions left of the N_2+ fluorescence the probe volume is before the filament (conventional two-beam fs/ps CARS). For positions right of the N_2+ fluorescence the probe volume is behind the filament (ultrabroadband two-beam fs/ps CARS). The dashed horizontal line represents room temperature ($T_{room} = 293K$). At the origin the probe volume and filament are spaced as normally employed during thermometry in the experimental setup. Please note that this spacing is set by hand, therefore it deviates from the position discussed in Chapter 6.

The temperature on the left and right side of the figure match. Here, temperatures of around $T \approx 296$ - $298K$, with a standard deviation of $\sigma_T \approx 0.3K$ are measured. In between position -2 and $-11mm$ the temperature deviates from the baseline measured on the left and right. Furthermore, the standard deviation increases in this range to a maximum of $\sigma_T = 3.2K$ at position $= -10mm$.

It can be concluded that ultrabroadband two-beam fs/ps CARS thermometry with supercontinuum generation via fs-laser-induced filamentation (right side of figure) and conventional two-beam fs/ps CARS thermometry result in the same temperature (left side of figure). Furthermore, the results demonstrate that ultrabroadband CARS can be referenced with an averaged non-resonant argon profile, for the boundary conditions given by the experiment. This illustrates that bandwidth generation via fs-laser-induced filamentation is stable.

The supercontinuum generated by fs-laser-induced filamentation is gas composition dependent (see Section 5.5). The bandwidth of the pump/Stokes pulse is therefore different in argon and molecular nitrogen. The excitation efficiency of the resonant and non-resonant CARS signals therefore do not entirely compare. Along the filament, the excitation profile changes differently for the resonant and non-resonant CARS spectra. This means that the normalisation is slightly off. Most probably, the thermometry performed in between position -2 and $-11mm$ is off due to a normalisation error.

Furthermore, in Section 5.2 it is shown that the start and end position of the filament move in time, the standard deviation of the start and end position in room temperature air are $\sigma_{start} = 0.33mm$ and $\sigma_{end} = 0.30mm$ respectively. Therefore, the relative position of the filament to the probe volume is not constant. A different position leads to a different excitation profile as the bandwidth is increased along the filament. The excitation efficiency changes more drastically from shot-to-shot. As observed in the experiment, the standard deviations of the temperature measurements inside the filament are increased.

Inside the filament it is possible that the probability of molecule being in a certain energy state deviates from the Boltzmann distribution. It could be that the system is not in thermal equilibrium. To verify, thermometry should be performed with *in-situ* referencing. Hereby, the effects of gas composition on the normalisation are removed. *In-situ* referencing of the excitation efficiency can determine the excitation from shot-to-shot. If this leads to a temperature which is independent of the position of the filament, it would show that the distribution is unaltered. Furthermore, if the distribution of states is unaffected, it is expected that the standard deviation in the filament would reduce to the standard deviation measured outside the filament.

To conclude, it is not possible to move the filament closer to the probe volume when *ex-situ* referencing of the excitation efficiency is used. This would result in spectral cooling or heating. Most likely, the observed spectral heating and cooling are limitations of the referencing method used during the experiment (*ex-situ*) and are not due to the physics in the filament.

7.3. Effect of Input Energy on Thermometry

The characterisation of the filamentation process in Section 5.5 shows that the input power affects the excitation efficiency. Furthermore, experimental results show that different gas compositions and pump/Stokes pulse powers affect differently the excitation efficiency. In this section the effect of input pump/Stokes pulse power on CARS thermometry is investigated.

A typical fit of molecular nitrogen at room temperature for $E_{p/S} = 200\mu J$ is presented in Figure 7.4. The single-shot CARS spectrum is fitted with a model to retrieve temperature. At an offset of -0.2 the residual between the model and the spectrum is displayed. The Voigt lineshape consists of a $\sim 0.3cm^{-1}$ Lorentzian (FWHM) and a $\sim 2.6cm^{-1}$ Gaussian (FWHM) distribution. There is a large difference in between the Voigt function of this experiment and the experiment presented in Section 7.2 ($\sim 0.9cm^{-1}$ Lorentzian (FWHM) and a $\sim 1.2cm^{-1}$ Gaussian (FWHM)). Most likely, the difference is due to the presence of CCARS in the other experiment.

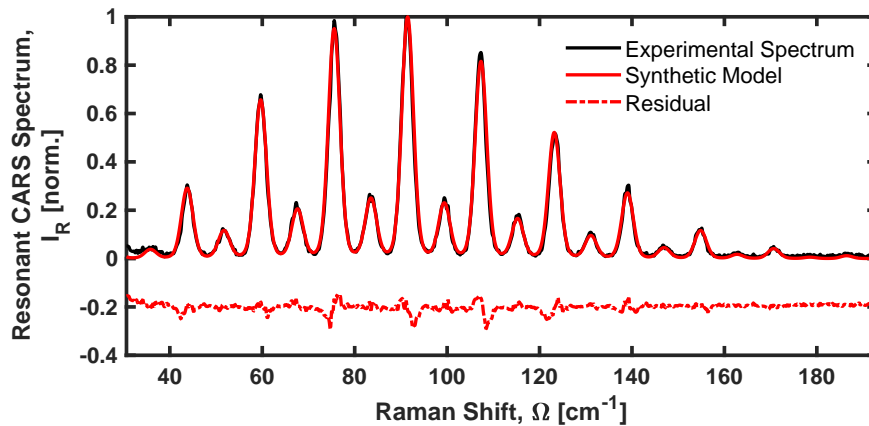


Figure 7.4: Typical fit of single-shot ultrabroadband CARS spectrum via *in-situ* fs-laser-induced filamentation in molecular nitrogen at room temperature with $E_{p/S} = 200\mu J$. Temperature of synthetic model is $T = 316K$. The spectral fitting can be evaluated by the residual of the synthetic and experimental Spectra, the residual is presented in the figure at an offset of -0.2 for clarity Purposes.

The experimental results are presented in Figure 7.5. The figure shows the temperature for molecular nitrogen at room temperature for different pump/Stokes pulse powers. 1000 frames were acquired per measurement point. The actual temperature is approximately $T_{room} \approx 293K$. The measured temperature is not constant with input power. Firstly, the baseline temperature, being the temperature outside pump/Stokes pulse energy of $E_{p/S} < 80$ and $> 300\mu J$, is high. The baseline temperature is approximately $T = 305K$. Secondly, in between $E_{p/S} \Rightarrow 80$ and $\leq 300\mu J$ spectral heating is observed. The temperature increases to a maximum of $T \approx 318K$, an increase of $T \approx 13K$. The standard deviation at $E_{p/S} = 50, 190,$ and $800\mu J$ are $\sigma_T = 0.68, 2.29,$ and $1.23K$ respectively. At higher powers, the standard deviation slightly increases. Furthermore, the standard deviation in the region between $E_{p/S} \Rightarrow 80$ and $\leq 300\mu J$ is elevated. Still, the changes are relatively small, therefore, it is not possible to draw clear conclusions.

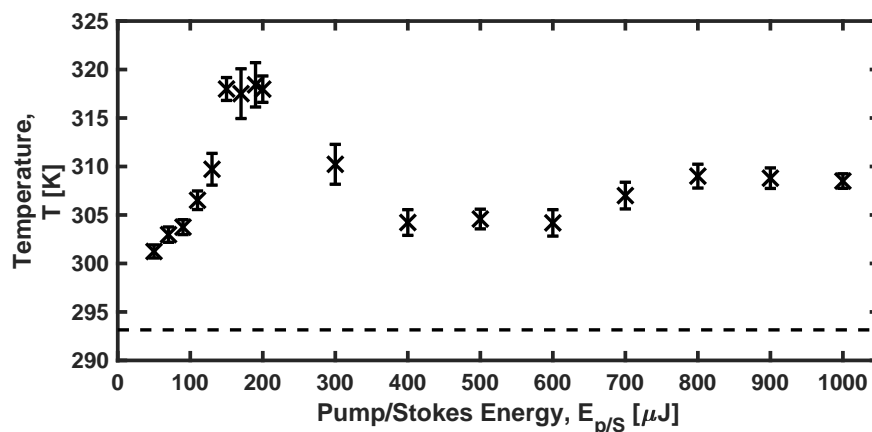


Figure 7.5: Effect of pump/Stokes pulse power on CARS thermometry (1000 frames). The dashed horizontal line represents room temperature ($T_{room} = 293K$).

In Section 5.5.3 it is shown how the non-resonant CARS signal scales with input power due to broadening of the pump/Stokes pulse by fs-laser-induced filamentation for different gas compositions. The non-resonant signal in molecular nitrogen is not discussed. It is suggested that normalisation in a gas with higher number density or third-order susceptibility results in spectral cooling. Normalisation in a gas with a lower number density or third-order susceptibility results in spectral heating. The thermometry presented in this section is measured in molecular nitrogen ($44.98\text{mol}/\text{m}^3$, $\chi_{NR}^{(3)} = 7.90 \cdot 10^{-18}\text{cm}^3/\text{erg amagat}$) and normalised with a non-resonant CARS spectrum acquired in argon ($44.56\text{mol}/\text{m}^3$, $\chi_{NR}^{(3)} = 9.46 \cdot 10^{-18}\text{cm}^3/\text{erg amagat}$). Thus, the experiment is carried out with normalisation in a gas composition with lower number density and higher non-resonant third-order susceptibility. The spectral heating suggests that the number density is more important than the non-resonant third-order susceptibility.

Furthermore, in the experiment where the effect of gas composition on non-resonant signal is researched, it is concluded that most of the pulse compression occurs in the range $E_{p/S} = 60\text{-}200\mu\text{J}$ (see Section 5.5.3). The increase in excitation efficiency is dependent on the gas composition. Therefore, it is likely that the normalisation is further off in this region. The increase in temperature in between $E_{p/S} \geq 80$ and $\leq 300\mu\text{J}$ is due to a difference in excitation efficiency.

In Section 7.2 a baseline temperature of approximately $T = 297K$ is found. There is a $T = 8K$ difference between both experiments. Part can possibly be explained by the cascaded CARS observed in Section 7.2, this could have resulted in slight spectral cooling. However, a difference of $T = 8K$ seems too large to be explained by this effect, the reason for this difference is unknown.

To further study the physical reason for the higher baseline new experiments are required. It is advised to re-acquire experimental data in molecular nitrogen with both *in-situ* as *ex-situ* referencing. A comparison of both referencing methods can indicate the effect of inaccuracies due to the normalisation. If no spectral heating would be observed for *in-situ* referencing, it would indicate that the normalisation with *ex-situ* referencing is not correct.

7.4. Effect of Combustion on Thermometry

In this section the effects of combustion on thermometry are discussed. Combustion adds extra uncertainties to the boundary conditions. Both gas compositions and gas temperature are affected by a flame. The pump/Stokes pulse energy is varied in a laminar methane/air premixed flame provided on a Bunsen burner. Thermometry is performed for equivalence ratios of $\phi = 0.9, 1.0, 1.1, \text{ and } 1.2$.

A typical fit is presented in Figure 7.6. Here the fit is displayed for a pump/Stokes pulse power of $E_{p/S} = 100\mu\text{J}$ at an equivalence ratio of $\phi = 1.0$. The residual between the experimental and synthetic

spectrum are displayed at an offset of -0.2 . The Voigt lineshape consists of a $\sim 0.3\text{cm}^{-1}$ Lorentzian (FWHM) and a $\sim 1.5\text{cm}^{-1}$ Gaussian contribution (FWHM).

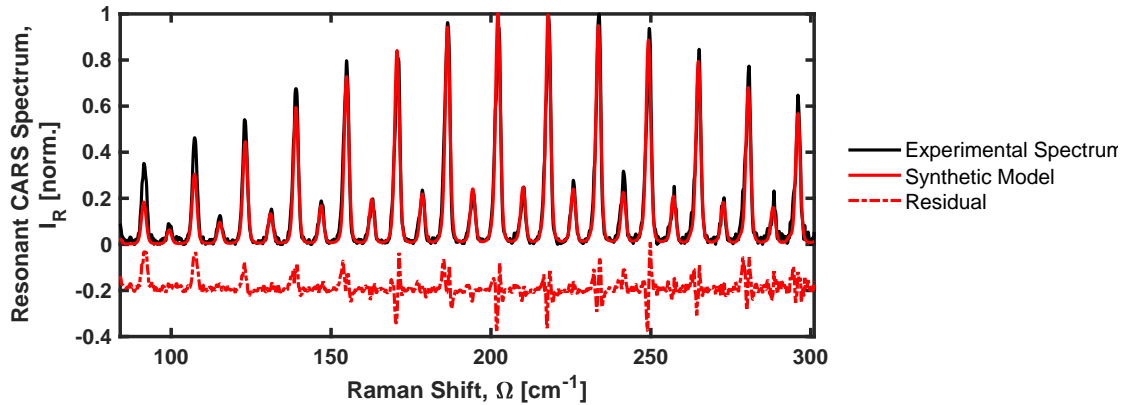


Figure 7.6: Typical fit of single-shot ultrabroadband CARS spectrum via *in-situ* fs-Laser-induced filamentation in laminar premixed methane/air flame ($\phi = 1.0$) with $E_{p/S} = 100\mu\text{J}$. Temperature of synthetic model is $T = 1985\text{K}$. The spectral fitting can be evaluated by the residual of the synthetic and experimental spectra, the residual is presented in the figure at an offset of -0.2 for clarity purposes.

The temperature for different pump/Stokes pulse energies and equivalence ratios are displayed in Figure 7.7. 1000 frames were acquired per measurement point. The horizontal dashed line shows the methane/air adiabatic flame temperature of $T_{Ad} = 2236\text{K}$ [89]. Spectral heating is observed for increasing pump/Stokes pulse powers for $\phi = 0.9, 1.1,$ and 1.2 . For an equivalence ratio of $\phi = 1.0$ and pump/Stokes pulse powers in between $E_{p/S} = 70$ to $100\mu\text{J}$ spectral cooling is observed. At higher powers, spectral heating is observed. At powers lower than $E_{p/S} < 100\mu\text{J}$, the standard deviation is large, the maximum standard deviation in this range is $\sigma_T = 181\text{K}$. For these powers the signal to noise ratio is low. At powers equal or above $E_{p/S} \Rightarrow 100\mu\text{J}$, the standard deviation is in between $\sigma_T = 13$ and 28K .

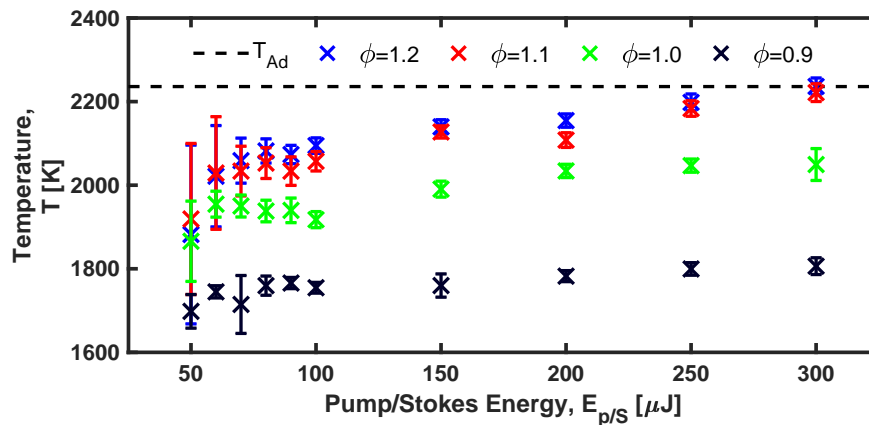


Figure 7.7: Effect of pump/Stokes pulse energy on flame thermometry in laminar premixed methane/air flame. Adiabatic flame temperature of methane with air as oxidizer is $T_{Ad} = 2236\text{K}$ [89].

The data is relatively noisy, resulting in a non-smooth trend with power. The temperature measurements in flames add uncertainties due to variations in the combustion process. The temperature in the probe volume is not constant. Therefore, it is difficult to raise firm conclusions based on this experiment. However, it can be noticed that the same behaviour of spectral heating in between pump/Stokes pulse energies of $E_{p/S} \Rightarrow 80$ and $\leq 300\mu\text{J}$ is observed in Section 7.3. In Section 7.3 thermometry is performed in molecular nitrogen at room temperature. There it is assumed that the normalisation of the resonant signal is off due to different developments velocities

of the filamentation process in different gas compositions. Here, it is likely that the effect is stronger as the gas temperature is also different.

7.5. Ultrabroadband Coherent Raman Spectroscopy Behind Optical Window

To demonstrate the power of two-beam fs/ps CRS with *in-situ* fs-laser-induced filamentation, single-shot flame thermometry is performed behind an optical window. No literature is available which demonstrates ultrabroadband two-beam fs/ps CARS behind optical windows. *In-situ* generation allows for flexible compensation of dispersions terms due to an optical window with one external compressor. The supercontinuum is directly used after it is created.

The optical window ($\sim 22\text{mm}$ thick BK7 Glass) is placed behind the pump/Stokes pulse focusing lens. The implementation of the optical window in the experimental setup is displayed in Figure 7.8. On the left, a schematic is presented. On the right, a picture is presented where the pump/Stokes pulse is represented by a red arrow. Here, the pump/Stokes pulse moves from right to left, it passes through a spherical lens ($f_{p/S} = 500\text{mm}$) and then through the optical window. The pump/Stokes pulse is aligned with the probe pulse with two mirrors where one of the two is behind the optical window. The probe pulse is focussed with a spherical lens ($f_{pr} = 300\text{mm}$)

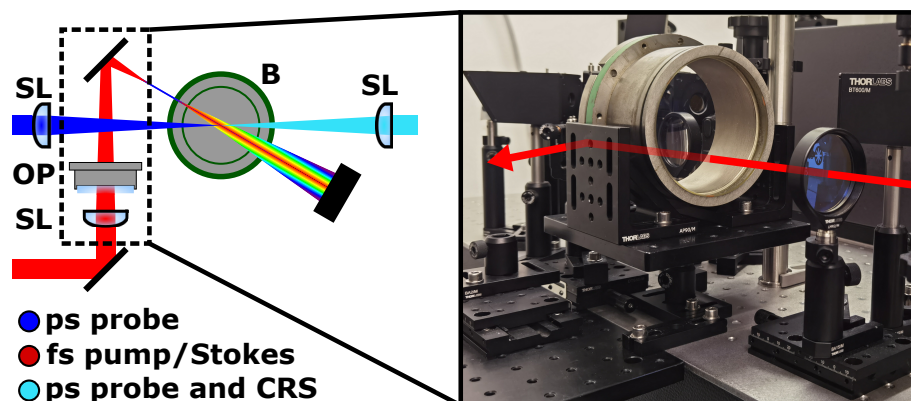


Figure 7.8: Schematic of implementation of optical window in experimental setup. On the right picture shows focussing lens and optical port. Pump/Stokes pulse is displayed with red line which moves from right to left. Pump/Stokes pulse travels through focussing lens ($f = 500\text{mm}$) and then through optical window (BK7, $\sim 22\text{mm}$). The pump/Stokes pulse is aligned with the probe pulse by two mirrors. B, burner; OP, optical port; SL, spherical lens.

For the experiment the probe volume is positioned in the hot product gasses of a fuel-lean laminar premixed methane/air flame. The experimental single-shot spectrum with *in-situ* referencing of the excitation efficiency is displayed in Figure 7.9. In this spectral region, measurements are not possible with two-beam fs/ps CRS without ultrabroadband excitation. Simultaneous ro-vibrational spectroscopy on oxygen and carbon dioxide is performed, the oxygen and carbon dioxide resonances are fitted with two models separately.

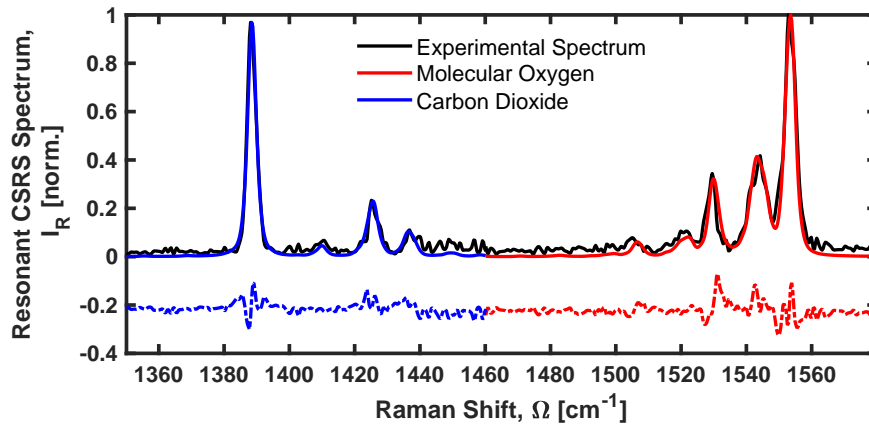


Figure 7.9: Typical fit of single-shot ultrabroadband CSRS spectrum via *in-situ* fs-laser-induced filamentation measured in fuel-lean laminar premixed methane/air flame behind an optical window. Spectrum is fitted with oxygen and carbon dioxide. Synthetic spectrum shows oxygen and carbon dioxide temperatures of $T_{O_2} = 1449K$ and $T_{CO_2} = 1451K$. The spectral fitting can be evaluated by the residual of the synthetic and experimental spectra, the residual is presented in the figure at an offset of -0.2 for clarity purposes.

The mean temperature (μ_T), the standard deviation (σ_T) and the relative standard deviation (σ_T/μ_T) are presented in Table 7.1. The fitted mean temperatures for the molecular oxygen and carbon dioxide resonances are in good agreement.

Table 7.1: Measured single-shot precision of ultrabroadband CSRS via *in-situ* fs-laser-induced filamentation in fuel-lean laminar premixed methane/air flame behind an optical window ($n = 1000$).

	μ_T [K]	σ_T [K]	σ_T/μ_T [%]
Molecular Oxygen	1371	99	7.20
Carbon Dioxide	1375	73	5.29

All in all, the experiment demonstrates successfully for the first time a robust implementation of ultrabroadband CRS behind an optical window. The excitation efficiency is preserved while the pump/Stokes pulse was passed through a thick optical window. No difference in excitation is noted. The extra dispersion terms could easily be accounted for by the external compressor. The methodology allows for measurements in practical applications.

8

Conclusion and Outlook

The aim of this thesis is to contribute to the development of ultrabroadband two-beam femtosecond/picosecond ($f_s = 10^{-15}s$, $p_s = 10^{-12}s$) coherent Raman spectroscopy (CRS) with *in-situ* fs-laser-induced filamentation by characterising fs-laser-induced filamentation and the effects of fs-laser-induced filamentation on thermometry. The work includes an experimental campaign split into three phases: the characterisation of fs-laser-induced filamentation, the characterisation of the probe volume dimensions under filamentation conditions, and the characterisation of ultrabroadband CRS thermometry. In this chapter the main findings of the experimental campaign are highlighted and some suggestion are made for further research.

In [Chapter 5](#) the critical power to initiate the filamentation process in air at room temperature is measured to be $P_{cr} = 1.2GW$ ($E_{p/s} = 74\mu J$). At powers below the critical power a pure multi-photon ionization regime (MPI) is observed ($E_{p/s} = 40-74\mu J$). Opposed to the general explanation of the filamentation process, it shows that there is no direct correlation between the onset of the Kerr-effect and MPI. Furthermore, unlike found in literature the flame has no effect on the critical power. This is further supported by the fact that no clear difference in the dimensions of the filament is measured when placed in a methane/air premixed flame or when placed in air at room temperature ($L \approx 13mm$ (length, $1/e^2$), $\sigma_{Length} = 0.3-0.7mm$ for $E_{p/s} = 1.5mJ$). Therefore, power is an inadequate demarcation line for the onset of the filamentation process and the start of pulse compression.

The pulse duration is estimated based on the non-resonant CRS signal to characterise the supercontinuum. Without filamentation reliable pulse duration measurement are demonstrated with the CRS system. With filamentation, asymmetry in the newly generated frequencies prevents reliable pulse duration measurements. The gas temperature and input power have major effects on the excitation efficiency, the effects of gas compositions are smaller. The excitation efficiency is stable from shot-to-shot. Surprisingly, a positively or negatively chirped input pulse of approximately $\tau_{p/s} \approx 60fs$ is most optimal for pulse compression via fs-laser-induced filamentation in air at room temperature. A transform-limited input pulse ($\tau = 35fs$) results in longer output pulse duration. Most likely, this is because the longer pulses increase the contribution of the delayed nuclear response.

In [Chapter 6](#) a novel procedure is designed to measure the dimensions of the probe volume under filamentation conditions. The cross-section of the pump/Stokes pulse out of the filament is relay-imaged to estimate its divergence. Hereby, the beam waist of the pump/Stokes pulse can be estimated, this part of the methodology gives reasonable results, although it is sensitive to the calibration. For a crossing angle of $\theta = 3.2deg$ the interaction length is estimated to be $L = 9.6-11.3mm$ (length, $1/e^2$). The estimated interaction length is long. Partly, this is due to the purely geometrical scheme used to estimate the crossing angle and interaction length. The intensity is not weighted. For further research it is advised to weight the intensity in the probe volume. Furthermore, the filament and probe volume were relatively far spaced. Still, the novel procedure is promising under harsh environments.

In Chapter 7 the quadratic to linear scaling of the pump/Stokes pulse energy versus the coherent anti-Stokes Raman spectroscopy (CARS) signal intensity is measured to be $E_{p/s} \approx 300\mu J$ which is much higher than reported on in literature. Possibly, the probe pulse power plays a role. Next, ultrabroadband two-beam fs/ps CARS is validated with conventional two-beam fs/ps CARS for molecular nitrogen at room temperature with *ex-situ* referencing of the excitation efficiency ($E_{p/s} = 1000\mu J$). The experimental results show that an averaged spectrum can be used for thermometry. However, flame and room temperature thermometry undergo spectral heating for pump/Stokes pulse powers of $E_{p/s} = 80-300\mu J$. Furthermore, when the probe volume is placed in the filament spectral heating and cooling are observed. Likely, the offset in temperatures originates from a normalisation error. As the boundary conditions can influence the excitation efficiency *ex-situ* referencing does not suffice. It is advised to use *in-situ* referencing of the excitation efficiency to be able to measure confidently the temperature under all boundary conditions. New experiments with *in-situ* referencing are required to prove these speculations.

Ultrabroadband two-beam fs/ps CRS with *in-situ* fs-laser-induced filamentation is demonstrated successfully with the first measurement of ultrabroadband CARS behind an optical window. The single-shot measurements are performed in the hot product gasses of a fuel-lean laminar premixed methane/air flame. The extra dispersion terms due the optical window were easily accounted for by pre-chirping with the external compressor. The excitation efficiency was not affected by the optical window. This demonstrates the robustness and power of supercontinuum generation via *in-situ* fs-laser-induced filamentation for ultrabroadband fs/ps CRS.

Besides the recommendation made to improve the experimental work, it is advised to study the effects of the pump/Stokes pulse numerical aperture for further research. In this work, the focusing speed is kept constant. Slower focusing speeds will most likely results in an improved excitation efficiency. For some applications, like large industrial furnaces, slower focusing is required.

All in all, the experimental work presents novel methodologies and results. The results demonstrate the potential power of supercontinuum generation via *in-situ* fs-laser-induced filamentation for ultrabroadband fs/ps CRS. Nonetheless, improved experiments are required to finalise the characterisation before the technique can be applied with full confidence. Ultrabroadband CRS via fs-laser-induced filamentation is a promising laser diagnostic tool to characterise fundamental combustion effects and novel engine designs to optimise combustion processes. The large stable excitation efficiency allows for measurements at higher Raman shifts behind optical windows where the Raman spectrum is less congested.

Bibliography

- [1] Ypserle, R. K. *et al.*, *Journal of Crystal Growth* (IPCC, Geneva, Switzerland, 2014).
- [2] *Adoption of the Paris Agreement*, in *Report of the Conference of the Parties on its twenty-first session, held in Paris from 30 November to 13 December 2015* (2016).
- [3] Haworth, D. C., *Progress in probability density function methods for turbulent reacting flows*, *Progress in Energy and Combustion Science* **36**, 168 (2010).
- [4] *WORLD ENERGY BALANCES - 2020 Edition*, Tech. Rep. January (2020).
- [5] Lee, D. S. *et al.*, *The contribution of global aviation to anthropogenic climate forcing for 2000 to 2018*, *Atmospheric Environment* **244**, 117834 (2021).
- [6] Xing, F. *et al.*, *The Brief Introduction of Different Laser Diagnostics Methods Used in Aeroengine Combustion Research*, (2016).
- [7] Buldyreva, J., Lavrentieva, N. & Starikov, V., *Collisional Line Broadening and Shifting of Atmospheric Gases* (IMPERIAL COLLEGE PRESS, 2010).
- [8] Bohlin, A., *Development and application of pure rotational CARS for reactive flows*, *Ph.D. thesis*, Lund University (2012).
- [9] Barros, J. *et al.*, *5 kHz single shot hybrid fs/ps-CARS thermometry in an atmospheric flame*, *Optics Express* **28**, 34656 (2020).
- [10] Castellanos, L. *et al.*, *Pure-rotational 1D-CARS spatiotemporal thermometry with a single regenerative amplifier system*, *Optics Letters* **45**, 4662 (2020).
- [11] Mazza, F. *et al.*, *Coherent Raman imaging thermometry with in-situ referencing of the impulsive excitation efficiency*, *Proceedings of the Combustion Institute* **38**, 1895 (2020).
- [12] Kearney, S. P., Scoglietti, D. J. & Kliewer, C. J., *Hybrid femtosecond/picosecond rotational coherent anti-Stokes Raman scattering temperature and concentration measurements using two different picosecond-duration probes*, *Optics Express* **21**, 12327 (2013).
- [13] Escofet-Martin, D. *et al.*, *Dual-probe 1D hybrid fs/ps rotational CARS for simultaneous single-shot temperature, pressure, and O₂/N₂ measurements*, *Optics Letters* **45**, 4758 (2020).
- [14] Bohlin, A., Patterson, B. D. & Kliewer, C. J., *Communication: Simplified two-beam rotational CARS signal generation demonstrated in 1D*, *The Journal of Chemical Physics* **138**, 081102 (2013).
- [15] Kearney, S. P., *Hybrid fs/ps rotational CARS temperature and oxygen measurements in the product gases of canonical flat flames*, *Combustion and Flame* **162**, 1748 (2014).
- [16] Bohlin, A. & Kliewer, C. J., *Direct coherent Raman temperature imaging and wideband chemical detection in a hydrocarbon flat flame*, *Journal of Physical Chemistry Letters* **6**, 643 (2015).
- [17] Richardson, D. R. *et al.*, *Comparison of chirped-probe-pulse and hybrid femtosecond/picosecond coherent anti-Stokes Raman scattering for combustion thermometry*, *Applied Optics* **56**, E37 (2017).
- [18] Lang, T. & Motzkus, M., *Single-shot femtosecond coherent anti-Stokes Raman-scattering thermometry*, *Journal of the Optical Society of America B* **19**, 340 (2002).

- [19] Lucht, R. P. *et al.*, *Femtosecond coherent anti-Stokes Raman scattering measurement of gas temperatures from frequency-spread dephasing of the Raman coherence*, *Applied Physics Letters* **89**, 1 (2006).
- [20] Bohlin, A. *et al.*, *Multiparameter spatio-thermochemical probing of flame-wall interactions advanced with coherent Raman imaging*, *Proceedings of the Combustion Institute* **36**, 4557 (2017).
- [21] Richardson, D. R., Kearney, S. P. & Guildenbecher, D. R., *Post-detonation fireball thermometry via femtosecond-picosecond coherent anti-Stokes Raman Scattering (CARS)*, *Proceedings of the Combustion Institute* **38**, 1657 (2021).
- [22] Prince, B. D. *et al.*, *Development of simultaneous frequency- and time-resolved coherent anti-Stokes Raman scattering for ultrafast detection of molecular Raman spectra*, *The Journal of Chemical Physics* **125**, 044502 (2006).
- [23] Calegari, F. *et al.*, *Molecular rovibrational dynamics excited in optical filamentation*, *Optics Letters* **33**, 2922 (2008).
- [24] Odhner, J. H., Romanov, D. A. & Levis, R. J., *Rovibrational wave-packet dispersion during femtosecond laser filamentation in air*, *Physical Review Letters* **103**, 1 (2009).
- [25] Odhner, J. H., McCole, E. T. & Levis, R. J., *Filament-Driven Impulsive Raman Spectroscopy*, *The Journal of Physical Chemistry A* **115**, 13407 (2011).
- [26] McCole Dlugosz, E. T. *et al.*, *Filament-Assisted Impulsive Raman Spectroscopy of Ozone and Nitrogen Oxides*, *Journal of Physical Chemistry A* **119**, 9272 (2015).
- [27] Calegari, F. *et al.*, *Filamentation-assisted time-resolved Raman spectroscopy in molecular gases*, *Journal of Modern Optics* **57**, 967 (2010).
- [28] Odhner, J. H., Romanov, D. A. & Levis, R. J., *Self-Shortening Dynamics Measured along a Femtosecond Laser Filament in Air*, *Physical Review Letters* **105**, 125001 (2010).
- [29] Phillips, A. C., *Introduction to Quantum Mechanics* (John Wiley & Sons, Incorporated, Chicester, UNITED KINGDOM, 2003).
- [30] (U.S.), N. R. C., *A glossary of terms in nuclear science and technology*, (1957).
- [31] Hosseinnia, A., *On the Use of Rotational CARS on Polyatomics and in Time Domain*, Ph.D. thesis, Lund University (2020).
- [32] Potma, E. O. & Mukamel, S., *Theory of Coherent Raman Scattering*, in *Coherent Raman Scattering Microscopy* (CRC Press, 2016) pp. 24–63.
- [33] Boyd, R. W., *Nonlinear Optics*, third edit ed., edited by Boyd, R. W. (Academic Press, Burlington, 2008) p. 634.
- [34] Placzek, G., *Rayleigh-Streuung und Raman-Effekt* (Akademische Verlagsgesellschaft, Leipzig, 1934).
- [35] Svelto, O. *et al.*, *Lasers and Coherent Light Sources*, in *Springer Handbook of Lasers and Optics* (Springer New York, New York, NY, 2007) pp. 583–936.
- [36] El-Diasty, F., *Coherent anti-Stokes Raman scattering: Spectroscopy and microscopy*, *Vibrational Spectroscopy* **55**, 1 (2011).
- [37] Kataoka, H., Maeda, S. & Hirose, C., *Effects of Laser Linewidth on the Coherent Anti-Stokes Raman Spectroscopy Spectral Profile*, *Applied Spectroscopy* **36**, 565 (1982).
- [38] Michelson, A. A., *On the Broadening of Spectral Lines*, *The Astrophysical Journal* **2**, 251 (1895).
- [39] Dicke, R. H., *The effect of collisions upon the doppler width of spectral lines*, *Physical Review* **89**, 472 (1953).

- [40] Peach, G., *Theory of the pressure broadening and shift of spectral lines*, *Advances in Physics* **30**, 367 (1981).
- [41] Vestin, F., Afzelius, M. & Bengtsson, P.-E. E., *Development of rotational CARS for combustion diagnostics using a polarization approach*, *Proceedings of the Combustion Institute* **31**, 833 (2007).
- [42] Bohlin, A., Bengtsson, P. E. & Marrocco, M., *On the sensitivity of rotational CARS N₂ thermometry to the Herman-Wallis factor*, *Journal of Raman Spectroscopy* **42**, 1843 (2011).
- [43] Marrocco, M., *Herman-Wallis factor to improve thermometric accuracy of vibrational coherent anti-Stokes Raman spectra of H₂*, *Proceedings of the Combustion Institute* **32 I**, 863 (2009).
- [44] Placzek, G. & Teller, E., *Die Rotationsstruktur der Ramanbanden mehratomiger Moleküle*, *Zeitschrift für Physik* **81**, 839 (1933).
- [45] Lukasik, J. & Ducuing, J., *Anharmonic coherent raman scattering in H₂*, *Physical Review Letters* **28**, 1155 (1972).
- [46] Régnier, P. R. & Taran, J. P., *On the possibility of measuring gas concentrations by stimulated anti-Stokes scattering*, *Applied Physics Letters* **23**, 240 (1973).
- [47] REGNIER, P. R., MOYA, F. & TARAN, J. P. E., *Gas Concentration Measurement by Coherent Raman Anti-Stokes Scattering*, *AIAA Journal* **12**, 826 (1974).
- [48] Moya, F., Druet, S. & Taran, J., *Gas spectroscopy and temperature measurement by coherent Raman anti-stokes scattering*, *Optics Communications* **13**, 169 (1975).
- [49] Miller, J. D., *Hybrid femtosecond/picosecond coherent anti-Stokes Raman scattering for gas-phase temperature measurements*, *Ph.D. thesis*, Iowa State University, Digital Repository, Ames (2012).
- [50] Gaydon, A. G., *The Spectroscopy of Flames* (Springer Netherlands, Dordrecht, 1974).
- [51] Afzelius, M. et al., *Dual-broadband rotational CARS modelling of nitrogen at pressures up to 9 MPa. II. Rotational Raman line widths*, *Applied Physics B: Lasers and Optics* **75**, 771 (2002).
- [52] Zheltikov, A. M., *Coherent anti-Stokes Raman scattering: from proof-of-the-principle experiments to femtosecond CARS and higher order wave-mixing generalizations*, *Journal of Raman Spectroscopy* **31**, 653 (2000).
- [53] Kamga, F. M. & Sceats, M. G., *Pulse-sequenced coherent anti-Stokes Raman scattering spectroscopy: a method for suppression of the nonresonant background*, *Optics Letters* **5**, 126 (1980).
- [54] Owschimikow, N., Schmidt, B. & Schwentner, N., *Laser-induced alignment and anti-alignment of rotationally excited molecules*, *Physical Chemistry Chemical Physics* **13**, 8671 (2011).
- [55] Prince, B. D., *Development and application of a hybrid femtosecond/picosecond coherent Raman probe designed for study of excited state systems*, *Ph.D. thesis*, Iowa State University, Digital Repository, Ames (2008).
- [56] Chin, S. L., *Femtosecond Laser Filamentation*, Springer Series on Atomic, Optical, and Plasma Physics, Vol. 55 (Springer New York, New York, NY, 2010).
- [57] Nurhuda, M., Suda, A. & Midorikawa, K., *Generalization of the Kerr effect for high intensity, ultrashort laser pulses*, *New Journal of Physics* **10**, 053006 (2008).
- [58] Béjot, P. et al., *Higher-order kerr terms allow ionization-free filamentation in gases*, *Physical Review Letters* **104**, 103903 (2010), arXiv:1011.1598 .
- [59] Liu, W. W., *Intensity Clamping During Femtosecond Laser Filamentation*, *Chinese Journal of Physics* **52**, 465 (2014).

- [60] Bernhardt, J. *et al.*, *Pressure independence of intensity clamping during filamentation: theory and experiment*, *Applied Physics B* **91**, 45 (2008).
- [61] Chin, S. L. *et al.*, *Some fundamental concepts of femtosecond laser filamentation*, *Springer Series in Chemical Physics* **89**, 243 (2008).
- [62] Théberge, F. *et al.*, *Self-stabilization of third-harmonic pulse during two-color filamentation in gases*, *Applied Physics B* **87**, 207 (2007).
- [63] Keldysh, L., *Ionization in the field of a strong electromagnetic wave*, *Sov. Phys. JETP* **20** (1965), 10.7790/tja.v61i2.213.
- [64] CHIN, S. L., *FROM MULTIPHOTON TO TUNNEL IONIZATION*, in *Advances in Multi-Photon Processes and Spectroscopy*, *Advances in Multi-Photon Processes and Spectroscopy*, Vol. 23 (WORLD SCIENTIFIC, 2004) pp. 249–271.
- [65] Liu, Y. *et al.*, *Self-seeded lasing in ionized air pumped by 800 nm femtosecond laser pulses*, *Optics Express* **21**, 22791 (2013).
- [66] Wang, P. *et al.*, *Population dynamics of molecular nitrogen initiated by intense femtosecond laser pulses*, *Physical Review A* **92**, 063412 (2015).
- [67] Zhao, X., Nolte, S. & Ackermann, R., *Lasing of N₂⁺ induced by filamentation in air as a probe for femtosecond coherent anti-Stokes Raman scattering*, *Optics Letters* **45**, 3661 (2020).
- [68] Chin, S. L. *et al.*, *The propagation of powerful femtosecond laser pulses in optical media: physics, applications, and new challenges*, *Canadian Journal of Physics* **83**, 863 (2005).
- [69] Papeer, J. *et al.*, *Extended lifetime of high density plasma filament generated by a dual femtosecond–nanosecond laser pulse in air*, *New Journal of Physics* **16**, 123046 (2014).
- [70] Loriot, V. *et al.*, *Measurement of high order Kerr refractive index of major air components: erratum*, *Optics Express* **18**, 3011 (2010).
- [71] Nibbering, E. T. J. *et al.*, *Determination of the inertial contribution to the nonlinear refractive index of air, N₂, and O₂ by use of unfocused high-intensity femtosecond laser pulses*, *Journal of the Optical Society of America B* **14**, 650 (1997).
- [72] Brodeur, A. & Chin, S. L., *Ultrafast white-light continuum generation and self-focusing in transparent condensed media*, *Journal of the Optical Society of America B* **16**, 637 (1999).
- [73] Liu, W. & Chin, S. L., *Direct measurement of the critical power of femtosecond Ti:sapphire laser pulse in air*, *Optics Express* **13**, 5750 (2005).
- [74] Marburger, J., *Self-focusing: theory*, in *International Quantum Electronics Conference, 2005.*, Vol. 2005 (IEEE, 2005) pp. 1593–1593.
- [75] Aközbek, N. *et al.*, *White-light continuum generation and filamentation during the propagation of ultra-short laser pulses in air*, *Optics Communications* **191**, 353 (2001).
- [76] Li, H. *et al.*, *Critical power and clamping intensity inside a filament in a flame*, *Optics Express* **24**, 3424 (2016).
- [77] Sharma, A. *et al.*, *Counting the electrons in a multiphoton ionization by elastic scattering of microwaves*, *Scientific Reports* **8**, 1 (2018).
- [78] Théberge, F. *et al.*, *Tunable ultrashort laser pulses generated through filamentation in gases*, *Physical Review Letters* **97**, 1 (2006).
- [79] Schulz, E. *et al.*, *Intense few-cycle laser pulses from self-compression in a self-guiding filament*, *Applied Physics B: Lasers and Optics* **95**, 269 (2009).
- [80] Ripoche, J. F. *et al.*, *Determination of the time dependence of n₂ in air*, *Optics Communications* **135**, 310 (1997).

- [81] Hahn, J. W. & Lee, E. S., *Measurement of nonresonant third-order susceptibilities of various gases by the nonlinear interferometric technique*, *Journal of the Optical Society of America B* **12**, 1021 (1995).
- [82] Tedder, S. A. *et al.*, *Determination of probe volume dimensions in coherent measurement techniques*, *Applied Optics* **47**, 6601 (2008).
- [83] Chu, W. *et al.*, *A self-induced white light seeding laser in a femtosecond laser filament*, *Laser Physics Letters* **11** (2014), 10.1088/1612-2011/11/1/015301.
- [84] Lin, Y.-C., Nabekawa, Y. & Midorikawa, K., *Conical third-harmonic generation of optical vortex through ultrashort laser filamentation in air*, *Optics Express* **24**, 14857 (2016).
- [85] Bohlin, A. & Kliewer, C., *Single-shot Coherent Raman Multiplex Planar Imaging*, in *CLEO: 2014*, Vol. 2 (OSA, Washington, D.C., 2014) p. STu3I.7.
- [86] Mazza, F. *et al.*, *High-temperature rotational-vibrational O₂CO₂ coherent Raman spectroscopy with ultrabroadband femtosecond laser excitation generated in-situ*, *Combustion and Flame* , 111738 (2021).
- [87] Kliukin, D. *et al.*, *Cascaded coherent anti-Stokes Raman scattering for high-sensitivity number density determination in the gas phase*, *Journal of Raman Spectroscopy* , 1 (2021).
- [88] Miller, J. D. *et al.*, *Single-shot gas-phase thermometry using pure-rotational hybrid femtosecond/picosecond coherent anti-Stokes Raman scattering*, *Optics Express* **19**, 15627 (2011).
- [89] Williams, M. L., *CRC Handbook of Chemistry and Physics, 76th edition*, *Occupational and Environmental Medicine* **53**, 504 (1996).

Acknowledgements

Writing the acknowledgements is part of closing an important phase in my life. During this phase, I learned to appreciate experimental science and the complexity of it. This thesis would not have been possible without the help of a great number of people. I would like to thank a few in particular.

Firstly, my daily supervisor during the experimental campaign, **Ir. Francesco Mazza**. Dear Francesco, during the thesis work you knew to enthuse me about all physical process in the lab. Most of the time, a surprising result led to an inspiring lecture on the physical phenomenon. I believe that this spirit will make the remainder of your PhD a success. During the experiments, we had to work for long days to make certain deadlines. Sometimes, the results from the lab were frustrating and disappointing. However, most important is that in the end we succeeded! Your contributions to this work are indispensable. A notable fact is the number of times we had a miscommunication. Quite often we agreed upon a fact, but managed to explain the fact in completely different ways. I think, that this made us better as it required both of us to be sharp. I genuinely appreciate your contributions. Thank you Francesco.

Next, **Dr.ir. Alexis Bohlin**. Dear Alexis, a year ago I wrote you to ask if you had any places for a MSc thesis. From Nathan Griffioen, a friend of mine and MSc student at your group, I had heard great stories about your working ethics. Nathan told me that the human factor was of great importance in your research group. This convinced me to join your group. For me, the topic was secondary. The atmosphere within the group was of more importance. During my thesis work, we had a number of conversations about a wide range of topics. Among them were a cancelled holiday to Sweden, woman rights and career choices. The spontaneous meetings in the lab and the city centre of Delft resulted always in an interesting and appreciated talk. You showed interest, and invested time in those encounters. It helped to enjoy the work. In the meantime I have become enthusiastic about the topic. The complexity of the topic was exactly what I was looking for. All in all, I am happy that I choose you as my supervisor. Thank you for the opportunity.

Then, my daily supervisor during my literature study, **Dr. Dmitrii Kliukin**. Dear Dmitrii, it has been some time since we had our weekly meetings. But I am still convinced that the weekly hour in which I could ask all sorts of questions related to CARS and non-linear optics helped me get up to speed. Your answers were always on the right level of difficulty. The support resulted in a great literature study with very positive feedback. I would like to thank you again for those meetings.

Ir. Leonardo Castellanos Gonzales. Dear Leonardo, during the experimental campaign we spend many hours together in the lab. These hours were stressful at times, mainly when experiments were performed for the rebuttal. Your presence was calming and therefore added to the atmosphere in the lab. I am impressed by the amount of work you did during this time.

The defence committee, consisting of **Prof.dr.ir. P. Colonna di Paliano, Dr. R.M. Groves, Dr.ir. Alexis Bohlin, Ir. Francesco Mazza**, I would like to thank for reading and grading of my MSc thesis.

Dear **Anand Vijayaraghavan**, as fellow MSc student we worked to produce our final figures in the last few months. In this phase, I came to you with CRS related questions. You invested time and tried to help me. I respect this mentality willing to drop your own work to look at my figures. Thank you.

Beste **Ir. Nathan Griffioen**, ik wil je graag bedanken voor de goede verhalen die je hebt verteld over de onderzoeksgroep. Je liet me zien hoe belangrijk het is om de juiste groep mensen om je heen te hebben. Aan het begin van mijn thesis, het einde van jouw thesis, heb je me geholpen met de beginselen van CRS. Deze telefoontjes hebben geholpen om te begrijpen wat we aan het doen zijn.

Lieve **papa, mama, Thijs, Maartje en Geert**, afgelopen paar jaar is voor ons niet gemakkelijk geweest. Een aantal gebeurtenissen heeft er voor gezorgd dat we weer met z'n allen aan iets beters werken. Ik waardeer de energie die er is om er weer iets gezelligs van te maken. Het gaat ons lukken.

Papa, ik wil je bedanken voor het meedenken en lezen van mijn masterscriptie. Het is goed om te zien dat de natuurkunde van 40 jaar geleden nog nuttig kan worden toegepast. Uiteindelijk is het je ook gelukt om de processen in het lab een beetje te begrijpen. Niet gek als je bedenkt dat ik hier bijna een jaar aan heb gewerkt. Je was niet alleen nuttig om de grammatica te verbeteren, maar je hebt ook geholpen om de structuur van het verhaal te verbeteren. Dankjewel Pap.

Beste **Coen en Joppe**, als huisgenoten hebben jullie van dichtbij meegemaakt hoeveel tijd ik op de TU heb gezeten. Of misschien anders verwoord, hebben jullie meegemaakt hoe weinig ik thuis was. Mijn hersenschudding en de drukte omtrent mijn scriptie hebben er afgelopen jaren voor gezorgd dat ik vaak niet gezellig was 's avonds. Vaak moest ik vroeg naar bed om de volgende dag fit te zijn. Dat de situatie zo was en nog steeds deels zo is, is door de jaren heen door jullie altijd gerespecteerd. Iets wat ik enorm waardeer. Ik waardeer de sfeer die we met zijn drieën hebben gecreëerd.

Lieve **Liv**, ik wil je bedanken voor de continue steun, zowel tijdens mijn hersenschudding als tijdens de lange dagen voor mijn scriptie. Er was meestal weinig uitleg nodig om begrip te krijgen. Verder vond ik het altijd leuk als je interesse toonde in de lasers. Af en toe miste er wat natuurkundige kennis om het volledige verhaal te begrijpen, maar de interesse bleef, erg leuk!

Aert Stutvoet